Abstract

This paper deals with ELF emissions observed in the dayside magnetosphere, called ELF hiss and polar chorus. These waves are generated in the magnetic equatorial region through Doppler-shifted cyclotron wave-particle interaction by high-energy electrons. According to the satellite observations, the features of ELF emissions such as power spectrum and wave normal direction in low-altitude polar region are significantly different from magnetic equatorial plane after their propagation in the magnetosphere. Especially in ELF range, magnetospheric ions play a fundamental role in low-altitude propagation, for example in LHR reflection and multi-ion cutoff.

Previous work on ELF wave ray tracing from the high-altitude magnetic equatorial plane to low altitudes revealed that most of the rays undergo LHR reflection before they reach the usual level of polar orbiting satellites. So, it seems that ELF emissions observed by polar orbiting satellites and on the ground have propagated along field-aligned ducts. However, there is abundant evidence from satellite ELF wave observations that the wave normal of ELF emission makes a large angle with the earth's magnetic field at low altitudes, and this feature can be explained only by nonducted propagation. Therefore, it is important to find out the condition required for the nonducted ray path between the magnetic equatorial plane and low altitudes without suffering from LHR reflection. This kind of ray path is of special interest in the present study, and it is referred to as "penetrating ray path" in this paper.

This paper is devoted to the study of the above two kinds of propagation from the magnetic equatorial plane to the polar region with the observations of ELF/VLF waves by ISIS satellites over Antarctica, ELF waves at Syowa Sation, Antarctica and Bremsstrahlung X-rays by balloons. Characteristics of ELF emissions observed at the high-altitude equatorial region and the low-altitude polar region are briefly reviewed first. Conditions for the existence of penetrating ray paths are obtained from a 2-dimensional ray tracing. Wave normal directions and arriving latitudes at low altitudes are also calculated.

These calculated characteristics of ELF wave normals are compared with those from ISIS satellite observation in the altitude range of 1450–3500 km by means of spin-modulated characteristics and multi-ion cutoff characteristics of received ELF signals. Seasonal variation of ELF emission intensity at the ISIS satellite altitude and on the ground is attributable to a north-south asymmetry in the penetrating ray paths depending on a field-aligned electron density gradient in the both hemispheres.

Another mode of ELF wave propagation, *i.e.*, ducted propagation outside the

plasmapause, is investigated for periodic emissions. This type of emission is recorded on the ground at regular intervals of several seconds, alternately in the opposite hemispheres. Hence the emission is thought to be caused by an echoing of wave packet between the two hemispheres along a field-aligned duct. Periodic emissions with the same repetition interval are often observed over an area of more than 2000 km wide at the ISIS satellite altitude and on the ground. Such a wide spatial extent of emission reception is explained in this chapter from a viewpoint that the ELF duct terminates at a certain altitude, below which the waves propagate downward widely in nonducted mode.

Finally, ELF emissions observed on the ground are compared with Bremsstrahlung X-rays observed by balloons. As the electrons producing such X-rays precipitate along magnetic field lines, a pattern of electron precipitation observed on the ground is a projection onto the polar ionosphere of the wave-particle interaction region near the magnetic equator.

Hence the electron precipitation associated with ELF emission activity affords useful information on the source location of ELF emissions. With this background in mind, three balloon experiments were carried out in northern Norway and at Syowa Station, Antarctica, and the observed Bremsstrahlung X-rays and ELF emissions were compared for three characteristic time scales: slow variations (a few tens of minutes), pulsations (from a few tens of seconds to several minutes) and bursts (below 10 s).

1. General Introduction

1.1. Introduction

At the daytime auroras zone, strong natural electromagnetic emissions are observed in ELF range in the topside ionosphere and on the ground. They are classified into two categories according to their frequency-time spectra (HELLIWELL, 1965). The one is chorus which consists of many random discrete tones lasting a few tenth of a second, usually with rising frequency, and the other is ELF hiss which shows a steady-state white noise spectrum with very little frequency-time structure. The main purpose of the present works is to investigate the propagation characteristics of these emissions in the magnetosphere on the data of polar orbiting satellites ISIS-1 and 2, and ground-based observation at Syowa Station, Antarctica.

The occurrences of these ELF emissions are correlated with worldwide geomagnetic activities (UNGSTRUP and JACKEROTT, 1963; KOKUBUN *et al.*, 1969), and they are often associated with a high energy ($\geq$40 keV) electron precipitation observed by electron detectors on board polar orbiting satellites (OLIVEN and GURNETT, 1968; HOLZER *et al.*, 1974) and by Bremsstrahlung X-ray detectors on board balloons (ROSENBERG *et al.*, 1971, 1981; FOSTER and ROSENBERG, 1976; YAMAGISHI *et al.*, 1985; KREMSER *et al.*, 1986). Therefore the emission is considered to be whistler mode waves generated through Doppler-shifted cyclotron wave-particle interaction of high energy electrons in the magnetic equatorial region, being injected on the nightside during an auroral substorm and drifted eastward to the morningside (KENNEL and PETSCHEK, 1966; THORNE *et al.*, 1974; ASHOUR-ABDALLA and COWLEY, 1974; THORNE *et al.*, 1977).

These emissions generated in the equatorial region propagate down eventually to the ground through the magnetosphere and the ionosphere. However, the characteristics and the spatial distribution of these emissions observed by high altitude equatorial satellites (OGO-1, 3 and 5, GEOS-1 and 2, ISEE-1 and 2, EXOS-B) are different from those observed by low altitude polar orbiting satellites (Alouette 1 and 2, ISIS-1 and 2, Injun-3 and 5, OGO-2, 4 and 6) in their wave normal direction, L-shell dependence of the emission frequency band, and relative distribution of chorus and ELF hiss as will be described in the following section. Most of the differences are connected with propagation characteristics of whistler mode waves in the magnetosphere, which depend essentially on the behavior of ions at low altitudes especially in ELF range. Thus it is important to study the propagation characteristics of ELF emissions in the magnetosphere for comprehensive understanding of the physical nature of ELF emissions at low altitudes and on the ground.

1.2. ELF emissions at high ($\geq$3000 km) altitudes

Chorus and ELF hiss are the dominant ELF electromagnetic emissions in the magnetic equatorial region outside the plasmapause (RUSSELL *et al.*, 1969; BURTIS and HELLIWELL, 1969, 1976; DUNCKEL and HELLIWELL, 1969; RUSSELL and HOLZER, 1970; BARRINGTON *et al.*, 1971; TSURUTANI and SMITH, 1977; CORNILLEAU-WEHRLIN *et al.*, 1978a). Chorus and ELF hiss occur simultaneously in most cases, although one or the other frequently dominates the spectrum (CORNILLEAU-WEHRLIN *et al.*, 1978a).

Another kind of strong unstructured emission is observed inside the plasmapause, and it is called "plasmaspheric hiss". This emission is quite distinct from those outside the plasmapause in its local time appearance and dependence on substorm activity (THORNE *et al.*, 1973, 1974, 1977; SMITH *et al.*, 1974). This emission is confined to the plasmasphere and contributes little to the ELF emissions observed outside the plasmapause (THORNE *et al.*, 1979; HUANG and GOERTZ, 1983; HUANG *et al.*, 1983; CHURCH and THORNE, 1983). Hence this type of emission is excluded from the present study.

Local time and magnetic latitude dependence of chorus occurrence was obtained by eccentric equatorial satellites (DUNKEL and HELLIWELL, 1969; RUSSELL *et al.*, 1969; TSURUTANI and SMITH, 1977). There is very little chorus activity in the pre-midnight quadrant. The activity in the post-midnight quadrant increases but is confined mainly to the equatorial region. However in the dawn quadrant, the region of frequent chorus occurrence expands to higher latitudes, although chorus is observable more frequently at the equator. The increase of chorus activity in the morning quadrant is understandable by taking account of the cold plasma density enhancement at the magnetic equator caused by an upward flow of cold plasma from the sunlit ionosphere. The enhancement of cold plasma density makes to decrease the wave phase velocity as well as resonant electron energy, and this in turn leads to increase the growth rate of whistler mode waves. In the afternoon quadrant, the activity diminishes but is observed over a wide range of latitude.

A region of strong ELF hiss is found in the morning and afternoon quadrants at magnetic latitudes between 40° and 50° (RUSSELL *et al.*, 1969). The local time dependence of this high latitude ELF hiss is quite different from that of equatorial chorus. The former mostly appears in the afternoon quadrant, whereas the latter in the pre-noon quadrant. Thus it appears that these two kinds of ELF hiss in different regions are separate phenomena.

TSURUTANI and SMITH (1977) found a similar high latitude region of chorus occurrence at magnetic latitudes between 45° and 55°, though its appearance above 50° was unknown due to a limited orbital coverage of the satellite for their study. They explained that high latitude chorus is locally generated at "minimum B pockets" which are regions of relatively low field strength formed at 20°–50° magnetic latitude due to the dayside compression of the magnetosphere by the solar wind (ROEDERER, 1970). High latitude chorus was found predominantly on the dayside from 08–16 LT, and it appeared roughly symmetrically about noon. Equatorial chorus is substorm related, whereas high latitude chorus does not depend on substorm activity.

The center-frequency of the ELF emission is controlled by the equatorial electron gyro-frequency, f_{H0}. It is approximately $0.5 f_{H0}$ at moderate L-value (BURTIS and

HELLIWELL, 1969), and close to $0.25 f_{H0}$ at higher L-value (RUSSELL and HOLZER, 1970). BURTIS and HELLIWELL (1976) reported a double-peak distribution of chorus frequency at $0.53 f_{H0}$ and $0.34 f_{H0}$. There is a missing band of the emission at $0.5 f_{H0}$. TSURUTANI and SMITH (1977) reported a maximum distribution of equatorial chorus frequency at 0.25–$0.3 f_{H0}$. The relationship between emission frequency and f_{H0} obtained in the geomagnetic equatorial plane is useful to determine the source location of the emission observed at low altitude.

1.3. ELF emissions at low (300–3000 km) altitudes

ELF hiss and chorus are common ELF emissions at low altitudes. Besides, there are also some other low-altitude emissions such as auroral hiss (GURNETT, 1966), narrow-band electromagnetic ion cyclotron waves (TEMERIN and LYSAK, 1984; SAITO *et al.*, 1986, 1987; SATO and HAYASHI, 1985), electrostatic ion cyclotron waves (BERING *et al.*, 1975; OGAWA *et al.*, 1981; YAMAGISHI *et al.*, 1981), which are not observed deep in the magnetosphere.

Among these ELF emissions, ELF hiss is the strongest one. ELF hiss at a low altitude is much different from that of the ELF hiss detected in the equatorial region. The intensity of ELF hiss near the magnetic equator shows a remarkable decrease outside the plasmasphere with an abrupt change at the plasmapause (BURTON *et al.*, 1970), whereas the low altitude ELF hiss is seen far beyond the normal position of the plasmapause ($L=4$, or 60° INV). Furthermore, the region of most frequent occurrence of emission always lies outside the plasmapause position. Thus it appears that ELF hiss from the plasmasphere is not the source of low altitude ELF hiss. The ELF hiss observed together with chorus outside the plasmasphere is thought to be a reasonable source of the low-altitude ELF hiss, because some simultaneous equatorial satellite-ground observations of ELF emission demonstrated nearly parallel time variation of the both emission intensities with a similar time variation in the energetic electron flux at the equator (CORNILLEAU-WEHRLIN *et al.*, 1978b). The equatorial hiss shows nearly the same occurrence tendency as that of chorus in the magnetic equatorial region, whereas the low-altitude hiss commonly extends to latitudes higher than that of the chorus. Wave normal measurement of chorus by BURTON and HOLZER (1974) revealed that the chorus observed at low altitudes with considerable signal strength must be ducted along a field line. On the other hand, there is abundant evidence that the ELF hiss is nonducted at low altitudes such as multi-ion cutoff of ELF hiss (GURNETT and BURNS, 1968; ALTMAN *et al.*, 1975; Chapter 3 of this paper). The different appearance tendency between chorus and ELF hiss at low altitudes is interpreted by taking account of above-mentioned different propagation mode for each emission, *i.e.*, chorus propagates along the field line, whereas the ELF hiss deviates from the field line in nonducted mode to extend towards higher latitudes.

The local time dependence of chorus activity at low altitudes shows maximum in the pre-noon quadrant (OLIVEN and GURNETT, 1968), which is quite similar to that obtained near the equatorial region described in Section 1.2. The local time dependence of ELF hiss recording at low altitudes also shows maximum in pre-noon quadrant, but it extends even to the afternoon quadrant (TAYLOR and GURNETT, 1968).

The region of chorus occurrence contains the area of micro-burst electron pre-

cipitations with energies greater than 40 keV (OLIVEN and GURNETT, 1968). Every micro-burst observed on Injun 3 satellite was accompanied by a chorus. This correlation is consistent with the mechanism of chorus generation near the equator by an electron cyclotron instability with the resulting diffusion of electron into loss cone and eventual precipitation into the ionosphere.

1.4. Contribution of the present work

As reviewed in preceding sections, characteristics of ELF emissions observed at the magnetic equatorial region show a significant difference from those observed at low altitudes, and the difference is attributable mostly to effect of ELF wave propagation in the magnetosphere. Previous works on calculated ray path from the magnetic equatorial plane to low altitudes (THORNE and KENNEL, 1967; AIKYO and ONDOH, 1971) revealed that most of the rays undergo LHR reflection at an altitude of several thousands of kilometers which is well above the usual levels of low-altitude satellites. Therefore, ELF emissions detected by low-altitude satellites must satisfy a strict condition of wave normal angle in order to escape from LHR reflection if the wave propagates in nonducted mode. This kind of ray path is referred to as "penetrating ray path" in this paper. Another mode of propagation between magnetic equatorial region and low altitudes is ducted propagation. This work is devoted to the analysis of the above two kinds of propagation with the data of ELF/VLF wave observation by ISIS satellite over Antarctica, ground-based ELF wave observation at Syowa Station, Antarctica and Bremsstrahlung X-ray observation by balloons.

In Chapter 2 of this paper, necessary conditions for the existence of penetrating ray paths are obtained with 2-dimensional ray tracing. Wave normal distribution and arriving latitudes at ISIS satellite altitudes are also calculated in this chapter.

In Chapter 3, wave normal distribution of ELF emissions in the altitude range of 1450–3500 km is obtained from ISIS satellite ELF observation by means of spin-modulated characteristics and multi-ion cutoff characteristics of received signals. These observational results are compared with the wave normal distribution calculated in Chapter 2. Seasonal variation of ELF emission intensity was obtained at ISIS satellite altitude, and this is explained by a seasonal change in conditions for penetrating ray path caused by an asymmetric field aligned electron density gradient between summer and winter hemispheres.

In Chapter 4, ducted propagation outside the plasmapause is investigated with help of periodic emissions, which appear on the ground at regular intervals of several seconds. Occurrence rate of ducted propagation outside the plasmapause is inferred from the occurrence characteristics of periodic emissions obtained from continuous wideband recordings of ELF emissions in the both hemispheres. Periodic emission with the same repetition interval is often observed over an area of more than 2000 km wide at ISIS satellite altitude and on the ground. Such a wide extent is explained in this chapter from a viewpoint that the ELF duct is terminated at a certain altitude and the waves released from the duct spread in nonducted mode.

It is generally difficult to obtain a source location of ELF emission on the equatorial plane from the ground-based ELF wave observation due to the diverging and poleward skewing of ELF wave propagation in the magnetosphere. When a strong

ELF emission activity arises on the magnetic equatorial plane, it causes a pitch angle diffusion of high energy electrons into loss cone, and these electrons precipitate eventually into the ionosphere. Therefore the location of electron precipitation associated with ELF emission activity gives useful information on the source location of the ELF emissions. In Chapter 5, ELF emissions observed on the ground are compared with the precipitation observed at balloon altitude as Bremsstrahlung X-ray. Comparison is made within three characteristic time scales: slow variations (a few tens of minutes), pulsations (a few tens of seconds to several minutes) and bursts (below 10 s).

Chapter 6 gives concluding remarks.

2. Nonducted Propagation of Whistler Mode ELF Waves in the Magnetosphere

2.1. Introduction

As reviewed in the preceding chapter, characteristics of ELF emissions observed at the magnetic equatorial region show significant differences from those observed at low altitudes such as wave normal directions and L-shell dependence. These differences are mostly attributable to effects of whistler mode wave propagation in the magnetosphere, which is calculated by ray tracing. Since the first computer program for ray tracing made by YABROFF (1961), a pronounced progress is made in the ray tracing technique in the past two decades as reviewed by KIMURA (1985). The ion effects were first included in the ray tracing program by KIMURA (1966) which makes possible to explain several characteristics of magnetospheric whistlers such as subprotonospheric (SP) whistlers and magnetospherically reflected (MR) whistlers. More realistic magnetospheric models came to be used in the ray tracing such as introducing of plasmapause (AIKYO and ONDOH, 1971; INAN and BELL, 1977) and adopting of non-dipolar geomagnetic field with 3-dimensional ray tracing (KIMURA *et al.*, 1985). Effect of plasma temperature is introduced by HASHIMOTO *et al.* (1977), which is useful for the ray path calculation starting from the deep magnetosphere.

Among these, several studies were made on the ELF nonducted ray paths from the magnetic equatorial plane to the polar ionosphere in order to explain physical nature of ELF emissions at low altitudes (THORNE and KENNEL, 1967; AIKYO and ONDOH, 1971). They revealed that most of the nonducted rays undergo LHR reflection at an altitude of several thousands of kilometer which is well above the usual levels of low-altitude satellites. Therefore a nonducted ray path between the geomagnetic equatorial plane and low altitudes without suffering from LHR reflection must satisfy a strict condition of the wave normal angle at the equator. This kind of ray path is referred to as "penetrating ray path" in this work and is investigated in this chapter. Another mode of propagation between magnetic equatorial plane and low altitudes is ducted propagation which will be investigated in Chapter 4.

In this chapter, we use 2-dimensional ray tracing program without temperature effect. The magnetospheric model is dipolar magnetic field with plasmapause as described in Section 2.2. In Section 2.3, general characteristics of nonducted ray paths in ELF range are studied by means of a 2-dimensional ray tracing. The characteristics and the conditions for the existence of the "penetrating ray path" are summarized in Section 2.4. The controlling factors on the altitude dependence of wave

normal angles are discussed in Section 2.5. Summary of this chapter is given in Section 2.6.

2.2. Magnetospheric model for ray path calculation

In this section, magnetic field, electron and ion distributions in the magnetosphere are described, which are used for ray tracing calculation. The geomagnetic field is given by a centered dipole field. The magnetic field intensity B_0 at a point (r, ϕ) is given as

$$B_0 = 8.0 \times 10^6 \sqrt{(1+3\sin^2\phi)}/r^3 \,(T), \tag{1}$$

where r is the geocentric distance in km and ϕ is magnetic latitude. Each field line is identified by an invariant latitude Λ, or an "L value" as

$$r/\cos^2\phi = R_E/\cos^2\Lambda, \tag{2}$$

and

$$L = r/(R_E \cos^2\phi) = 1/\cos^2\Lambda, \tag{3}$$

where R_E is the mean earth radius of 6370 km. The electron and ion density distributions follow AIKYO and ONDOH model (1971). In the model, the plasmapause position is assumed at $L=4.0$ as a typical location in quiet condition.

In the plasmasphere and in the polar ionosphere below an altitude of 3000 km, the number density of electrons and ions can be well described in terms of diffusive equilibrium model (ANGERAMI and THOMAS, 1964) as follows (KIMURA, 1966):

$$\begin{aligned} N_{de}(r,\phi) &= N_{e0}(\phi)\sqrt{\textstyle\sum_i \eta_i \exp(-z/H_i)}, \\ N_{di}(r,\phi) &= N_{de}\eta_i \exp(-z/H_i) \,/\, \textstyle\sum_i \eta_i \exp(-z/H_i), \\ z &= r_0(1-r_0/r), \quad H_i = kT/M_i g_0, \end{aligned} \tag{4}$$

where N_{de}, N_{di} : the electron and the i-th ion densities,
N_{e0} : the electron density at the reference level $r_0=6970$ km (600 km in altitude),
z : the geopotential height,
H_i, η_i : the scale height and the composition of the i-th ion at the reference level,
M_i : the mass of the i-th ion,
k, T, g_0 : the Boltzmann constant, the electron temperature, and the gravity constant at the reference level, respectively.

In our model, ions are composed of H^+, He^+, and O^+, and their composition at the reference level is $\eta_H=0.002$, $\eta_{He}=0.001$, and $\eta_o=0.997$, respectively. N_{e0} is assumed to be 4×10^4 cm^{-3}. Outside the plasmasphere and in the topside polar ionosphere higher than the altitude of 3000 km, a collisionless model distribution (EVIATAR *et al.*, 1964) is taken. In this region, only H^+ is considered as a sole ion species, and the ion density, N_{ci}, is given by EVIATAR as

$$N_{ce}=N_{ci}=N_{e0}\exp(-z/2H_p)\left[1-\sqrt{1-B_0/B_c}\ \exp\{(-z/2H_p)B_0/(B_c-B_0)\}\right], \quad (5)$$

where H_p is the scale height of proton, B_c is the geomagnetic field intensity at the bottom of the collisionless region, respectively. In order to obtain a smooth function of the particle distribution at the plasmapause, the particle densities N_{dj} and N_{ej} (j=i or e) are linearly combined with the weighting function f and given as follows (AIKYO and ONDOH, 1971),

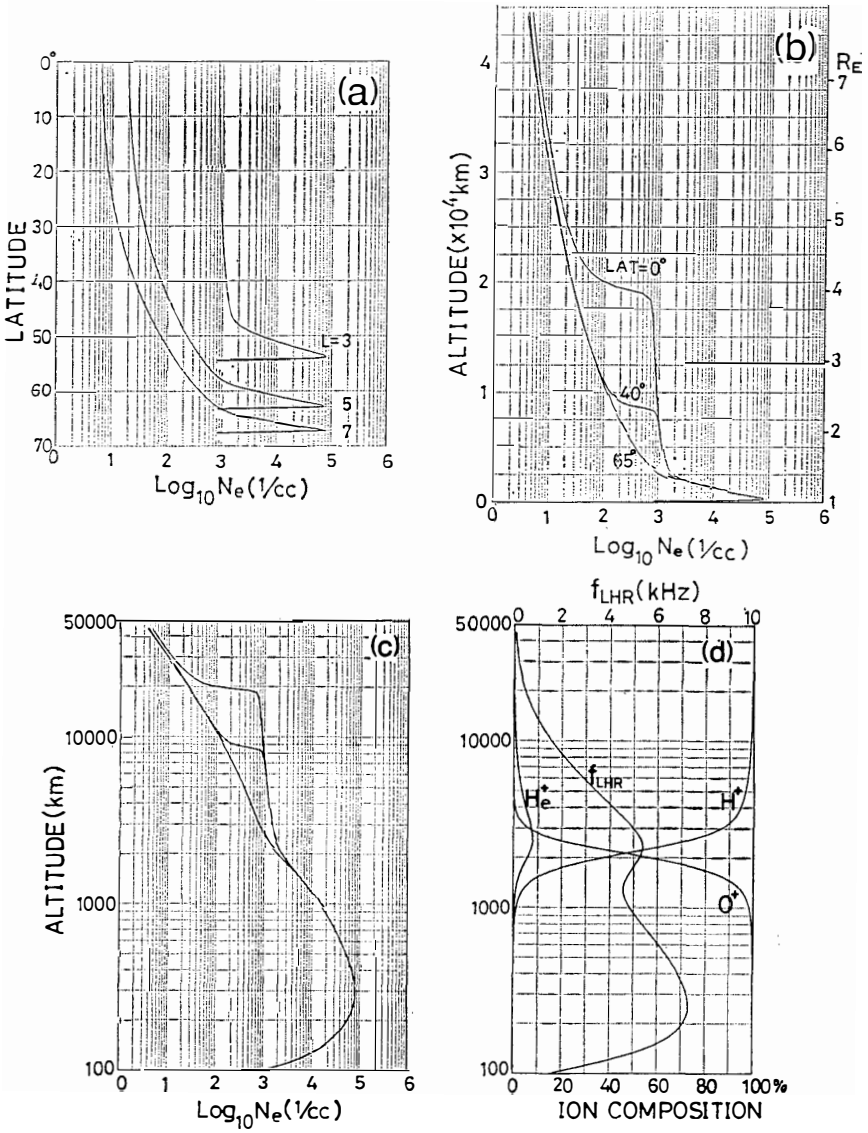

Fig. 1. *(a) A model of the electron density distributions in the magnetosphere used for the ray tracing. Three curves show electron density profiles along geomagnetic field lines of L=3.0, 5.0 and 7.0.*
(b) Electron density profiles along the radial directions at magnetic latitudes 0°, 40° and 65° with a linear altitude scale.
(c) The same as Fig. 1b except that a logarithmic altitude scale is used.
(d) Profiles of ion composition and the LHR frequency along geomagnetic latitude of 65°.

$$N_j=\left\{\frac{1}{2}-f(L)\right\}N_{dj}+\left\{\frac{1}{2}+f(L)\right\}N_{cj}\,,$$
$$f(L)=(1/\pi)\tan^{-1}(1-\xi_L)/\varepsilon_L\,, \tag{6}$$
$$j=e,\ H^+,\ He^+,\ \text{and}\ O^+\,,$$

where L, ξ_L and ε_L are the L value at a given point, the plasmapause position, and the half-width of the transition region. In our later calculation, $\xi_L=4.0$ and $\varepsilon_L=0.05$ are chosen. Latitude dependences of the ion composition, electron density and electron temperature at the reference level are not considered.

Figure 1 shows a model of electron and ion density distributions in the magnetosphere used in the ray tracing. Figure 1a shows electron density profiles along geomagnetic field lines of $L=3.0$, 5.0 and 7.0. Figure 1b shows electron density profiles along the radial directions at magnetic latitudes 0°, 40° and 65° with a linear altitude scale. Figure 1c is the same as Fig. 1b except that a logarithmic altitude scale is used. Figure 1d shows profiles of ion composition and the LHR frequency at geomagnetic latitude of 65°.

2.3. Nonducted ray paths in the magnetosphere

In this section, the general characteristics of nonducted ray paths starting from the geomagnetic equatorial plane are studied by means of a 2-dimensional ray tracing. In the ray tracing, the wave frequency of 1.5 kHz is chosen as a typical frequency of the ELF/VLF emission observed at Syowa Station, and the starting point on the magnetic equatorial plane is assumed to be at $L=6.0$, which is almost the same L-value of Syowa Station ($L=6.1$). In the meridian plane, there are two resonance angles, *i.e.* the one directing away from the earth and the other directing towards the earth. Hereafter they are referred to as "outer" and "inner" resonance angles, respectively. For the wave normal angle, ψ, with respect to the earth's magnetic field, $\boldsymbol{B}_0$, the positive sign indicates the direction away from the earth. The resonance angle defined as $\psi_{RA}=\cos^{-1}(f/f_H)$, where f denotes the wave frequency concerned and f_H the electron gyrofrequency, is 67° for $f=1.5$ kHz at the starting point. In the ray path calcula-

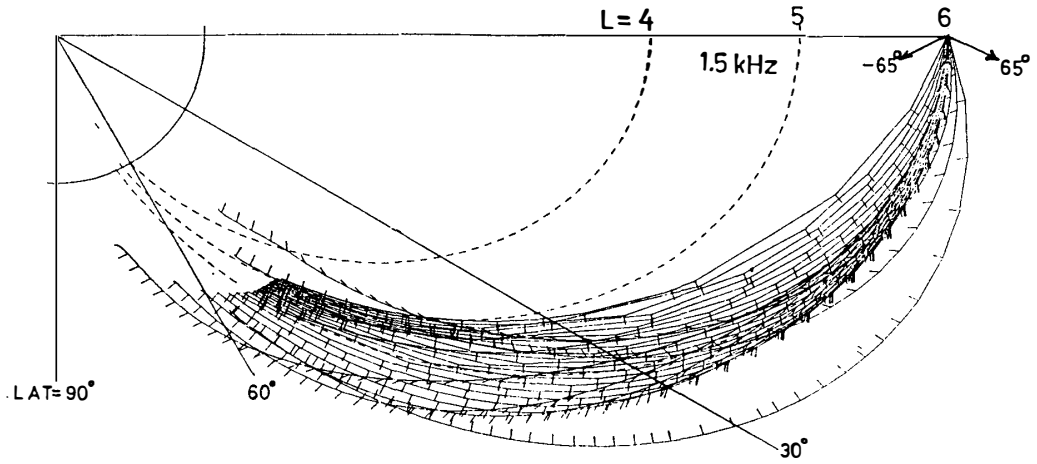

Fig. 2. A meridional plot of the ray paths of 1.5 kHz wave started from the equatorial plane at $L=6.0$. The initial wave normal angle is assumed at every 5° from −65° to +65°.

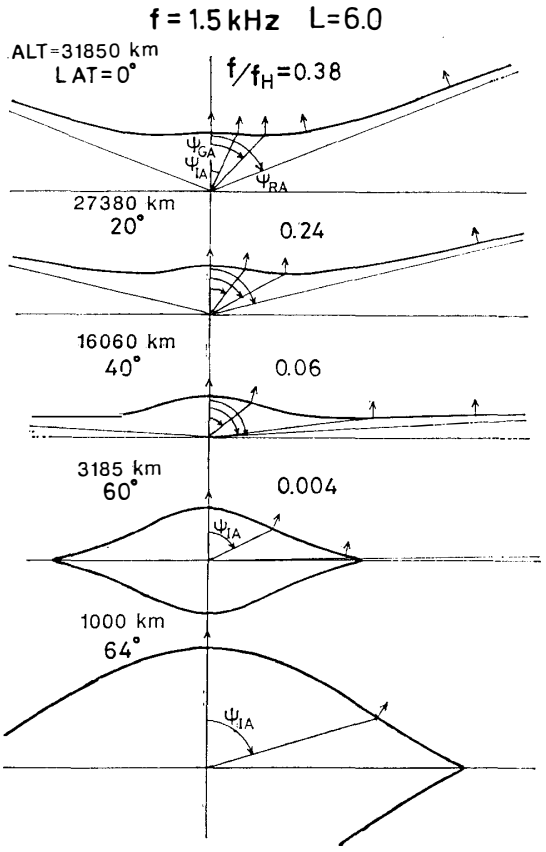

Fig. 3. The refractive index curves of the whistler mode wave of 1.5 kHz along L=6.0 field line at latitudes 0°, 20°, 40°, 60° and 64°. The ray directions are given by the arrows perpendicular to the refractive index curve.

tion, initial wave normal angle, ψ_i, is selected every 5° from −65° to 65°, so that the distribution of the nonducted ray paths from a point source can be obtained.

Figure 2 shows a meridional plot of the calculated ray paths. Wave normal directions are marked by short bars on each ray path. There are regions of ray path concentration in the latitude ranges of 0°–20° and 40°–50°. This feature of the ray path distribution is qualitatively understood by a change of the shape of refractive index curves along the ray paths, because ray directions are given as the normals of the refractive index curves. Figure 3 shows the refractive index curves of 1.5 kHz wave along $L=6.0$ field line at latitudes 0°, 20°, 40°, 60° and 64°. The altitudes corresponding to these latitudes are shown in the figure. The ray directions are given by the normals of the refractive index curve and shown by arrows on each curve. In the figure, ψ_{GA} stands for the Gendrin angle defined as the wave normal angle at which $n\cdot\cos\psi$ becomes minimum. When $\psi=\psi_{GA}$, the ray direction becomes parallel to $\boldsymbol{B}_0$. The angle ψ_{IA} stands for the inflection angle defined as the wave normal angle at which the ray direction shows the maximum deviation from $\boldsymbol{B}_0$. These angles are given by the following equations,

$$\psi_{GA} = \cos^{-1}(2f/f_H), \tag{7}$$

and

$$\psi_{IA} = \cos^{-1}\left\{\frac{f \cdot A}{f_H} + \frac{1}{3}\sqrt{1-\left(\frac{f}{f_H}\right)^2 A^2}\right\}, \tag{8}$$

where A denotes the effect of ion given by the following equation when only H^+ is considered:

$$A = 1-(f_H/f)(f_{Hp}/f) + (f_H/f_p)^2, \tag{9}$$

where f_{Hp} and f_p are proton gyro and electron plasma frequencies, respectively. At magnetic latitude of 0°, the refractive index curve shown at the top of Fig. 3 is almost flat and perpendicular to $\boldsymbol{B}_0$ for $|\psi| < \psi_{GA}$. Consequently, the ray directions for this range of ψ become almost parallel to $\boldsymbol{B}_0$, and the ray paths are kept along the field line of the starting point. However, at magnetic latitudes greater than 20°, the curvature of the refractive index curve for the above range of ψ increases, and the ray directions diverge around $\boldsymbol{B}_0$. Thus, a concentration region of ray paths is formed in the magnetic latitude range of 0°–20°. Another concentration region of ray paths, located at the magnetic latitude range of 40°–50°, is explained at the end of this section. In Fig. 2, only the downgoing ray paths are illustrated, and the termination of a ray path at an altitude around 10000 km indicates an occurrence of the LHR reflection described later. Due to this reflection, it is generally difficult for ELF waves starting from the magnetic equator to reach the polar ionosphere in nonducted mode.

Figure 4a shows the altitude dependence of ψ for each ray path shown in Fig. 2. The resonance angle along the ray path is also shown in the figure. For most part of

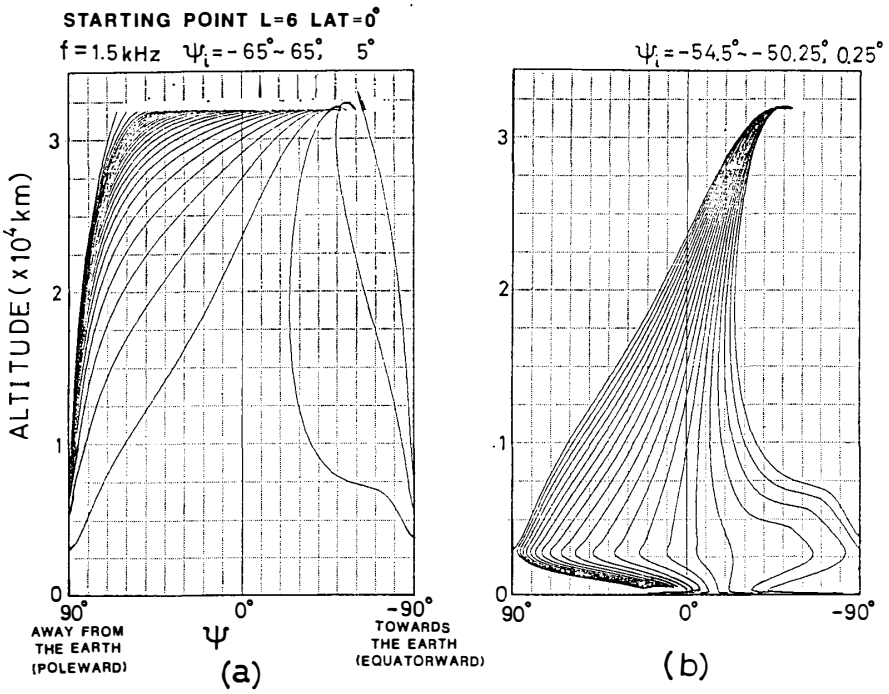

Fig. 4. (a) Altitude variation of ψ for the ray paths shown in Fig. 2. (b) Altitude variation of ψ for the "penetrating" ray paths.

the ray paths, wave normal angle increases, or turns away from the earth in the course of downward propagation and eventually reaches the outer resonance angle. When ψ_i has a large negative value ($\psi_i < -55°$ in this case), the wave normal angle decreases with decreasing altitude and it reaches the inner resonance angle. There is a critical initial wave normal angle, ψ_{ic}, for selecting either one of these opposite traverses of the wave normal variation. In our model, ψ_{ic} is $-50°$ for $L=6.0$ at the geomagnetic equator. In this figure, most of the wave normals are directed to either inner or outer resonance angle at an altitude below 10000 km. The resonance angle becomes almost perpendicular to $\boldsymbol{B}_0$ in the altitude below 6000 km. As shown in Fig. 1d, f_{LHR} increases with decreasing altitude and it becomes equal to the wave frequency of 1.5 kHz at an altitude of about 10000 km. So, most of the waves are reflected by LHR reflection at an altitude where both $f<f_{LHR}$ and $\psi=90°$ are satisfied. However, when ψ_i is within a few degree of ψ_{ic}, it takes a long time for ψ to attain a large angle, and in some cases, ψ never reaches 90°. These waves do not undergo LHR reflection and can reach the polar ionosphere. The ray paths of these waves are referred to as "penetrating ray paths". Figure 4b shows the altitude dependence of ψ for the "penetrating ray paths". Aside from the ducted propagation described in Chapter 4, the wave energy is carried along the "penetrating ray paths" from the magnetic equatorial plane to the polar ionosphere below the altitude of the LHR reflection. The propagation characteristics of the "penetrating ray paths" are analyzed in the following section.

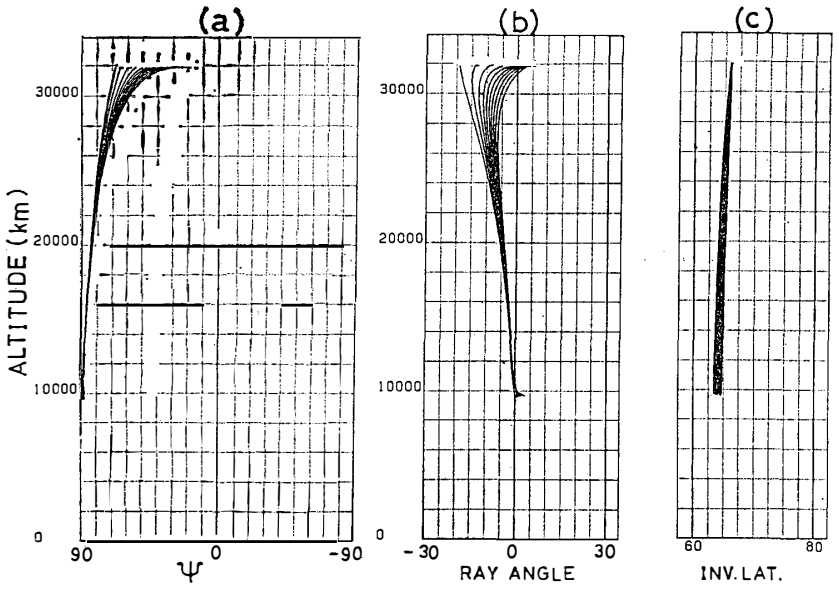

Fig. 5. (a), (b) and (c) show altitude variations of the wave normal angle, the ray angle, and the invariant latitude of ray path, respectively for 1.5 kHz wave started from the equatorial plane at $L=6.0$. Initial wave normal angle is taken every 5° from 20° to 65°.

In order to explain a concentration of ray paths at high latitudes in the altitude range of 8000–10000 km shown in Fig. 2, the altitude dependences of the wave normal angles, the ray angles and the invariant latitudes of the ray paths of $20° < \psi_i < 65°$ are shown in Figs. 5a–5c, respectively. In Fig. 5a, all of the wave normals are concentrated at the outer resonance angle when the altitude decreases. This tendency makes

the ray angles concentrate at the direction perpendicular to the outer resonance angle as shown in Fig. 5b. This indicates that all of the rays proceed in the same direction towards an inner L shell with little divergence as shown in Fig. 5c. Thus, the concentration region of the ray paths is formed in high latitudes at an altitude of 8000–10000 km and in the L shell of about 5.2 which is a little inner than the initial L shell of 6.0. The low altitude boundary of this region is given by the altitude of the LHR reflection.

2.4. Characteristics of the "penetrating ray paths"

In order to obtain the range of ψ_i which gives "penetrating ray paths", ray tracing was again carried out from the magnetic equatorial plane at $L=6.0$. The initial wave normal angle, ψ_i, was varied around ψ_{ic} with a very small increment of 0.25°. The results of the calculation is shown in Fig. 6, where altitude dependences of the wave normal angles, the ray angles and the invariant latitude of the penetrating ray paths are shown in Figs. 6a–6c, respectively in the same format as Fig. 5. It is found that ψ_i must be within the range of $-52.25° < \psi_i < -49.5°$ in order that the wave can reach the ionosphere. Hereafter, this range of ψ_i is referred to as "ψ_i window". In Fig. 6a, the resonance angle (R.A.), the Gendrin angle (G.A.) and the inflection angle (I.A.) along $L=6.0$ field line are also shown. For each curve of wave normal angle, ψ reaches its maximum at an altitude of about 3000 km. In the altitude below 3000 km, most of the wave normal angles are concentrated at an angle of large positive values (poleward direction). This angle is close towards 90° just below 3000 km and it becomes smaller with decreasing altitude according to Snell's law, *i.e.*, the wave normal turns toward the direction perpendicular to the ground due to a steep electron density gradient in this altitude range as shown in Fig. 1b. At the altitudes of ISIS satellites, the above-mentioned characteristics of the wave normal are confirmed by the ELF/VLF observation on board these satellites as described in Chapter 3.

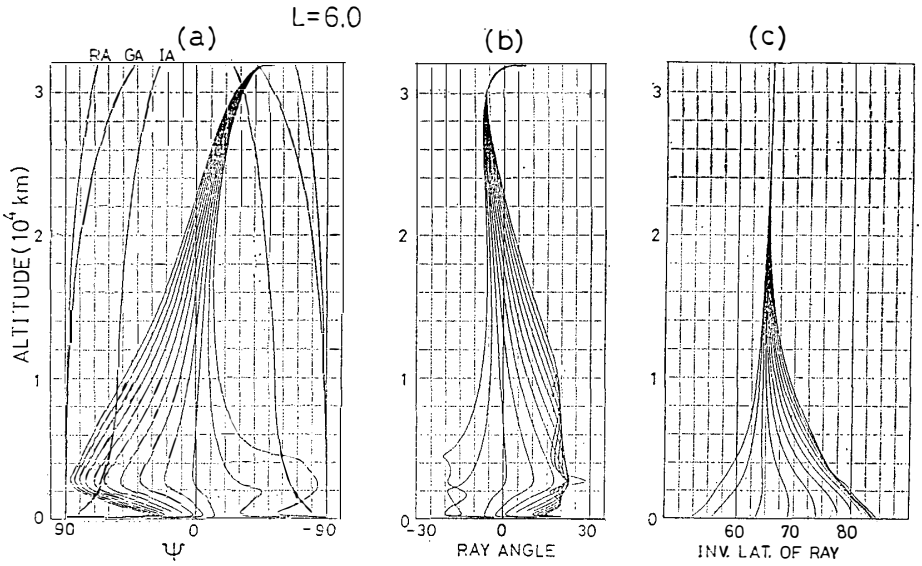

Fig. 6. (a), (b) and (c) show altitude variation of the wave normal angle, the ray angle, and the invariant latitude of the ray, respectively for the penetrating ray paths. The initial wave normal angle, ψ_i, is assumed at every 0.25° from −52.25° to −49.5°.

In Fig. 6b, ray angle within the altitude range from 3000 to 8000 km shows a maximum value at around 20° where the corresponding wave normal crosses the inflection angle. In the altitude below this maximum, the wave having propagated in the inner L shell overtakes the one in the outer L shell, and this causes piling up of the ray paths in the altitude below 5000 km for the invariant latitude greater than 75° as shown in Fig. 6c.

In Fig. 6c, the ray paths corresponding to those shown in panels Figs. 6a and 6b are confined within a narrow range of invariant latitude above an altitude of 20000 km, and they diverge below that altitude to cover a wide latitudinal range as much as 52.5°–84° at an altitude of the ionosphere. This wide spread is not real, because an

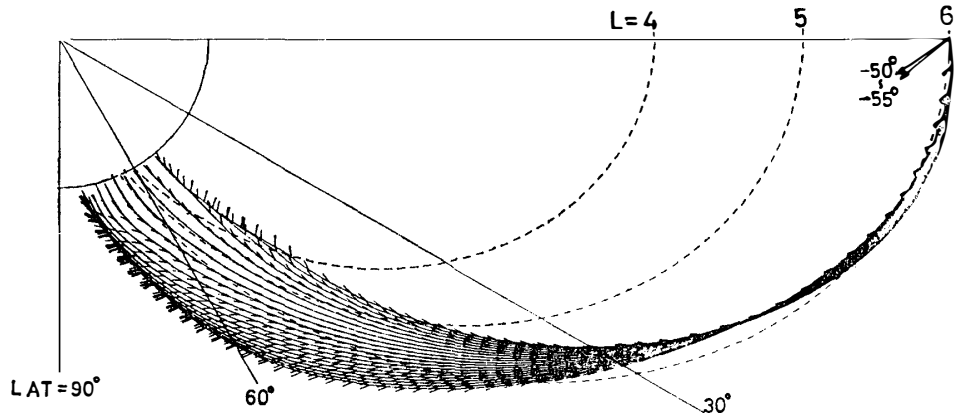

Fig. 7. Meridional plot of the ray paths shown in Fig. 6. Concentration of the ray paths towards outer L shell in the altitude below 5000 km is recognized.

actual north-south distance corresponding to a unit invariant latitude decreases at a low altitude due to the convergence of the magnetic field lines. In fact, Fig. 7 shows that the distribution of the ray path demonstrates maximum latitudinal spread of 4000 km at an altitude of 8000 km, and it becomes as small as 3000 km at the altitude of the ionosphere. The divergence of the ray paths below the altitude of 20000 km is interpreted in terms of the altitude dependence of the refractive index curve shown in Fig. 3. At a higher altitude near the magnetic equator, the curvature of the refractive index curve in the range of $|\psi| < \psi_{IA}$ is small, so that the ray directions in this range are collimated along $\boldsymbol{B}_0$, and the ray paths are kept within the initial L shell. However, in the altitude below 20000 km, the curvature of the refractive index curves for this range of ψ is increased and the ray directions diverge around $\boldsymbol{B}_0$. As a result, the ray paths diverge below 20000 km.

This distribution of ray paths is obtained from a point source located at $L=6.0$ in the magnetic equatorial plane. The source regions of the natural ELF/VLF emissions widely spread in the equatorial plane including the plasmasphere and the outer magnetosphere (*e.g.*, RUSSELL *et al.*, 1972, and the references herein). Therefore, the emissions observed at high latitudes are considered to be composed of the ray paths from a lot of sources widely distributed in the equatorial plane. In the following, ray paths are computed for the source positions of $L=4.5$, 5.0, 6.5 and 7.0 outside the plasmapause. In the plasmasphere, strong ELF emission (plasmaspheric hiss) always exists (*e.g.*, RUSSELL and HOLZER, 1970). Many previous works on the ray tracing

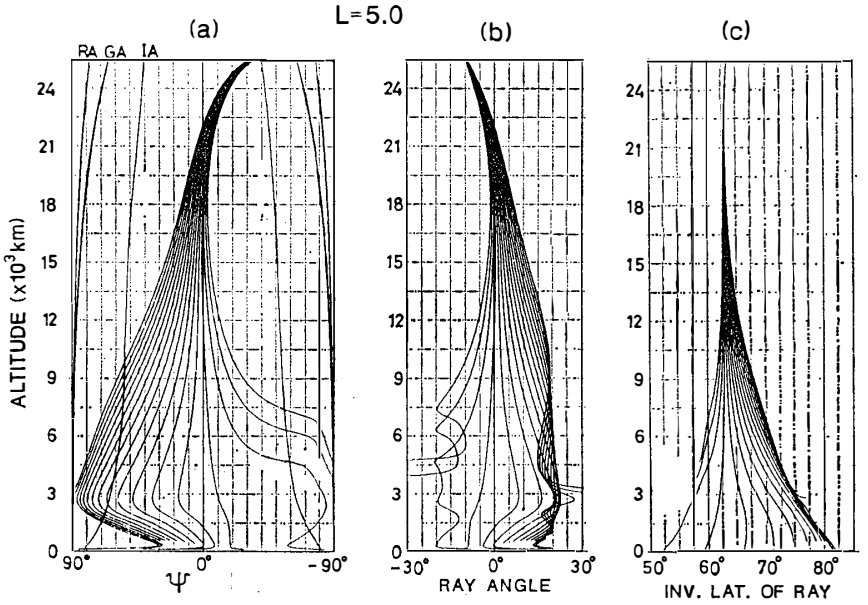

Fig. 8. The same as Fig. 6, except that the L value of the starting point is 5.0.

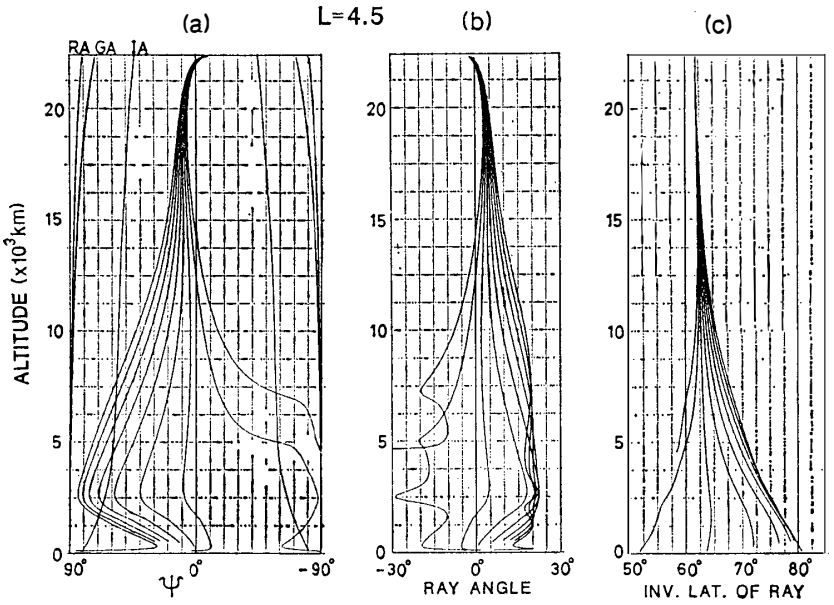

Fig. 9. The same as Fig. 6, except that the L value of the starting point is 4.5.

in the plasmasphere (*e.g.*, ONDOH *et al.*, 1972; THORNE *et al.*, 1979) show that these waves are confined to the plasmasphere and have little influence on the emissions observed in the polar ionosphere. Therefore the sources inside the plasmasphere is excluded in the following ray tracing. As we are interested in the emissions in the polar ionosphere, only those ray paths accessible to the polar ionosphere are calculated.

Figures 8 and 9 show the computational results for the cases of $L=5.0$ and $L=4.5$ in the same format as Fig. 6. The general characteristics of the propagation is much alike in these three cases, except for the fact that the location and the width of the

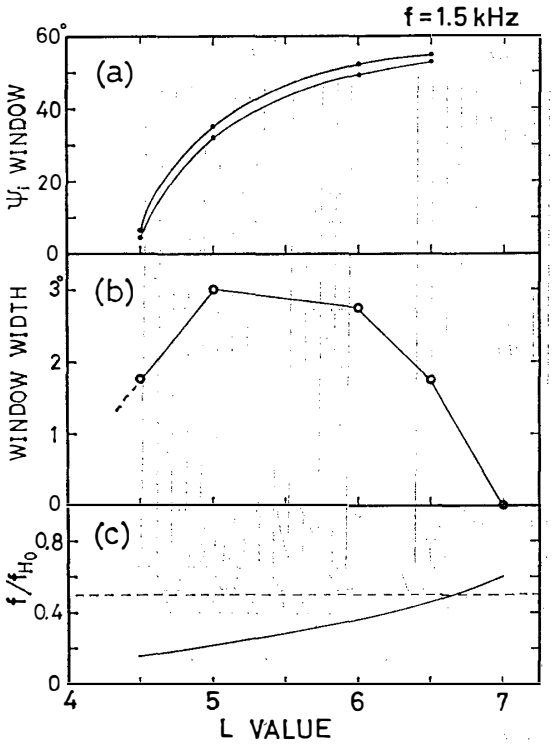

Fig. 10. L value dependency of the location of ϕ_i window (a) and the window width (b). The ratio of wave frequency f and the equatorial gyro frequency, f_{H0}, is shown in (c). The ϕ_i window vanishes at L=7.0, where f/f_{H0} exceeds 0.5.

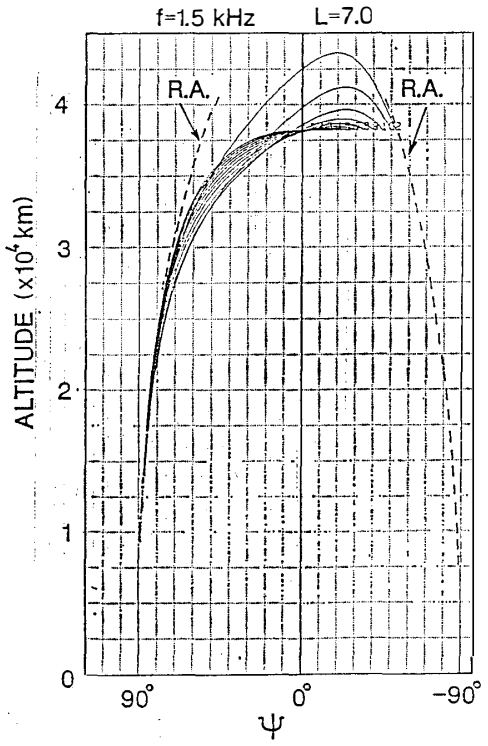

Fig. 11. Altitude variation of wave normal angle for the case of f=1.5 kHz and the starting L value of 7.0. All of the wave normal curves approach outer resonance angle and undergo LHR reflection at 10000 km. Hence the ϕ_i window vanishes in this case.

ϕ_i window are dependent upon the source location. This feature of the ϕ_i window is shown in Fig. 10 as a function of L value. The location and the width of the ϕ_i window is shown in Figs. 10a and 10b, respectively. The wave frequency normalized by the equatorial electron gyro frequency, f_{H0}, is shown in Fig. 10c. When the source location shifts to an inner L shell, the ϕ_i window comes closer to $\boldsymbol{B}_0$. This behavior can be explained by the effect of the increasing electron density gradient near the plasmapause. This effect turns the wave normal towards a region of higher electron density, *i.e.*, an inner L shell, by Snell's law. This results in the wave normal turning towards an outer L shell shown in Fig. 4.

When the source is located at L=7.0, the ϕ_i window disappears, *i.e.* all of the rays from the equator are reflected before they reach the polar ionosphere. Figure 11 shows the altitude variation of ψ of these ray paths for the initial L value of 7.0 and ϕ_i of 0° to −52.5°. When ϕ_i is very close to the inner resonance angle of −54°, the ray goes upward at first with the wave normal almost aligned with the inner resonance angle. Then, it turns and goes downward with the wave normal approaching to the outer resonance angle. So, all of the wave normals are concentrated to the outer resonance angle within low altitude range and these waves are reflected at an altitude of 10000 km where the wave frequency is equal to the local LHR frequency. This

wave normal variation is related to a change in the nature of the refractive index curve at the equator when f/f_{H0} exceeds 0.5, *i.e.*, when $f/f_{H0}>0.5$, the refractive index curve is concave for all values of ψ, while the refractive index curve is convex for $|\psi|<\psi_{IA}$ and concave for $|\psi|>\psi_{IA}$ when $f/f_{H0}<0.5$.

Figure 12 shows results for the wave frequency of 0.7 kHz. The general characteristics are similar to that of 1.5 kHz shown in Fig. 10, except for the fact that the window width is narrower in the case of 0.7 kHz, and that the ψ_i window does not

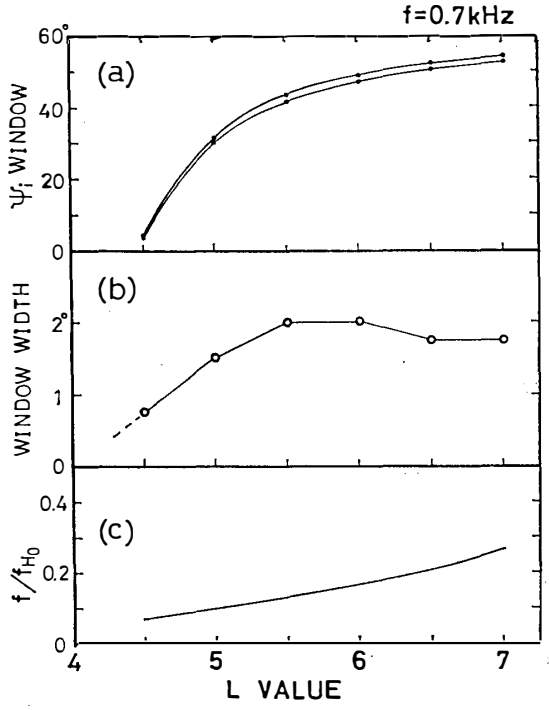

Fig. 12. The same as Fig. 10 except that the wave frequency is 0.7 kHz. The window width is narrower than that of $f=1.5$ kHz.

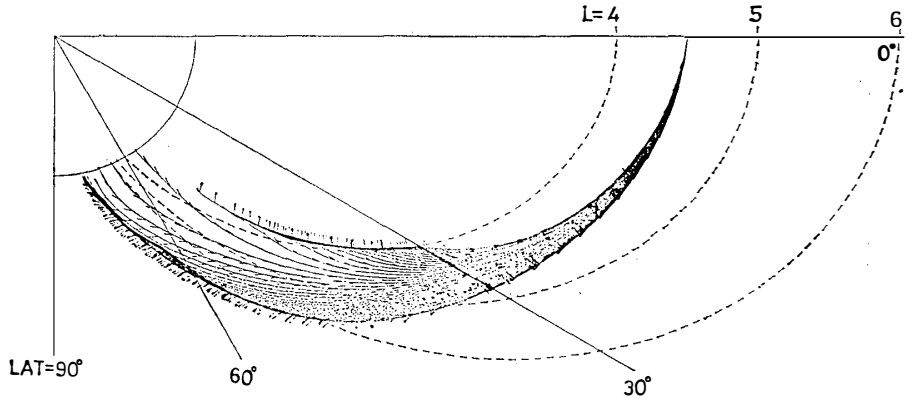

Fig. 13. A meridional plot of ray paths of 1.5 kHz waves starting from the equatorial plane at $L=4.5$. The initial wave normal angle is almost within ψ_i window. The wave normal direction of the ray paths coming close to the plasmapause is forced to turn towards perpendicular to the geomagnetic field line due to the steep electron density gradient at the plasmapause and these rays undergo LHR reflection.

disappear for $L=7.0$, because the condition of $f/f_{H0}<0.5$ is satisfied for the wave frequency of 0.7 kHz. For both frequencies, the window width is decreased when the starting point is located near the plasmapause. This may be understood considering a meridional plot of the ray paths of 1.5 kHz waves starting from the equatorial plane at $L=4.5$, as shown in Fig. 13. The wave normal direction of the ray paths coming close to the plasmapause is forced to turn to the direction of a steep electron density gradient at the plasmapause, which is almost perpendicular to $\boldsymbol{B}_0$. These waves are reflected at a latitude where the wave frequency is equal to the local LHR frequency. If there were no plasmasphere, the wave normal angle of these ray paths remains within a small value with respect to $\boldsymbol{B}_0$, and these waves do not undergo LHR reflection and reach the polar ionosphere. So, the existence of the plasmapause decreases the width of ψ_i window when the starting point is located near the plasmapause.

2.5. Discussion

The time variation of the wave normal angle along a ray path can be described in the following differential equation given by WALTER (1969) and SCARABUCCI (1969),

$$\frac{2n}{c}\cdot\frac{\partial\psi}{\partial t}=\sin\delta\left\{\frac{\partial(\ln N_e)}{\partial r}+\frac{3}{r}(m_c+m_y)\right\}-\frac{\cos\delta}{r}\left\{\frac{\partial(\ln N_e)}{\partial\theta}+m_\theta\right\}, \tag{10}$$

where c is the speed of light and δ is the wave normal angle with respect to the radial direction given by the following relation,

$$\delta=(270^\circ+I)+\psi, \tag{11}$$

where I denotes the dip angle of the geomagnetic field given by the relation of $\tan I=2\cot\theta$, where θ is colatitude. In this equation, quasi longitudinal approximation,

$$n^2\simeq(f/f_p)^2/\{(f_H/f)\cos\psi-1\}, \tag{12}$$

is assumed. The effect of the curvature of the earth's magnetic field is given by

$$m_c=2(1+\cos^2\theta)/(1+3\cos^2\theta), \tag{13}$$

and the effect of the altitude variation of the refractive index curve is given by the following equations,

$$\left.\begin{aligned} m_\theta&=\{3\sin\theta\cos\theta/(1+3\cos^2\theta)\}m_y,\\ m_y&=(f_H/f)\cos\psi/\{(f_H/f)\cdot\cos\psi-1\}.\end{aligned}\right\} \tag{14}$$

Eq. (10) is expressed in another form,

$$(2nr/c)\cdot\partial\psi/\partial t=(-1/N_e\cdot\partial N_e/\partial\theta\cdot\cos\delta)+(r/N_e\cdot\partial N_e/\partial r\cdot\sin\delta)+(3m_c\sin\delta)+(3m_y\sin\delta-m_\theta\cos\delta). \tag{15}$$

On the right-hand side of this equation, the first and the second terms give an effect of electron density gradient in θ and r directions, respectively. The third term

gives an effect of the curvature of the geomagnetic field line, and the last term gives an effect of the altitude variation of the magnitude of $\boldsymbol{B}_0$.

These four terms give the physical meaning of the wave normal variations along the ray paths shown in Fig. 4. In the following, each term of eq. (15) is calculated for a fixed value of ψ for simplicity. This procedure corresponds to calculate $\partial\psi/\partial t$ at the intersections of the wave normal curves and a vertical line of a certain value of

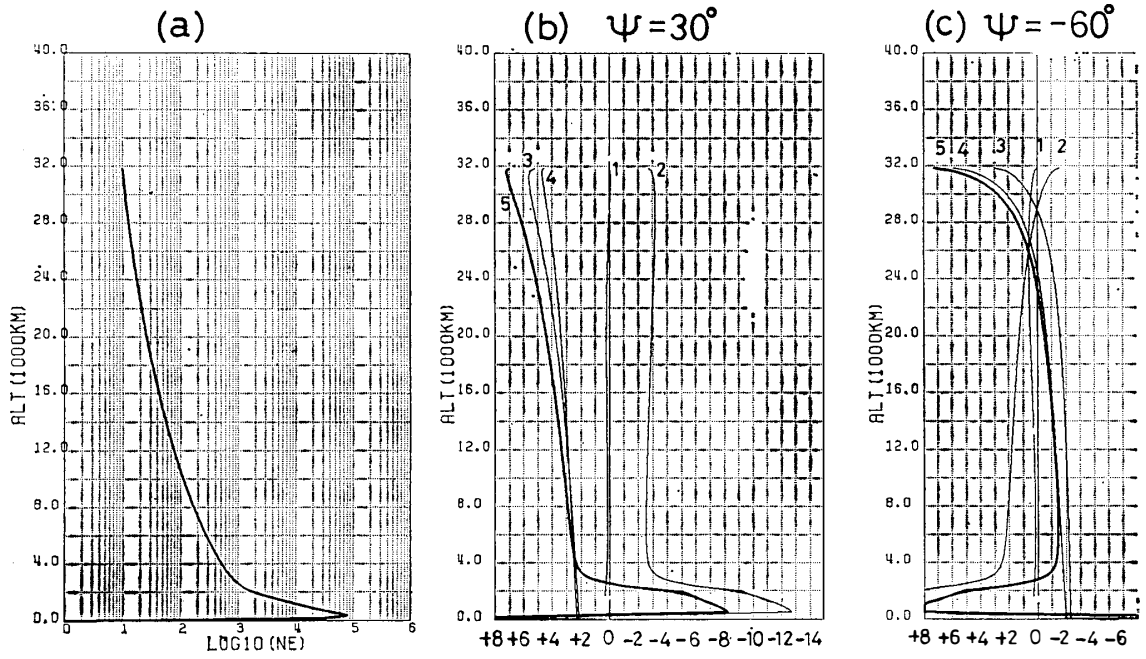

Fig. 14. (b) and (c) show altitude variation of the each term of eq. (15) for the case of $\psi=30°$ and $-60°$, respectively. An electron density profile used in this calculation is shown in (a). In (b) and (c), thin lines labeled from 1 to 4 correspond to the four terms in the right-hand side of eq. (15) and a bold line labeled 5 corresponds to the summation of these four terms.

ψ in Fig. 4. The calculation was made along the field line of $L=6.0$ for the wave frequency of 1.5 kHz, and the results are shown in Fig. 14 for the case of $\psi=30°$ (Fig. 14b) and $\psi=-60°$ (Fig. 14c). Figure 14a shows the electron density profile used in the calculation. In the figure, the four terms on the right-hand side of eq. (15) are shown by thin curves labeled 1 to 4, and the summation of these four terms, *i.e.* the left-hand side, is shown by a bold curve labeled as 5. As a positive sign of ψ corresponds to the wave normal directing away from the earth, the positive sign of the abscissa, $\partial\psi/\partial t$, indicates the turning of a wave normal in a direction away from the earth.

In Fig. 14b, the effect of the latitudinal electron density gradient (curve 1) is always much smaller than the other effects. The effect of the vertical electron density gradient (curve 2) is always negative, *i.e.* this rotates the wave normal towards the earth. This effect is greatly increased in the altitude below 3000 km, where the electron density profile in Fig. 14a shows a steep increase. The effects of the curvature of the geomagnetic field (curve 3) and the altitude variation of the geomagnetic field (curve 4) are always positive, and they tends to rotate the wave normal away from the earth.

The sum of these effects, shown by the curve 5, is positive above an altitude of 3000 km, and this explains the general tendency of the wave normal turning away from the earth shown in Fig. 4. At the altitude below 3000 km, the curve 5 takes a negative value due to an increase in the vertical electron density gradient, and this causes the turning of wave normal towards the earth, or the equatorward, shown in Fig. 4b for $\psi>0$ at the altitude below 3000 km.

In Fig. 14c, the signs of the four terms of eq. (15) are similar to those in Fig. 14b near the starting point. However, the second and the third terms, shown by the curves 2 and 3, change their sign at an altitude of 28900 km, and the fourth term, shown by the curve 4, changes its sign at an altitude of 24300 km. The change in sign of these terms is due to the polarity change of $\sin\delta$ included in each term when δ exceeds 180°. In fact, the dip angle, I, is $-30°$ at an altitude of 28900 km for $L=6.0$ in the southern hemisphere. By substituting $-30°$ for I and $-60°$ for ψ in eq. (11), δ becomes 180°. When the sign changes, the role of these terms on the wave normal direction is reversed. This explains a concentration of wave normal angles at the inner resonance angle at an altitude of 7000 km as shown in Fig. 4a for the value of ψ_1 smaller than ψ_{1c}. In Fig. 4b, the poleward turning of the wave normal for $\psi<0$ at the altitude below 3000 km is also explained by a positive value of curve 5 at the same altitude.

At an altitude of about 3000 km, the effect of the electron density gradient balances with the other effects, and $\partial\psi/\partial t$ becomes zero as shown by the zero crossing of curve 5 in Fig. 14. At this altitude, $|\psi|$ of the penetrating ray paths show their maxima as shown in Fig. 4b. This gives a criterion for the penetrating ray paths, that is, those having $|\psi|$ smaller than 90° at this altitude are the penetrating ray paths. This also demonstrates that the ψ_1 window is obtained by a backward ray tracing of the critical ray paths whose wave normal angle at this altitude is $90°-\varepsilon$ and $-90°+\varepsilon$, where ε denotes an infinitely small and positive value.

2.6. Summary

From a 2-dimensional ray tracing of ELF waves starting from the geomagnetic equatorial plane outside the plasmapause, it was found that for most of the ray paths, wave normal turns away from the earth during downward propagation, and eventually reaches the outer resonance angle which is very close to 90° at low altitudes. For those ray paths whose wave normal at the equator directs inward (towards the earth), the wave normal turns towards the earth during downward propagation, and reaches the inner resonance angle which is very close to $-90°$ at low altitudes. These waves are reflected upward at an altitude where both $f<f_{\mathrm{LHR}}$ and $|\psi|=90°$ are satisfied (LHR reflection).

There is a critical equatorial wave normal angle, ψ_{1c}, which contributes to selecting the wave normal variation out of the above-mentioned two opposite tendencies. The value of ψ_{1c} is dependent upon the ambient magnetic field and electron density distribution in the magnetosphere, and it is $\sim-50°$ in our magnetosphere model for $f=1.5$ kHz and $L=6.0$. When the wave normal angle at the equator is within a few degree of ψ_{1c}, it takes a long path length for ψ to attain a large angle, and in some cases, $|\psi|$ never reaches 90°. These waves do not undergo LHR reflection and reach

the polar ionosphere. The ray paths of these waves are called "penetrating ray paths", and the range of equatorial wave normal angle which permits penetrating ray paths are called "ψ_1 window". The penetrating ray paths show "poleward skewing" in the low altitude, *i.e.* the ray paths shift to higher latitude when they approach nearer to the earth.

After the formula given by WALTER (1969) and SCARABUCCI (1969), the wave normal direction is controlled by four factors: (1) latitudinal dependence of electron density, (2) height variation in electron density, (3) curvature of the geomagnetic field, and (4) height variation of the geomagnetic field. The factors (1) and (2) makes turning the wave normal towards the earth, whereas (3) and (4) away from the earth. The effects of (3) and (4) are greater than that of (1) and (2) at high altitudes (above $\sim$3000 km), and this turns the wave normal away from the earth. However, the effect of (2) becomes greater than that of (3) and (4) at low altitudes (below $\sim$3000 km) due to a steep electron density increase at the topside ionosphere, and this turns the wave normal towards the vertical.

The effects of (1) and (2) balance with that of (3) and (4) at a certain altitude along a penetrating ray path, where wave normal shows maximum deviation from $\boldsymbol{B}_0$. This point on the ray path is called "turning point" of wave normal. The altitude of the turning point is dependent on the electron density profile of the magnetosphere, and it is $\sim$3000 km for our model.

From the maximum wave normal deviation at the "turning point", it is found that the ψ_1 window at the equator is given by the backward tracing of the critical penetrating ray paths whose wave normal angles at the "turning point" are $90°-\varepsilon$ and $-90°+\varepsilon$, where ε denotes an infinitely small and positive value.

The location of ψ_1 window, or ψ_{1c}, approaches to $\boldsymbol{B}_0$ when the starting point approaches to the plasmapause. The width of the ψ_1 window decreases with increasing L value of the starting point when $L>5$, and it also decreases in the proximity of the plasmapause. The ψ_1 window vanishes when the wave frequency is greater than the one half of the equatorial electron gyrofrequency.

3. Nonducted ELF Emissions Observed by ISIS Satellites and on the Ground

3.1. Introduction

Ray tracing of ELF waves in Chapter 2 revealed that most of the nonducted ray paths undergo LHR reflection above usual altitude of polar orbiting satellite and only special nonducted ray paths, *i.e.* "penetrating ray paths", are accessible to satellite altitudes. Wave normals of penetrating ray paths converge towards 90° with respect to $\boldsymbol{B}_0$ at an altitude of about 3000 km where the effects of field line curvature and of vertical electron density gradient on wave normal variation balance. Below this altitude, the wave normal convergence becomes weaker with decreasing altitude. It is found that some results of ISIS satellite ELF wave observations over Syowa Station support above feature of penetrating ray paths, and they are described in this chapter.

Satellite data acquisition facilities were built up at Syowa Station in January 1976, and the telemetry reception of the ISIS-1 and 2 data has been carried out on a routine basis since April 1976. The geographic and geomagnetic coordinates of Syowa Station are 69.0°S and 39.6°E, −70.0° and 79.4°, respectively. The apogee and perigee altitudes of ISIS-1 are 3526 km and 578 km, and the orbit inclination is 88.4°, while ISIS-2 is in a circular orbit of ∼1450 km with the orbit inclination of 88.1°. ELF/VLF wave instruments onboard ISIS satellites consist of an electrical dipole antenna with 60 m in length and a receiver with frequency range of 50 Hz–25 kHz. The received wideband signal is telemetered to the ground receiving station *via* FM channel. Besides, total signal intensity for the above frequency range is telemetered *via* PCM channel. ELF/VLF emissions are also observed on the ground at Syowa Station, and ground ELF/VLF wave data are recorded on the same magnetic tapes along with the satellite ELF/VLF wave data. Characteristics of ELF/VLF emissions over Syowa Station observed by ISIS satellites are reported by YOSHINO *et al.* (1981).

In Section 3.2, wave normal direction of ELF hiss is obtained from the spin-modulated characteristics of received signal intensity. In Section 3.3, wave normal direction of ELF hiss is estimated from the attenuation at the multi-ion cutoff observed in the power spectrum of ELF hiss. Wave normal directions obtained from the above two methods agree well with the wave normal feature of penetrating ray paths calculated in Chapter 2. In Section 3.4, seasonal variation of ELF hiss intensity is obtained at ISIS satellite altitude, and it is explained by a seasonal difference in the condition for the existence of penetrating ray paths.

3.2. Wave normal direction of ELF hiss deduced from the satellite spin modulation

3.2.1. Introduction

From the ray tracing of ELF hiss in Chapter 2, it was found that the wave normal of ELF hiss converges to a certain direction pointing away from the earth in the lower magnetosphere below an altitude of ~3000 km. The convergence of the wave normal gives a well-defined polarization plane of the wave electric field perpendicular to the earth's magnetic field. In this condition, a rotating dipole antenna for ELF/VLF observation detects a sharp decrease of signal intensity twice during a rotation due to the directional sensitivity pattern of the receiving antenna. ELF hiss observed by ISIS-1 and 2 satellites passing over Syowa Station often showed such characteristics, and this fact seems to confirm the concentration of the wave normal direction predicted by the ray tracing described above.

An estimation of the wave normal direction from the characteristics of the spin-modulated received signal has been made for auroral kilometric radiation (KURTH *et al.*, 1975; JAMES, 1980), for auroral hiss (KAMADA *et al.*, 1981; KIMURA and MATSUO, 1982; NISHINO and TANAKA, 1987) and for Siple transmitter signals (SONWALKER and INAN, 1986). The first two papers dealt with electromagnetic waves of RX or LO mode, and the rest of the papers dealt with whistler mode waves. In this section, the wave normal direction of ELF hiss, which propagates in whistler mode, is obtained from the spin-modulated characteristics of the wave electric field with a similar method used by NISHINO and TANAKA (1987) and SONWALKER and INAN (1986). In the former paper, the wave electric field is analyzed under the restriction that the spin-axis is almost parallel to the earth's magnetic field, $\boldsymbol{B}_0$. In the latter paper, spin modulations of both electric and magnetic field components of the wave are analyzed and not only the wave normal direction, but also the effective height of the dipole antenna is obtained.

The first part of this section is devoted to obtain a wave normal direction of whistler mode wave from the spin-modulated characteristics for general spin axis direction. In the second part, this method is applied to the wave normal detection of ELF hiss observed by ISIS satellites. Finally, the result is compared with the propagation characteristics obtained from the ray tracing in Chapter 2.

3.2.2. Theory of wave normal detection

Figure 15 shows the sensor allocation and the coordinate system used in ISIS satellites. A set of three-axis magnetometer is used as a geomagnetic attitude sensor. A dipole antenna along Y-axis is used for VLF observation. The spin axis of the satellite is Z-axis. In the analysis of wave normal detection, another coordinate system shown in Fig. 16 is introduced, where z-axis is parallel to the earth's magnetic field $\boldsymbol{B}_0$, and x-z plane includes the wave normal vector $\boldsymbol{k}$, which makes an angle ψ with $\boldsymbol{B}_0$. The spin axis of the satellite is shown by a vector $\boldsymbol{Z}$, and its projection onto x-y plane is given by a vector $\boldsymbol{Z}'$ marked by a broken-line arrow. $\boldsymbol{Z}$ makes an angle γ with $\boldsymbol{B}_0$, and $\boldsymbol{Z}'$ makes an angle β with x-axis. The angle γ is obtained by the geomagnetic attitude sensor as

$$\gamma = \cos^{-1}(B_z / \sqrt{B_x^2 + B_y^2 + B_z^2}), \tag{16}$$

where B_x, B_y and B_z are the three components of $\boldsymbol{B}_0$ measured by the attitude sensor.

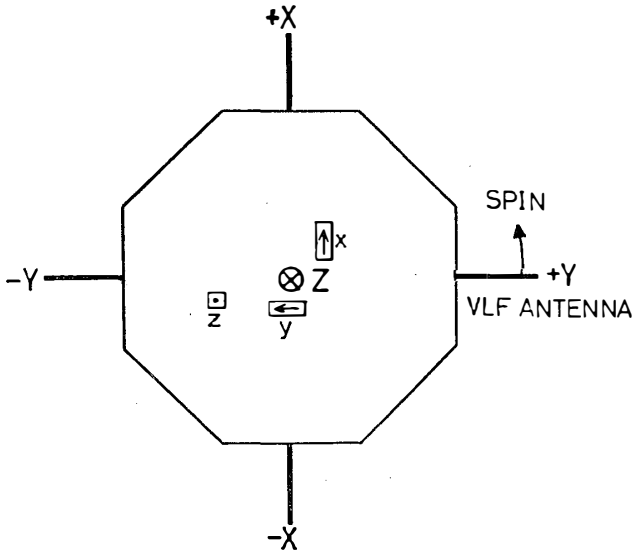

Fig. 15. Coordinate system and the allocations of the geomagnetic attitude sensor and VLF antenna of ISIS satellites. The spin axis of the satellite is parallel to Z-axis.

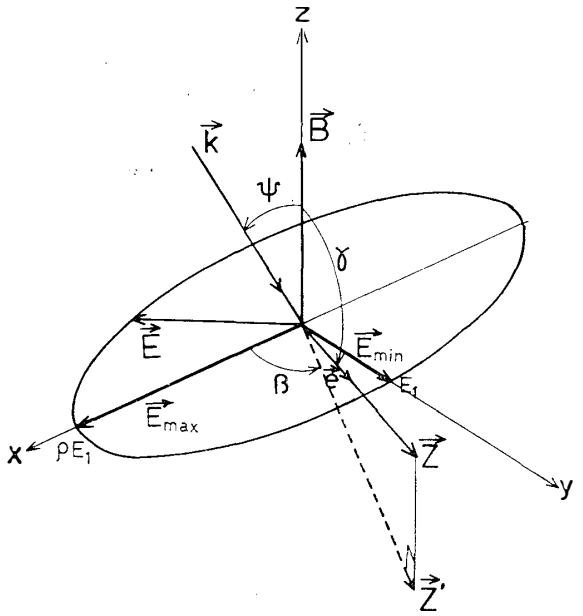

Fig. 16. Coordinate system used in the wave normal detection of ELF hiss. The earth's magnetic field $\boldsymbol{B}_0$ is parallel to Z-axis, and x-z plane includes the wave normal vector k.

In ELF range, the electric field of whistler mode wave is elliptically polarized in the x-y plane which is perpendicular to $\boldsymbol{B}_0$, and its ellipticity, ρ, is given by

$$\rho = 1/\cos\psi\,, \tag{17}$$

as described in Appendix 1. The wave electric field $\boldsymbol{E}$ is expressed with the spin phase angle Ω and two orthogonal vectors, $\boldsymbol{E}_{\min} \equiv E_1(0, 1, 0)$ and $\boldsymbol{E}_{\max} \equiv \rho E_1(1, 0, 0)$, as

$$\begin{aligned}\boldsymbol{E} &= \boldsymbol{E}_{\max}\cos\Omega + \boldsymbol{E}_{\min}\sin\Omega \\ &= E_1(\rho\cos\Omega,\ \sin\Omega,\ 0) \\ &= E_1(\cos\Omega/\cos\psi,\ \sin\Omega,\ 0)\ .\end{aligned} \tag{18}$$

As the plane of the antenna rotation, *i.e.* X-Y plane, does not coincide with the polarization plane of the wave electric field, the antenna detects the electric field component projected onto X-Y plane. This is shown in Fig. 17, where $\boldsymbol{E}'$ and $\boldsymbol{B}'_0$ are the projections of $\boldsymbol{E}$ and $\boldsymbol{B}_0$ onto X-Y plane and they are given by using a unit vector $\boldsymbol{e}\equiv$(sin

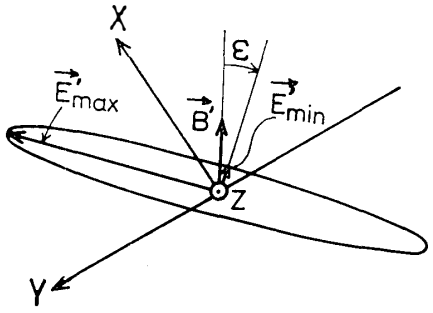

Fig. 17. Configuration of E' and B'_0, which are the projections of E and B_0 onto X-Y plane, in the coordinate system of ISIS satellite.

$\gamma\cos\beta,\ \sin\gamma\sin\beta,\ \cos\gamma$) along Z-axis as

$$\begin{aligned}\boldsymbol{E}' &= \boldsymbol{E} - (\boldsymbol{E}\cdot\boldsymbol{e})\boldsymbol{e} \\ &= E_1\{(1-\sin^2\gamma\cos^2\beta)\cos\Omega/\cos\psi - \sin^2\gamma\sin\beta\cos\beta\sin\Omega \\ &\quad - \sin^2\gamma\sin\beta\cos\beta\cos\Omega/\cos\psi + (1-\sin^2\gamma\sin^2\beta)\sin\Omega \\ &\quad - \sin\gamma\cos\gamma\cos\beta\cos\Omega/\cos\psi - \sin\gamma\cos\gamma\sin\beta\sin\Omega\}\ ,\end{aligned} \tag{19}$$

$$\begin{aligned}|\boldsymbol{E}'|^2 &= E_1^2\{\cos^2\Omega/\cos^2\psi + \sin^2\Omega \\ &\quad - \sin^2\gamma(\cos\beta\cos\Omega/\cos\psi + \sin\beta\sin\Omega)^2\}\ ,\end{aligned} \tag{20}$$

and

$$\begin{aligned}\boldsymbol{B}'_0 &= \boldsymbol{B}_0 - (\boldsymbol{B}_0\cdot\boldsymbol{e})\boldsymbol{e} \\ &= -B_0\sin\gamma(\cos\gamma\cos\beta,\ \cos\gamma\sin\beta,\ -\sin\gamma)\ ,\end{aligned} \tag{21}$$

where B_0 is the magnitude of the vector $\boldsymbol{B}_0$. $\boldsymbol{E}'$ is elliptically polarized in X-Y plane, and its maximum and minimum values are $\boldsymbol{E}'_{\max}$ and $\boldsymbol{E}'_{\min}$ as shown in the figure. The angles Ω_1 and Ω_2 which give $\boldsymbol{E}'_{\min}$ and $\boldsymbol{E}'_{\max}$ are obtained from the following equation,

$$\begin{aligned}\frac{\partial}{\partial\Omega}\left(\frac{|E'|^2}{E_1^2}\right) &= \{1-\sin^2\beta\sin^2\gamma-(1-\cos^2\beta\sin^2\gamma)/\cos^2\psi\}\sin^2\Omega \\ &\quad -(\sin^2\beta\sin^2\gamma/\cos\psi)\cos^2\Omega = 0\ ,\end{aligned} \tag{22}$$

and they are given as

$$\left.\begin{aligned}\Omega_1 &= \frac{1}{2}\tan^{-1}\left\{\frac{\sin^2\beta\sin^2\gamma/\cos\psi}{1-\sin^2\beta\sin^2\gamma-(1-\cos^2\beta\sin^2\gamma)/\cos^2\psi}\right\} \\ \Omega_2 &= \Omega_1 + \frac{\pi}{2}\ .\end{aligned}\right\} \tag{23}$$

The ellipticity of the polarization of $\boldsymbol{E}'$, defined as $\rho' \equiv |\boldsymbol{E}'_{\max}|/|\boldsymbol{E}'_{\min}|$, is expressed with Ω_1 and Ω_2 as

$$\rho' = \sqrt{\frac{\cos^2\Omega_2/\cos^2\psi + \sin^2\Omega_2 - \sin^2\gamma(\cos\beta\cos\Omega_2/\cos\psi + \sin\beta\sin\Omega_2)^2}{\cos^2\Omega_1/\cos^2\psi + \sin^2\Omega_1 - \sin^2\gamma(\cos\beta\cos\Omega_1/\cos\psi + \sin\beta\sin\Omega_1)^2}} \quad . \tag{24}$$

An angle ε between $\boldsymbol{B}'_0$ and $\boldsymbol{E}'_{\min}$ is given by

$$\varepsilon = \tan^{-1}\left\{\frac{(\boldsymbol{E}'_{\min} \times \boldsymbol{B}'_0)\cdot \boldsymbol{e}}{\boldsymbol{E}'_{\min}\cdot\boldsymbol{B}'_0}\right\} . \tag{25}$$

As γ is given by eq. (16), ρ' in eq. (24) is determined by ψ and β in a similar way as Ω_1 and Ω_2. By substituting Ω_1 for Ω in eq. (19), and considering eq. (16), $\boldsymbol{E}'_{\min}$ is given by ψ and β. From eq. (21), $\boldsymbol{B}'_0$ is determined by β. Hence ε, expressed by $\boldsymbol{E}'_{\min}$ and $\boldsymbol{B}'_0$ in eq. (25), can be also determined by ψ and β.

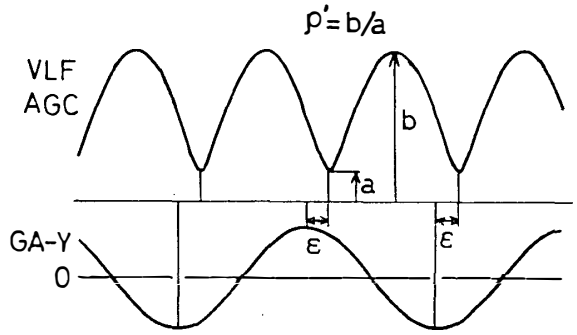

Fig. 18. A schematic illustration showing the relationship between VLF AGC and GA-Y waveforms. The definitions of ρ' and ε is shown in the figure.

Figure 18 illustrates the observed time-variation in VLF signal intensity and the Y component of the attitude sensor, GA-Y, on board ISIS satellite. The maximum and the minimum of VLF signal intensity, *i.e.* a and b, are obtained when the antenna becomes parallel to $\boldsymbol{E}'_{\max}$ and to $\boldsymbol{E}'_{\min}$, respectively. Therefore ρ' can be determined experimentally from the observed VLF signal intensity as follows

$$\rho' = |\boldsymbol{E}'_{\max}|/|\boldsymbol{E}'_{\min}| = b/a . \tag{26}$$

The angle ε is also obtained as a phase angle between the maximum of GA-Y and the minimum of VLF signal intensity. Therefore, β and ψ are inversely derived from ρ' and ε. This means that the direction of $\boldsymbol{k}$ is obtained by the spin modulated wave form of VLF signal intensity and the orientation of the receiving antenna.

As a simple example, a special case of $\gamma \simeq 0°$ (but is not exactly 0°) is considered. In this case, the spin axis is parallel to $\boldsymbol{B}_0$ and the plane of the antenna rotation coincides with the polarization plane of the wave electric field. The phase angles Ω_1 and Ω_2 are obtained from eq. (23) as 90° and 0°, respectively. By substituting these values for Ω in eq. (24), ρ' is given by

$$\rho' = 1/\cos\psi\,(=\rho) . \tag{27}$$

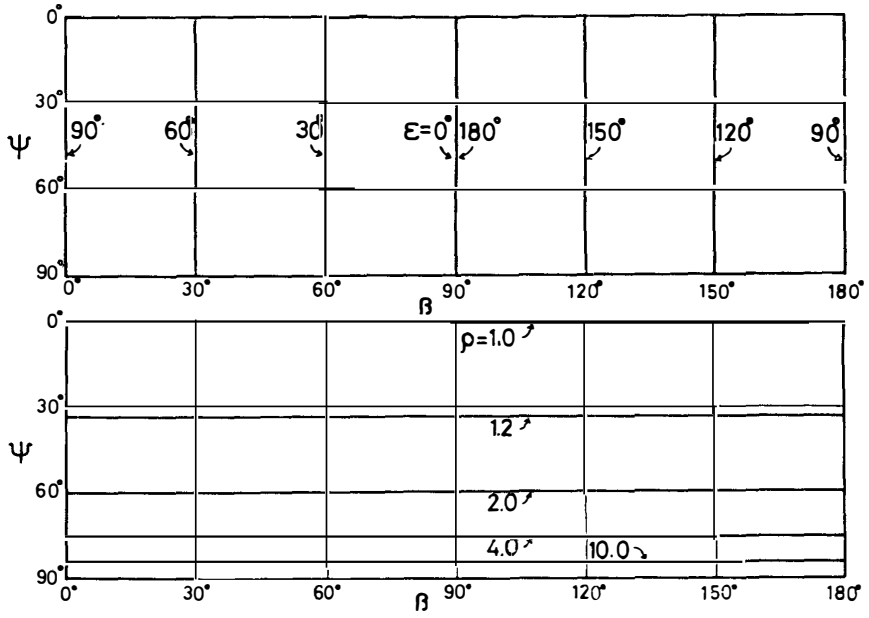

Fig. 19. Calculated value of ε and ρ′ in β-ψ plane for the case of γ≒0° (but is not exactly 0°).

$\boldsymbol{E}'_{\min}$ can be obtained by substituting 90° for Ω in eq. (19) as $E_1(0, 1, 0)$. Then, ε is calculated from eqs. (21) and (25) by using the above value of $\boldsymbol{E}'_{\min}$ as

$$\varepsilon = \tan^{-1}\left(\frac{\cos\beta}{\sin\beta}\right). \tag{28}$$

From eqs. (27) and (28), ρ' and ε are calculated for the variables of ψ and β and the results are shown in Fig. 19. In a general case with a finite value of γ, values of ρ' and ε can be calculated from eqs. (19), (21), (23), (24) and (25) for the variables of ψ and β, and the examples are shown later in Figs. 23 and 26. In this method, there is an uncertainty in ψ and β, *i.e.*, two values of ψ and $180°-\psi$ or that of β and $\beta+180°$ cannot be distinguished. This comes from the fact that the shape of the polarization of the wave electric field is identical for these wave normal directions. This method applied to ELF hiss data analysis is described in the following sections.

3.2.3. ISIS-2 observation on October 31, 1976

Figure 20 shows an example of ELF hiss observed by ISIS-2 satellite on October 31, 1976. The flight path of the satellite is shown in Fig. 21. In Fig. 20, the second panel from the top shows a frequency-time spectrogram of ELF hiss and the third panel shows AGC (automatic gain control) signal of the VLF receiver, which is equivalent to the intensity of received VLF wave electric field in a range of 0–25 kHz. In this event, there were no other emissions except this ELF hiss, so the AGC waveform represents the intensity of the ELF hiss. The bottom panel shows GA-Y, *i.e.* *Y*-component output from the geomagnetic attitude sensor. In the third panel, the VLF signal intensity is apparently modulated by the spinning motion of the satellite. There is a time lag between the maximum of GA-Y and the minimum of VLF AGC signals. This time lag, represented as a spin phase angle ε, is shown in the top panel with dots. This angle is the one between $\boldsymbol{B}'_0$ and $\boldsymbol{E}'_{\min}$ in Fig. 17. The top panel of Fig. 20 shows

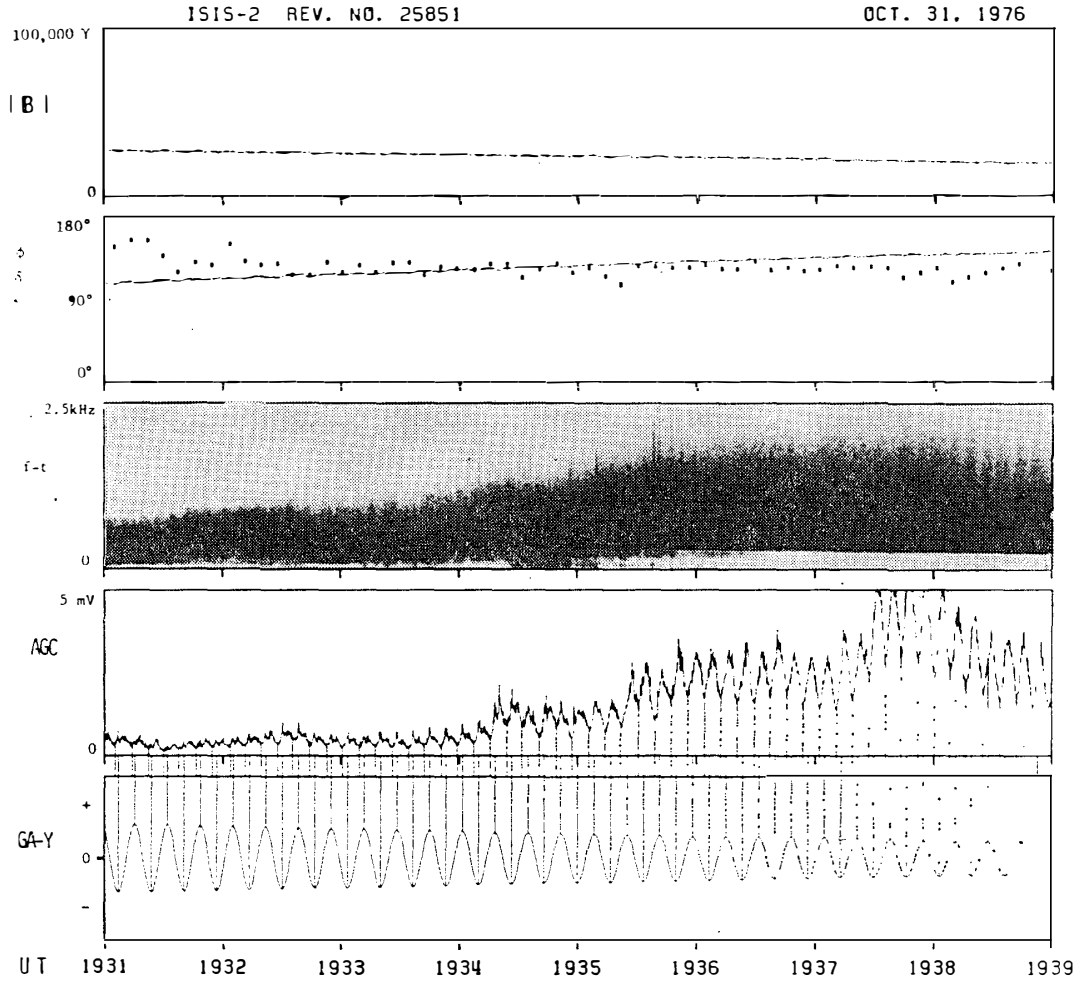

Fig. 20. An ELF hiss event observed by ISIS-2 satellite on October 31, 1976. The top panel shows an angle (by a line) between the spin axis of the satellite and B_0, and the angle (marked by dots) between the minimums of VLF AGC (given in the third panel) and the maximum of GA-Y (the fourth panel). The second panel shows a frequency-time spectrogram of ELF hiss.

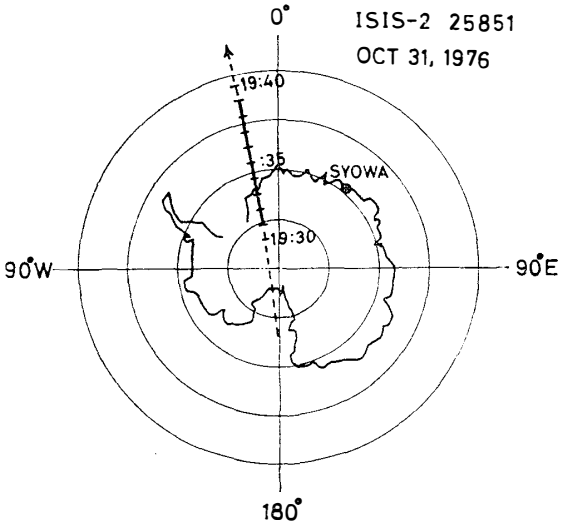

Fig. 21. A ground track of ISIS-2 satellite during the observation shown in Fig. 20.

also an angle γ between the spin axis of the satellite and the ambient magnetic field, which is determined by the geomagnetic attitude sensor.

At 1935 UT, the satellite was located at 68°S, 14.5°W, (56.9°S, 37.2°E in geomagnetic coordinates) at an altitude of 1400 km, where $B_0=0.13$ gauss, $N_e=10^4$ cm^{-3}, and $\gamma=138°$. Based on these values, ρ' and ε are calculated from eqs. (19), (21), (23), (24) and (25) for $f=500$ Hz, which is almost the center frequency of the ELF hiss at this time, with β and ψ as variables. The results are shown in Fig. 22. In the upper panel, there is a singular point at $\psi=42°$ (or 138°) and $\beta=0°$ (or 180°). This corresponds to the special case of $\gamma=\psi$ and $\beta=0°$, *i.e.*, the spin axis of the satellite is parallel to $\boldsymbol{k}$, where the electric field projected onto the plane of the antenna rotation is circularly polarized. In this case, the spin modulation of VLF signal disappears and ε becomes undeterminable.

From the observation, it was known that $\rho'=2.0$ and $\varepsilon=130°$. A set of β and ψ satisfying the above condition is obtained from Fig. 22 as a crossing point of two curves

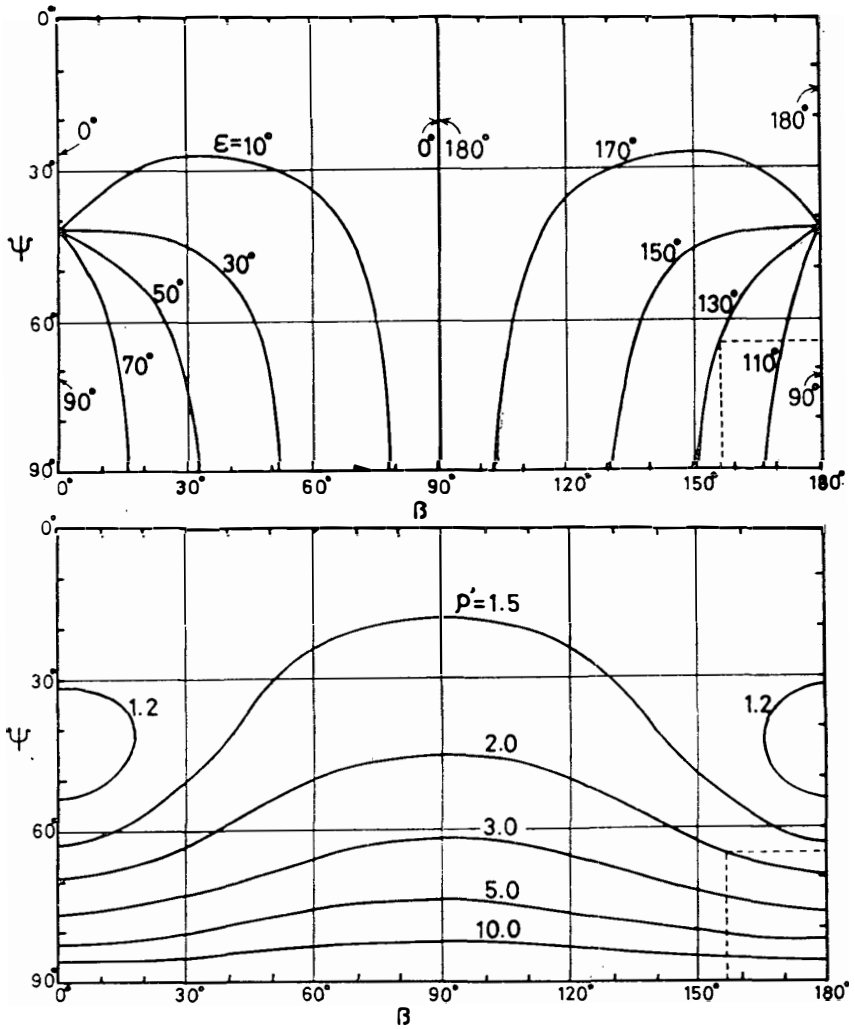

Fig. 22. Calculated curves of ε and ρ' in β-ψ plane for the case of $\gamma=138°$. Broken lines show a set of β and ψ which satisfies the observational value of ρ' and ε obtained at 1935 UT in the ELF hiss event shown in Fig. 20.

of $\rho'=2.0$ and $\varepsilon=130°$ in $\beta-\psi$ plane. As marked by broken lines in the diagrams, β is given as 156° (or 336°) and ψ is given as 64° (or 116°). In this way, the direction of wave normal $\boldsymbol{k}$ is determined with respect to the earth's magnetic field, $\boldsymbol{B}_0$, and the satellite spin axis, $\boldsymbol{Z}$. At this time, $\boldsymbol{Z}$ makes an angle of 132° with magnetic meridian, then $\boldsymbol{k}$ makes an angle of 24° (=156°−132°) with the magnetic meridian.

3.2.4. ISIS-1 observation on August 29, 1977

Figure 23 shows an example of ELF hiss observed by ISIS-1 satellite on August 29, 1977. The flight path of the satellite is shown in Fig. 24. In the top panel of Fig. 23, a frequency-time spectrogram of ELF hiss is shown. The second panel shows AGC signal of the VLF receiver and the bottom panel GA-Y signal. The spectrogram

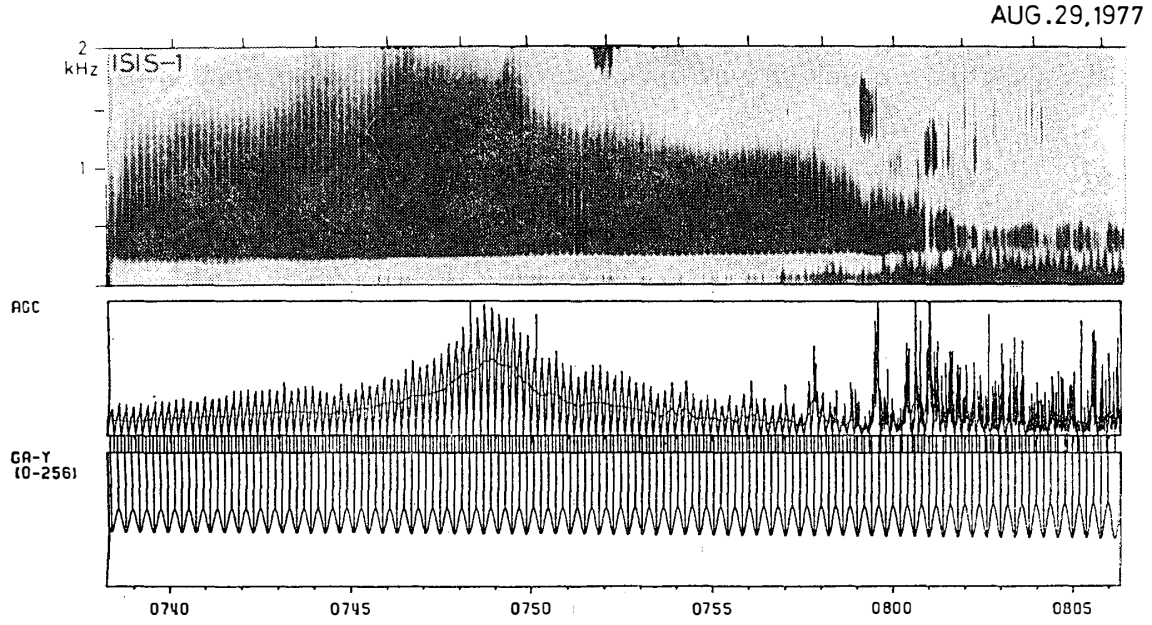

Fig. 23. An ELF hiss event observed by ISIS-1 satellite on August 29, 1977. A frequency-time spectrogram is shown in the top panel, and VLF AGC and GA-Y signal are shown in the middle and the bottom panels, respectively.

and the AGC signal are apparently modulated by the spinning motion of the satellite shown in the GA-Y waveform. The phase angle between the maximum of GA-Y and the minimum of AGC signal lies within 98°−120° with a median of 104°, while ρ' lies within 5–16. As a typical example, the observation at 0746 UT is analyzed. At this time, the satellite was located at 42.9°S, 37.0°E (57.2°S, 95.2°E in geomagnetic coordinates) at an altitude of 3508 km, where $\gamma=100°$, $B_0=0.114$ gauss, and $N_e=10^3\ \mathrm{cm}^{-3}$. Based on these values, ρ' and ε are calculated from eqs. (19), (21), (23), (24) and (25) for $f=500$ Hz for the variables of ψ and β. The results are shown in Fig. 25. As $\boldsymbol{Z}$ is almost perpendicular to $\boldsymbol{B}_0$ in this case, the characteristics of ε and ρ' in Fig. 25 is different from those in Fig. 22. When ε is close to 0° or 180°, ε is insensitive to β or ψ, and the β and ψ values determined by this method are unreliable. From the observation, it was known that $\varepsilon=104°$ and $\rho'=12.5$. A set of β and ψ satisfying the above condition is obtained from Fig. 25 as $\beta=177°$ and $\psi=88°$.

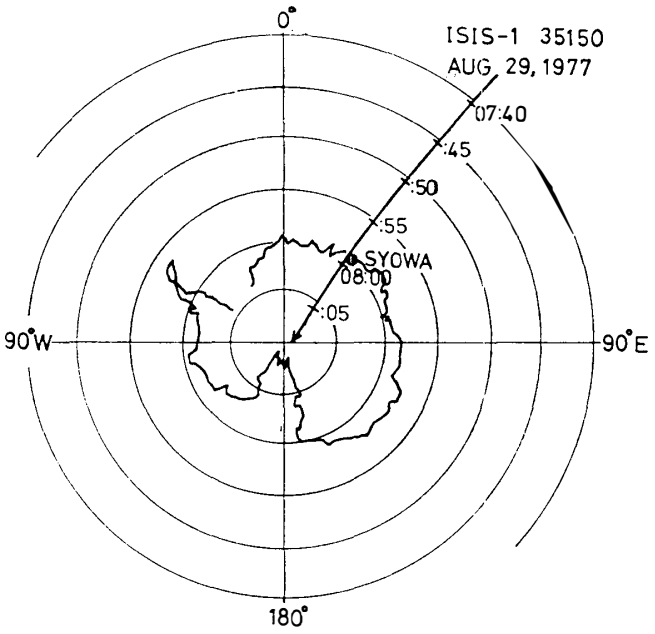

Fig. 24. A ground track of ISIS-1 satellite during the observation shown in Fig. 23.

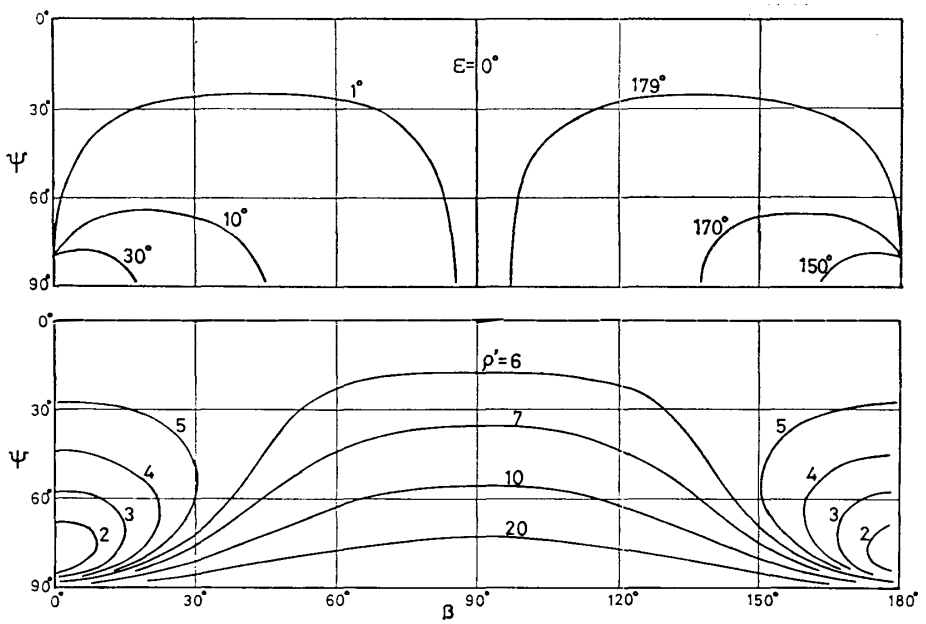

Fig. 25. Calculated curves of ε and ρ′ in β-ψ plane for the case of $\gamma=100°$.

3.2.5. Statistical analysis on the wave normal direction of ELF hiss

The orbit of ISIS-1 satellite is elliptical and its altitude varies during the observation period, while the orbit of ISIS-2 is almost circular and the altitude of the satellite is kept constant at about 1450 km. Considering Snell's law, the wave normal of ELF hiss is expected to be sensitive to the altitude below 3000 km, where the altitude dependence of electron density is great. Hence, it is better to use ISIS-2 data in the statistical analysis in order to exclude the scattering of the data due to the altitude dependence.

When the spin axis is almost perpendicular to $\boldsymbol{B}_0$, determination of β and ψ by this method is inaccurate due to the deformation of the polarization of wave electric field projected onto the plane of the antenna rotation. So, the observation under the condition of $80° < \gamma < 100°$ is omitted in the following statistics. In a period of October 1976–December 1979, 41 paths of ISIS-2 VLF observations are chosen, which satisfy the condition on γ mentioned above. The angles of β and ψ are obtained every 2 min when the satellite observed ELF hiss in these passes. Figure 26 shows the ψ values obtained from 41 passes of ISIS-2 VLF observations. In the figure, ψ is mainly distributed in a range of 50°–70°. Figure 27 shows the azimuthal angle of $\boldsymbol{k}$ in the plane perpendicular to $\boldsymbol{B}_0$. This angle is obtained from β and the direction of the spin axis with respect to the earth. The individual azimuthal angles of $\boldsymbol{k}$ are widely distributed over all directions but they are mostly concentrated within $\pm 25°$ of the geomagnetic meridian.

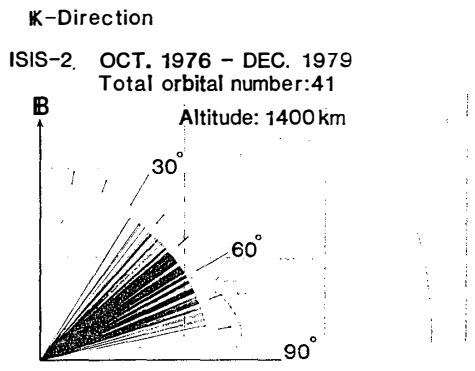

Fig. 26. Calculated wave normal angle ψ of ELF hiss obtained from 41 passes of ISIS-2 ELF/VLF observations.

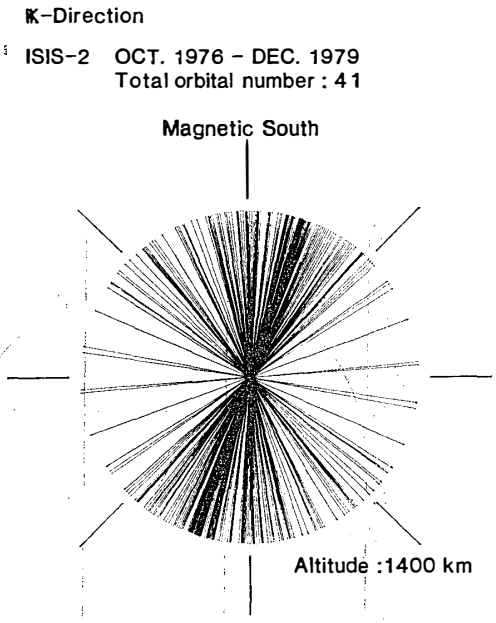

Fig. 27. Calculated azimuthal angles of ELF hiss obtained from 41 passes of ISIS-2 ELF/VLF observations.

3.2.6. Discussion and summary

If the ELF hiss observed in the polar ionosphere were propagating in nonducted mode, the ray tracing in Chapter 2 tells that the wave normal angle, ψ, is close towards 90° at the "turning point" of wave normal at an altitude of about 3000 km. Below the "turning point", most of the wave normal are concentrated at a certain direction which decreases with decreasing altitude. This decrease is understood by Snell's law, *i.e.* the increase of electron density in the lower latitude increases the refractive index of whistler mode wave and the wave normal tends to approach to the vertical in the lower altitude.

The altitude of ISIS-1 (3500 km) is very near to the level of the "turning point", and ISIS-2 made observations at an altitude well below the "turning point". Both

satellites very often observed ELF hiss whose intensity was modulated by the spinning motion of the satellite, and this means that the observed wave normals are collimated to a certain degree. The wave normal angle ψ obtained from the spin-modulated characteristic is almost 90° for ISIS-1 and 50°–70° for ISIS-2 observations. These results are consistent with the prediction by the ray tracing described above, and this supports the concepts of the "turning point" of wave normal and the "penetrating ray paths" introduced in the ray tracing in Chapter 2.

3.3. Multi-ion cutoff of ELF hiss observed by ISIS satellites

3.3.1. Introduction

In the power spectrum of ELF hiss observed in the polar ionosphere, sharp low-frequency cutoffs often appear near the proton gyrofrequency. GURNETT and BURNS (1968) studied this phenomenon with Injun 3 satellite. They found that one-third of the ELF hiss events observed had a recognizable low-frequency cutoff. These cutoffs have typical attenuations exceeding 20 dB in a 50 Hz frequency range. The cutoff frequencies decrease systematically with increasing altitude in the latitude range of 38°–60° INV, where INV denotes the invariant latitude, and they are within the range of $0.8f_{\mathrm{Hp}}$–f_{Hp}, where f_{Hp} denotes the local proton gyrofrequency. They explained this phenomenon as a multiple ion cutoff (or L=0 cutoff), *i.e.*, the polarization of a downgoing whistler mode wave is reversed from R to L at the altitude where the wave frequency is equal to the crossover frequency, f_{cr} (hereafter, this altitude is referred to as "crossover altitude"), and the left-handed polarization wave is succeedingly reflected at the altitude where the wave frequency is equal to the L=0 cutoff frequency, f_{L} (hereafter, this altitude is referred to as "L=0 altitude"). As f_{L} is determined by the local ion composition, the observed cutoff frequencies afford useful information on the ion composition in the polar ionosphere. The cutoff frequencies are also useful to estimate the incident angle of downgoing waves above the observation point. If the incident angle is close to the vertical, the reflection arises close to the "L=0 altitude". If the wave has a large incident angle, the reflection arises well above the "crossover altitude" (GURNETT and BURNS, 1968; ALTMAN *et al.*, 1975).

ELF hiss was often observed even below the L=0 cutoff frequency in the latitude higher than 60° INV, and this feature was explained by a mode coupling between the "fast R mode" and "slow R mode" waves near the crossover altitude. A cone of wave normal angle in which mode coupling efficiently arises is called "penetration cone", and was calculated to be 25° by a full-wave method (ALTMAN *et al.*, 1975). When the wave normals of downgoing waves occupy a considerable part of the "penetration cone", the attenuation at the low-frequency cutoff is decreased. Therefore, an amount of the attenuation at the cutoff can be used to estimate the wave normal distribution at the crossover altitude. For a strong attenuation (more than 20 dB) to arise, the wave normals of the downgoing waves at the crossover altitude must lie outside a cone whose axis is parallel to the earth's magnetic field, $\boldsymbol{B}_0$, and the half angle of 40° (ALTMAN *et al.*, 1975).

This section is devoted to the analyses of the low-frequency cutoff of ELF hiss observed by ISIS-1 and 2 satellites in two respects: the one is the relationship between the cutoff frequencies and the ion composition at the satellite altitude, and the other

is the relationship between the attenuation at the cutoff and the ion composition as well as the wave normal distribution of downgoing waves. GURNETT and BURNS (1968) analyzed the cutoff from the former aspect with Injun 3 satellite data. In their analysis, the latitude and the altitude dependence could not be separated due to an elliptic orbit of the satellite. In this work, an accurate latitude dependence is obtained by using the data of ISIS-2 satellite whose orbit is almost circular at an altitude of 1450 km. Besides, the ion composition observed by the same satellite (but at a different epoch) can be used for the comparison with ELF data.

In Section 3.3.2, seasonal variation of the occurrence of the lower cutoff is examined. In Section 3.3.3, latitudinal dependences of the lower cutoff frequency are

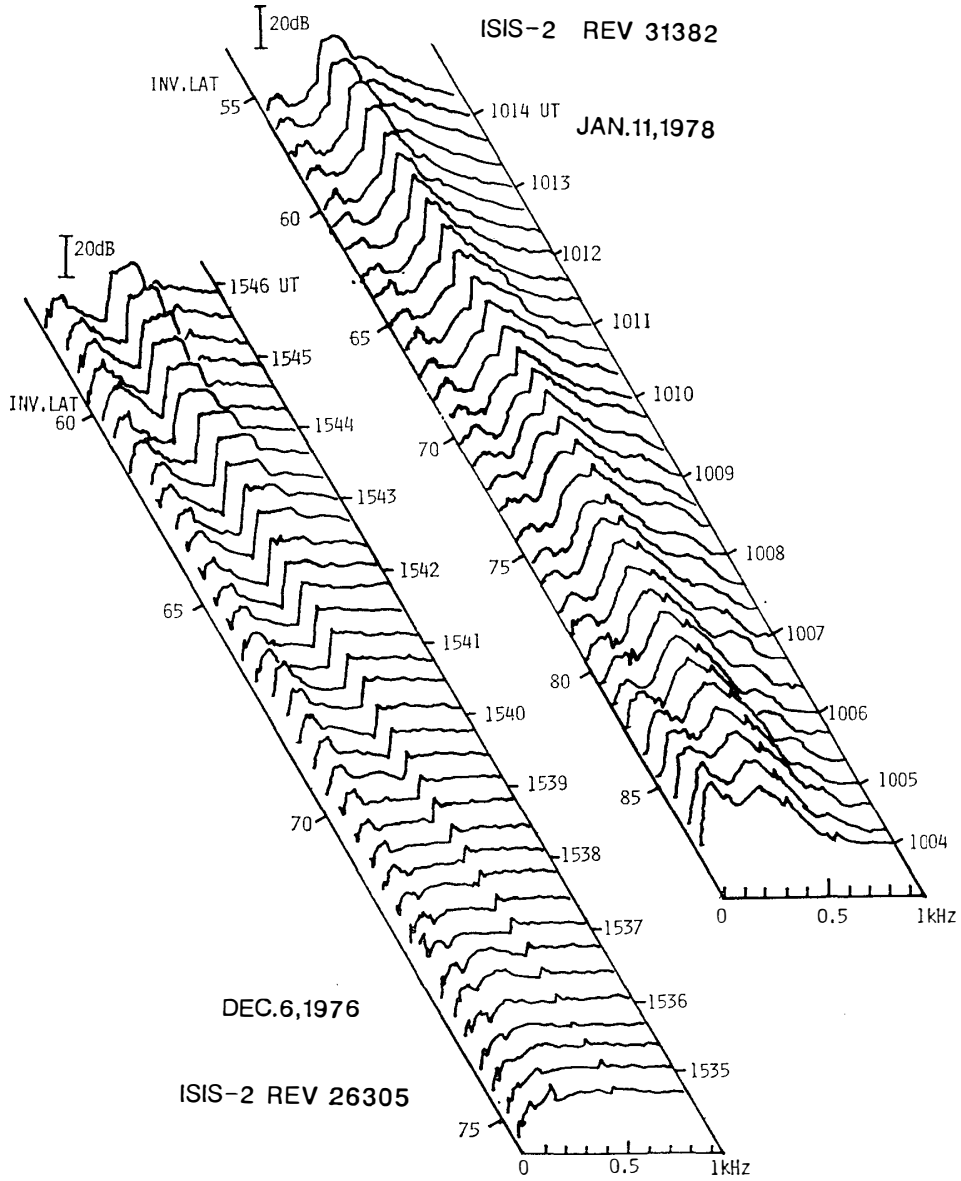

Fig. 28. Two series of power spectra of ELF hiss observed by ISIS-2 satellite passing over Antarctica on December 6, 1976 and January 11, 1978. The lower cutoff whose attenuation exceeds 20 dB is clearly recognized at 300–400 Hz in latitudes lower than 65° INV.

obtained for summer and winter seasons, and they are compared with f_{cr} and f_L calculated from the ion distribution observed by ISIS-2. In Section 3.3.4, the latitudinal dependence of the attenuation is elucidated for different conditions of geomagnetic activities. In Section 3.3.5, altitude dependence of the cutoff is examined by using ISIS-1 and 2 satellite data which were observed within a day. Finally in Section 3.3.6, intermode coupling at the crossover frequency is calculated by full wave method and the results are used to explain the disappearance of the cutoff in high latitudes as well as in winter. The wave normal distribution of ELF hiss obtained from the ray tracing in the preceding chapter is reviewed and it is compared with the satellite observations.

3.3.2. Seasonal variation of the lower cutoff occurrences

Figure 28 shows two series of power spectra of ELF hiss observed by ISIS-2 satellite passing over Antarctica on December 6, 1976 and January 11, 1978. The lower cutoff whose attenuation exceeds 20 dB is clearly recognized at 300–400 Hz in latitudes lower than 65° INV; however the attenuation at the cutoff decreases in the higher latitude. This latitudinal dependence is a common feature of these phenomena and will be examined in Section 3.3.4. ISIS-2 ELF/VLF observations over Antarctica in the winter of 1977 and the whole seasons of 1978 provided the data of 63 passes that cover a wide range of local time on the dayside and for various conditions of the geomagnetic activities. They are classified into four classes according to the values of the maximum attenuation at the cutoff of: (1) 0 dB (2) 0–10 dB, (3) 10–20 dB, (4) above 20 dB. Figure 29 shows a seasonal variation of the number of occurrence and the percentages of these four classes. It is clear that a strong attenuation predominates in summer, whereas the cutoff often disappears in winter. There are two possibilities

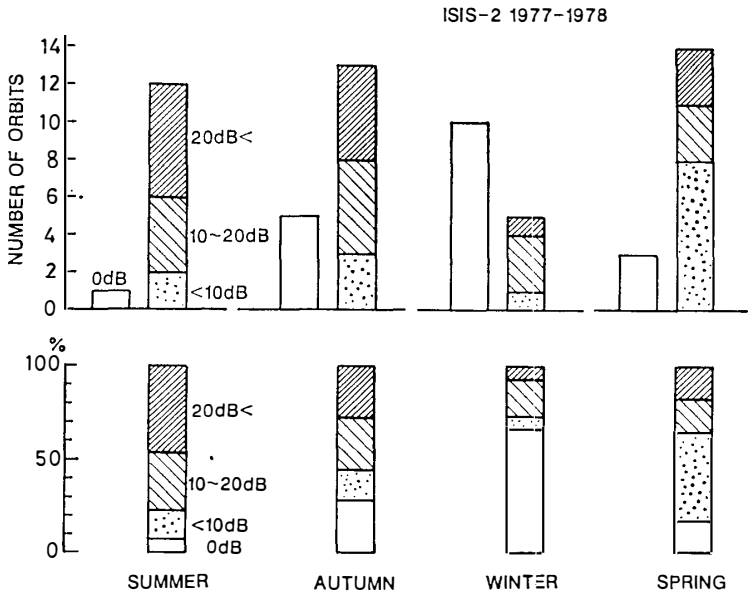

Fig. 29. A seasonal variation of the number of occurrence and the percentages of the four classes of ELF hiss lower cutoff: (1) 0 dB (2) 0–10 dB (3) 10–20 dB (4) above 20 dB. It is clear that a strong attenuation predominates in summer, whereas the cutoff often disappears in winter.

to explain this seasonal change. The one is an asymmetry in wave normal distribution between the summer and the winter hemisphere due to asymmetric electron density profiles along the propagation paths. If the wave normal of ELF hiss in winter occupies a considerable part of the "penetration cone", the lower cutoff disappears due to an increased intermode coupling at f_{cr}. However, no observational evidence was found yet to support this idea.

Another possibility is that the ion composition in summer is favorable for the multiple ion cutoff of ELF waves. Figure 30 shows fractional abundances of ions at the altitude of about 1450 km in high latitudes observed by ISIS-2 in 1972 (HOFFMAN and DODSON, 1980). The upper panel shows those observed in summer, in which O^+ dominates over the whole latitudinal range higher than 55° INV. The lower panel shows those in winter. There is a notable depression of total ion concentration at the auroral zone around 65° INV, and there are transitions of dominant ions from H^+ to O^+, or *vice versa* in the polar cap and in the subauroral zone. For the plasma with three ion species O^+, H_e^+ and H^+, there are two f_{cr}'s and f_L's. The one is higher than the helium gyrofrequency, $f_H(H_e^+)$, and the other is lower than that frequency, and they are hereafter referred to as f_{cr1}, f_{L1}, and f_{cr2}, f_{L2}, respectively. The change in the dominant ion species from O^+ to H^+ can result in the transition of the lower cutoff frequency from f_{L1} to f_{L2}. The cutoff below $f_H(H_e^+)$ is usually difficult to find out

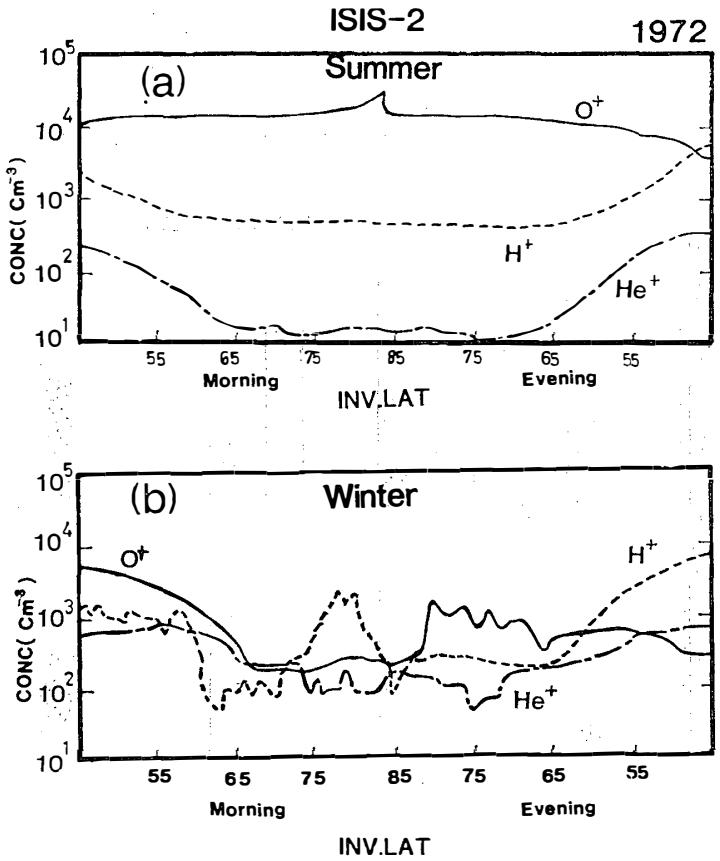

Fig. 30. Fractional abundances of ions at the altitude of 1450 km in high latitudes in summer (a) and in winter (b) observed by ISIS-2 in 1972 (after HOFFMAN and DODSON, 1980).

because its frequency is very close to the band edge of the VLF receiver on board ISIS satellites. In the data used for the statistics of Fig. 29, the lower cutoff whose frequency is less than $f_H(H_e^+)$ is not included. Therefore, it is very likely that the cutoffs are occasionally missed in winter when the dominant ion species changes from O^+ to H^+. This possibility will be discussed in more detail in Sections 3.3.3 and 3.3.6.

3.3.3. Latitudinal dependence of the lower-cutoff frequencies

Figures 31 and 32 show latitudinal dependences of the normalized crossover frequencies, f_{cr1}/f_{Hp} and f_{cr2}/f_{Hp}, and the normalized cutoff frequencies, f_{L1}/f_{Hp} and f_{L2}/f_{Hp}, calculated from the summer and winter ion compositions illustrated in the bottom panels, which are derived from the ion fractional abundances shown in Fig. 30. In Fig. 31, which represents the summertime condition, f_{L1} is within 0.9 of f_{Hp} in the latitude higher than 60° INV, whereas in winter (Fig. 32), f_{L1} changes widely from $0.9f_{Hp}$ to $0.3f_{Hp}$ as the dominant ion changes from O^+ to H^+. The observed lower-cutoff frequency is close to, but is not exactly f_L, and the frequency difference

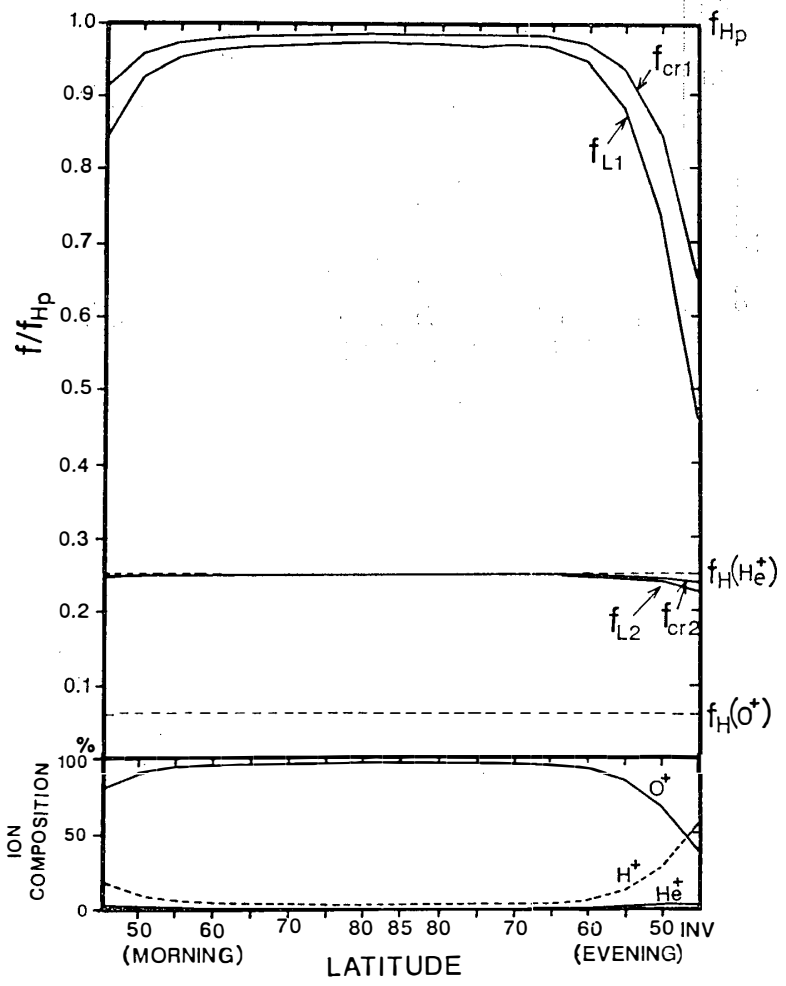

Fig. 31. Latitudinal dependences of the normalized crossover frequencies, f_{cr1}/f_{Hp} and f_{cr2}/f_{Hp}, and the cutoff frequencies, f_{L1}/f_{Hp} and f_{L2}/f_{Hp}, in summer calculated from the ion composition illustrated in the bottom panel, which is derived from the ion fractional abundances shown in Fig. 30a.

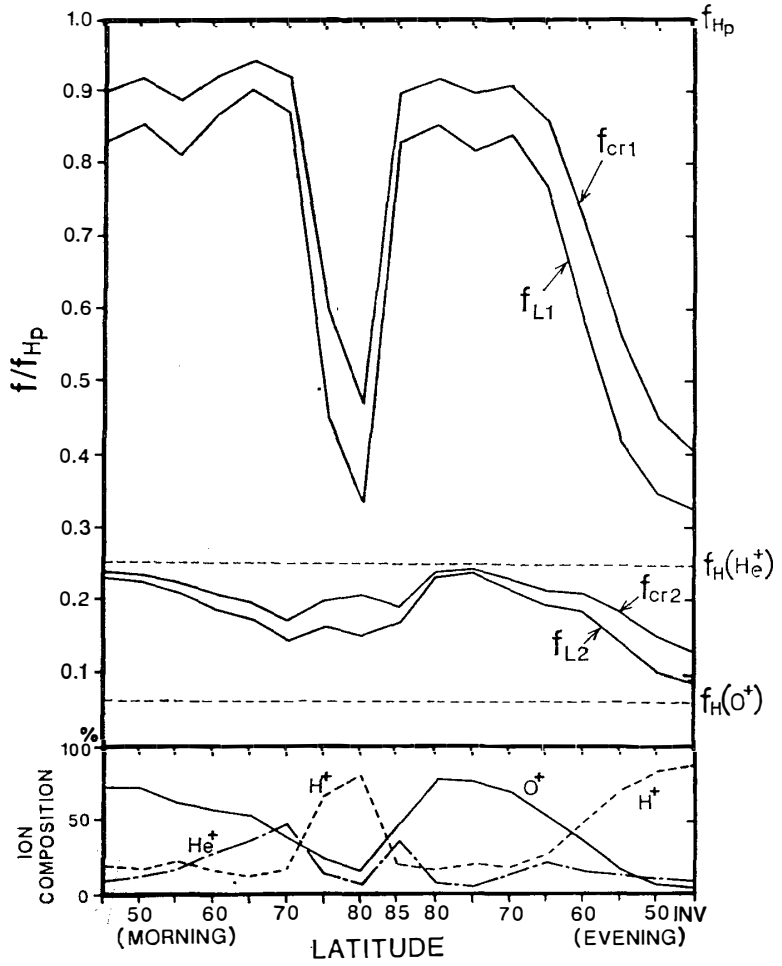

Fig. 32. The same as Fig. 31, except that the wintertime ion composition shown in the bottom panel is assumed. The ion composition is derived from the ion fractional abundances shown in Fig. 30b.

between the both frequencies is strongly dependent upon the initial wave normal angle (GURNETT and BURNS, 1968). In the following, the relationship between the calculated frequencies, f_{cr}, f_L, and the observed cutoff frequencies is discussed.

In the power spectrum of ELF hiss which shows a lower cutoff, the slope at the cutoff is generally very steep, but has a finite bandwidth of f. It varies from 5 Hz to 40 Hz with the median of 15 Hz for the attenuation of 20 dB. This slope is considered to be closely related to the wave normal distribution of the incident wave (GURNETT and BURNS, 1968). Figure 33 schematically illustrates these characteristic relations, where f_{Hp}, f_{cr} and f_L are shown as functions of altitude. At an altitude of 1450 km, f_{cr} and f_L are assumed to be 400 Hz and 380 Hz, respectively, and they are marked by circles and triangles in the figure. Here it is assumed that these ELF waves are propagating downwards with various wave normal directions. Figure 33 shows also refractive indices of 380 Hz and 400 Hz waves with certain initial wave normal angles as functions of altitude. They are initially propagating in R-mode. When the wave approaches the crossover altitude at 1450 km, the refractive indices of R-mode decrease and the wave having a large initial wave normal angle undergoes reflection

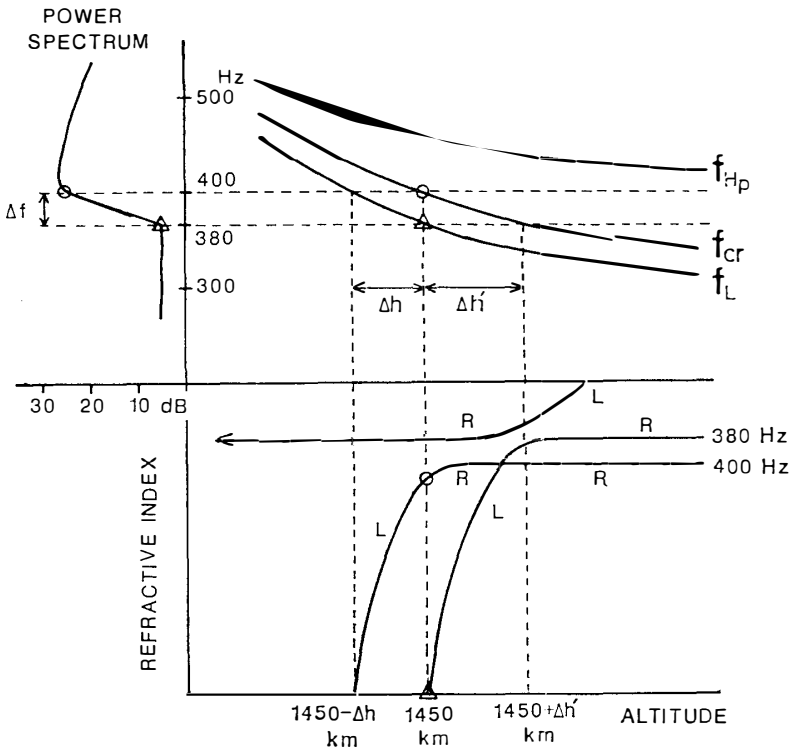

Fig. 33. A schematic illustration of the relationship between the power spectral shape of ELF hiss with low-frequency cutoff and the profiles of characteristic frequencies, f_{Hp}, f_{cr} and f_L, and refractive indices of 380 Hz and 400 Hz waves. Distances Δh and $\Delta h'$ denote altitude differences between crossover and $L=0$ altitudes for 380 Hz wave and 400 Hz wave, respectively.

in *R*-mode. If the initial wave normal angle is sufficiently small, the wave passes through the crossover altitude and the polarization is reversed to *L*-mode as marked by a circle in the figure. Below the crossover altitude, the refractive indices of *L*-mode decrease rapidly and eventually reach zero at the $L=0$ altitude. Due to this rapid decrease, most of the waves undergo reflection above the $L=0$ altitude in *L*-mode. In a similar way, 380 Hz waves propagating downwards experience a polarization reversal from *R* to *L* at the crossover altitude for 380 Hz wave which is a little higher than 1450 km, and these *L*-mode waves are completely reflected at the $L=0$ altitude of 1450 km as marked by triangles. However, if some of the wave normals have a small angle with the earth's magnetic field at the crossover altitude, considerable wave energy can be transferred from the fast *R*-mode (lower branch) to the slow *R*-mode (upper branch) as marked by an arrow in the figure. This wave component passes through the $L=0$ altitude and continues to propagate downwards. This corresponds to the residual part below the cutoff in the power spectrum shown on the left side. From these characteristics, it is reasonable to relate f_{cr} and f_L with the upper and the lower edges of the slope at the cutoff in the power spectrum. Hereafter, the above edge frequencies are referred to as f_{cu} and f_{cl}, and in order to confirm such an inference, they are to be compared with f_{cr} and f_L calculated from the ion concentration models shown in Figs. 31 and 32.

Figure 34 shows latitudinal variations of the cutoff frequencies, f_{cu} and f_{cl} (illustrated by vertical bars in the lower panel), and the amount of attenuation at the cutoff (upper panel) observed by ISIS-2 in austral summer at 1002–1014 UT (05–09 MLT) on January 11, 1978. Solid lines in the lower panel are the calculated values of f_{cr} and f_L. The f_{cl}'s are close to, but slightly lower than f_L as much as 8 Hz. This small frequency difference is possibly due to a difference in ion composition between the epoch of this observation and that of the ion observation by HOFFMAN and DODSON in 1972. A decrease of the major ion (O^+) composition from 96% observed in 1972 to 94% can account for the above frequency difference. In the lower latitude, f_{cu} exceeds calculated f_{cr} or even f_{Hp}. This suggests that the incident angle of ELF hiss is large in this latitude range.

Figure 35 shows a result similar to Fig. 34, observed by ISIS-2 in the austral winter at 0827–0835 UT (07–09 MLT) on July 21, 1977. The observed cutoff frequencies marked by vertical bars in the lower panel show a sharp decrease in the latitude higher than 70° INV, and this cutoff disappears at 71.8° INV. However at this latitude,

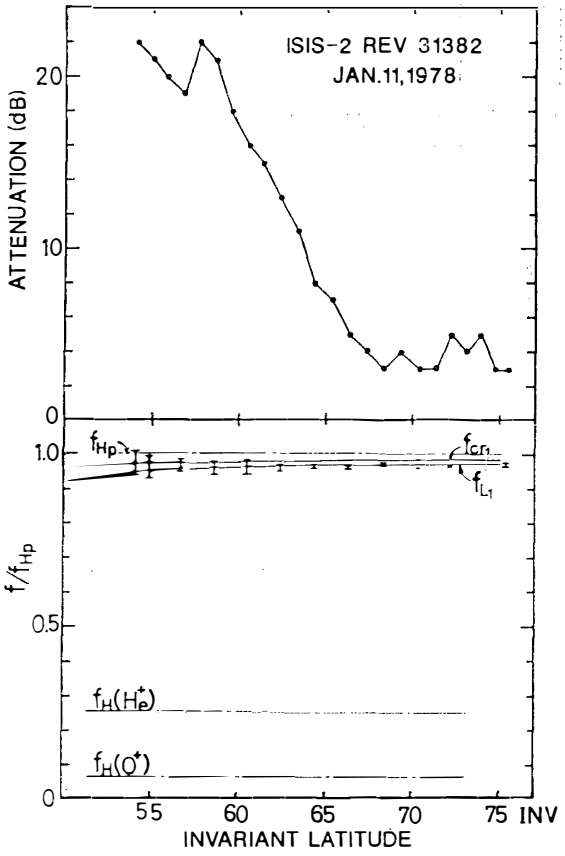

Fig. 34. Latitudinal variations of the amount of attenuation at the cutoff (upper panel) and the cutoff frequencies, f_{cu} and f_{cl} (illustrated by vertical bars in the lower panel), observed by ISIS-2 in austral summer at 1002–1014 UT (05–09 MLT) on January 11, 1978. Solid lines in the lower panel are the calculated values of f_{cr} and f_L.

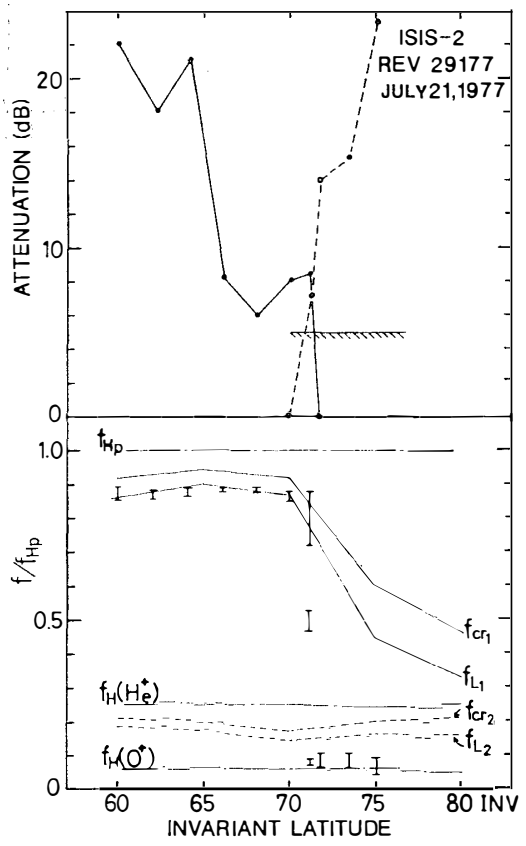

Fig. 35. A result similar to Fig. 34, observed by ISIS-2 in the austral winter at 0827–0835 UT (07–09 MLT) on July 21, 1977.

another cutoff is newly formed below $f_H(H_e^+)$. The attenuation at the former cutoff is shown by solid line in the top panel, and the latter one by broken line. The observed cutoff frequency higher than $f_H(H_e^+)$ coincides with f_{L1}, however the one less than $f_H(H_e^+)$ is much lower than f_{L2}. This means that the light ion (H^+ or H_e^+) dominated in the latitudes higher than 72°, and the ion composition in this latitude range was different from the model shown in the bottom panel of Fig. 32. This notable difference between the observed cutoff frequencies and the model calculation is due to a high variability in the ion composition in winter as seen in Fig. 30. It should also be noted that the cutoff frequencies lower than $f_H(H_e^+)$ are usually located at 30–50 Hz and this is almost the band edge of the VLF receivers on board ISIS satellites. For ISIS-2, the attenuation due to the low frequency response of the receiver is 5 dB at 30–50 Hz. In Fig. 35, the attenuation due to the receiver is marked by a hatched line in the top panel.

The transition of the lower-cutoff frequencies between f_{L1} and f_{L2} is not rare but a general feature in winter. However the cutoff near f_{L2} is often missed due to a limited bandwidth of the receiver mentioned above, and this is a possible reason why the occurrence of the lower cutoff decreases in winter as shown in Fig. 29.

Presented in Fig. 36 is a plot of f_c/f_{Hp} *vs.* invariant latitude obtained from 13 passes

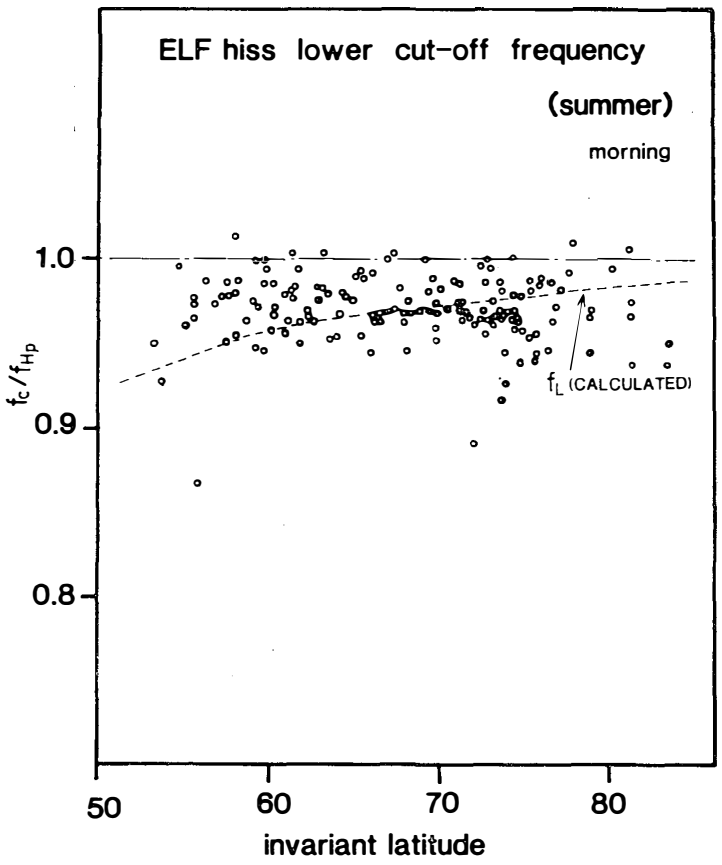

Fig. 36. A plot of f_c/f_{Hp} vs. invariant latitude obtained from 13 passes of ISIS-2 ELF observation in the summer of 1978, where f_c is a mean of f_{cu} and f_{cl}. The broken line in the figure indicates f_L/f_{Hp} calculated from the summertime ion composition model shown in Fig. 31.

of ISIS-2 ELF observation in the summer of 1978, where f_c is a mean of f_{cu} and f_{cl}. Average *Kp* index during these observation was 2.7. The broken line in the figure indicates f_L/f_{Hp} calculated from the model ion composition shown in Fig. 31. More than 92 of the observed cutoff frequency, f_c/f_{Hp}, is distributed within 4% of f_L/f_{Hp}. This supports the validity of the ion composition model in summer. A small frequency difference between f_c and f_L is attributable either to the oblique incidence of ELF waves in which the reflection occurs above the $L=0$ altitude, or to a difference in ion composition between present ELF wave observation in 1978 and the ion observation in 1972. The former explains f_c's above f_L, whereas the latter explains f_c's both above and below f_L. A change in O^+ ion composition of $\pm 4\%$ from the summertime model accounts for the above frequency difference. Figure 37 shows a similar plot of f_c/f_{Hp} obtained from 15 passes of ISIS-2 ELF observation in the winter of 1977 and 1978. The average *Kp* index for these observations was 2.2. The normalized frequencies f_{cr}/f_{Hp} and f_L/f_{Hp}, calculated from the wintertime ion composition model shown in Fig. 32, are also indicated in the figure. The f_c/f_{Hp}'s scatter widely from 1.0 to 0.72, in consistence with the variability of f_{cr} and f_L shown in Fig. 30. Note that for latitudes higher than 71° INV, the occurrence of the cutoff is very rare. This will be attributable

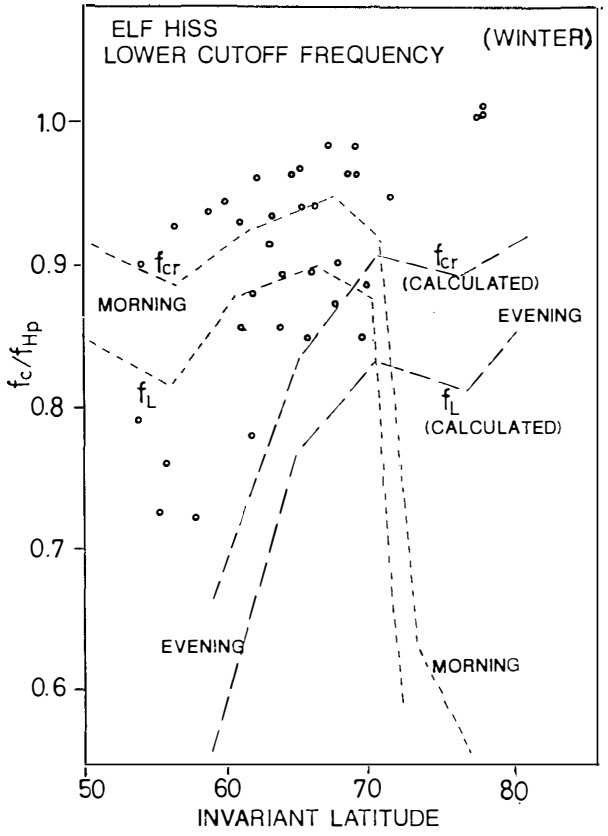

Fig. 37. A plot of f_c/f_{Hp} vs. invariant latitude obtained from 15 passes of ISIS-2 ELF observation in the winter of 1977 and 1978. The normalized frequencies f_{cr}/f_{Hp} and f_L/f_{Hp}, calculated from the wintertime ion composition model shown in Fig. 32, are also indicated in the figure.

to the transition of predominant ions from O^+ to H^+ in the morning sector, where the lower-cutoff frequency is expected to change from f_{L1} to f_{L2}. It is very likely that the cutoff near f_{L2} is missed due to the limited bandwidth of the receiver on board ISIS-2.

3.3.4. Latitudinal dependence of the attenuation at the cutoff

As shown in Figs. 34 and 35, the attenuation at the cutoff decreases with increasing latitude. In order to obtain a general feature of this latitudinal dependence, 14 passes of ISIS-2 data in the summer of 1978 were analyzed. According to the geomagnetic activity, they are classified into three groups: (1) $Kp<2$, (2) $2\leq Kp<3$, and (3) $Kp\geq 3$. A latitudinal dependence of the attenuation for each group is shown in Figs. 38 to 40. The observed cutoff frequencies are shown in the bottom panel of these figures. Under quiet condition shown in Fig. 38, the attenuation shows a steep decrease in the latitudes greater than 64° INV. Under moderately disturbed condition shown in Fig. 39, the attenuation starts to decrease at 60° INV. It reaches 5 dB at 70° INV, and keeps that level in 70°–75° INV. Under disturbed condition shown in Fig. 40, the attenuation is generally less than 10 dB and increases with increasing latitude above

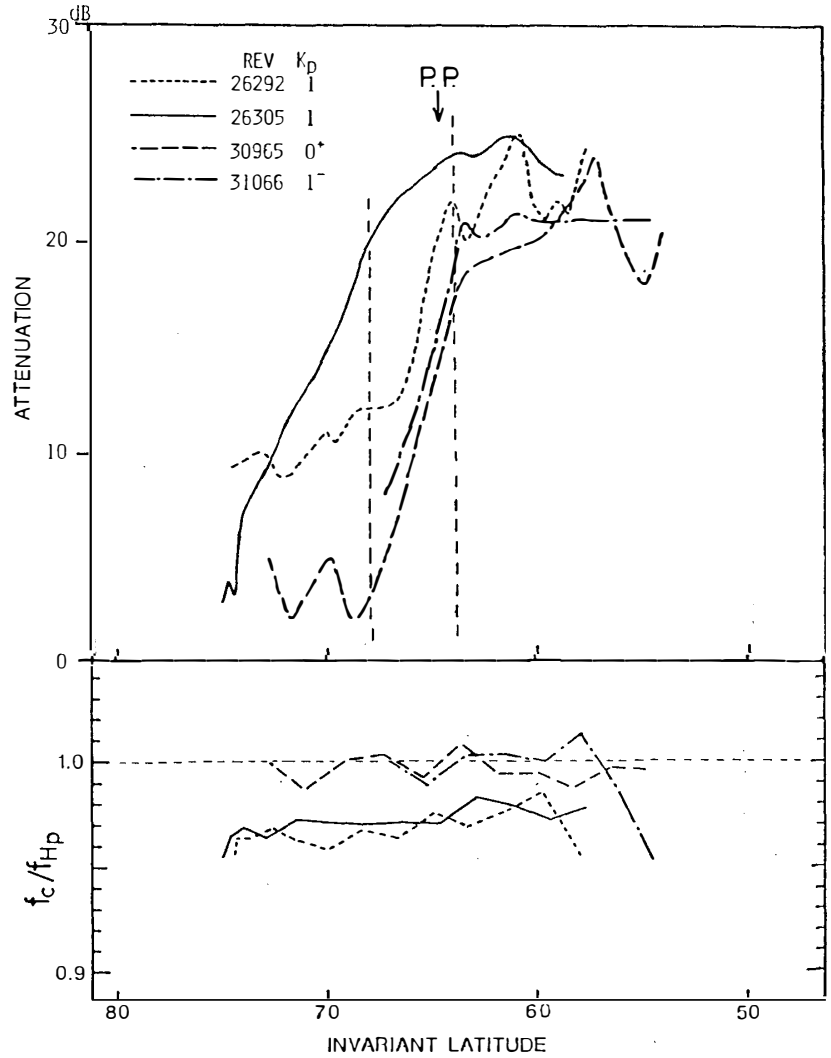

Fig. 38. A latitudinal dependence of the attenuation at the multiple ion cutoff observed under the geomagnetic activity of $Kp<2$.

65° INV, which is opposite to other cases. A latitudinal range where the attenuation shows a steep decrease is marked by vertical broken lines in these figures. This range moves according to the geomagnetic activities. This shows a similarity to the motion of the plasmapause position, which is inferred from an empirical relation of $L_{pp}=6.0-0.6\,Kp$ given by BINSACK (1967), where L_{pp} denotes the L-value of the plasmapause. In Figs. 38 to 40, the plasmapause position obtained from the above relation is marked by an arrow. It seems that the attenuation starts to decrease just outside the plasmapause. The attenuation at the multiple-ion cutoff is given by the mode coupling rate from the "fast R mode" to "slow R mode" at the crossover altitude (see Fig. 33), which depends on the incident wave normal angle of ELF waves with respect to the earth's magnetic field, and/or the distance in altitude between the crossover and the $L=0$ altitude (*e.g.*, Δh or $\Delta h'$ in Fig. 33). The distance Δh can be determined by the ion composition profile, and it becomes as small as the wavelength of whistler mode ELF waves when the ion concentration ratio of H^+ to O^+ decreases well below 0.1 (see Fig. 45 in Section 3.3.6). In this condition, the attenuation at the multiple-ion cutoff decreases due to an increased mode coupling rate between fast

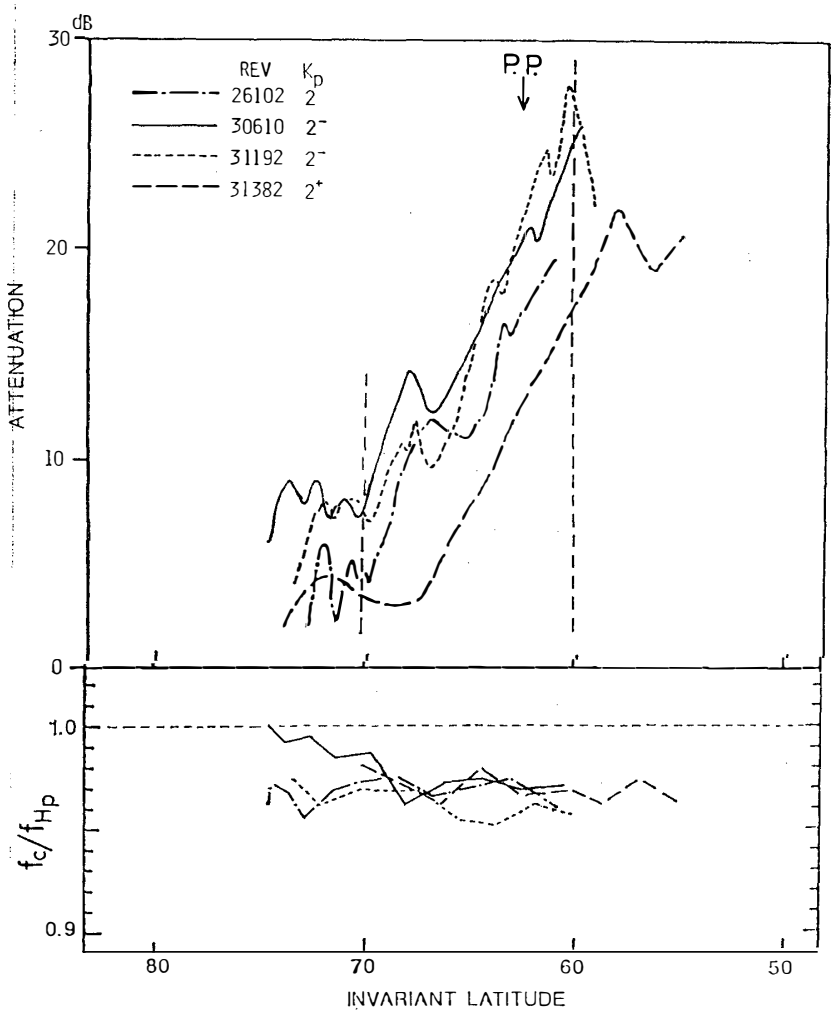

Fig. 39. The same as Fig. 38, except for the geomagnetic activity of $2\leq Kp<3$.

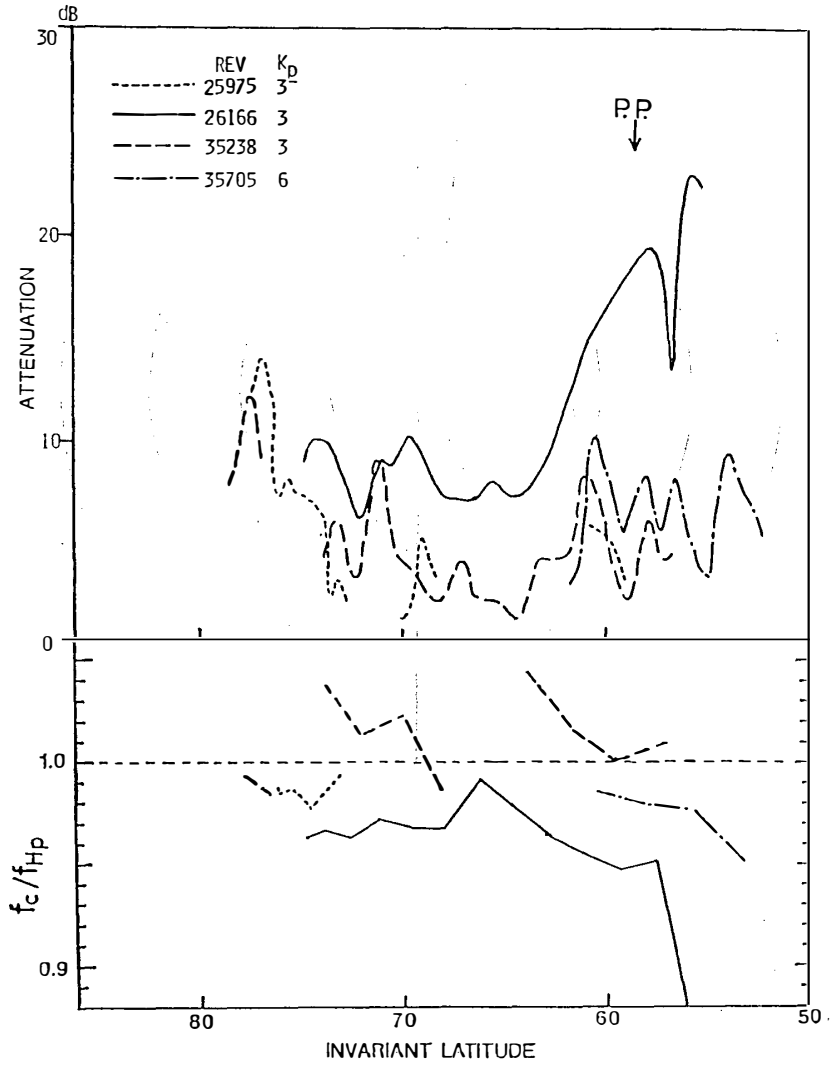

Fig. 40. The same as Fig. 38, except for the geomagnetic activity of Kp≥3.

R-mode and slow *R*-mode (see Fig. 33). In fact, Fig. 30 shows that the ion concentration ratio of H^+ to O^+ in the summer ionosphere decreases from 0.1 to 0.05 in the latitude range from 60° to 70° INV, where the attenuation at the multiple-ion cutoff often shows decrement from 20 dB to 5 dB as shown in Figs. 38–40. This latitudinal decrease of the cutoff will be discussed in Section 3.3.6 in terms of the full wave analysis of the mode coupling.

3.3.5. Altitude dependence of the cutoff observed by two satellites

The altitude dependence of the cutoff is investigated using ISIS-1 and 2 satellites, whose observations were made closely in time (within 22 hours) and under similar conditions in local time and in geomagnetic activity. Figure 41 shows ground tracks of ISIS-2 revolution of 31382 in the period of 1004–1014 UT on January 11, 1978 and ISIS-1 36676 of 0740–0800 UT on January 12, 1978. The satellite altitude was 1450 km for ISIS-2 and 2915–3530 km for ISIS-1. The *Kp* index at the time of the observation was 1^+ for both observations, and the local time of the satellite was 0700–0930 for ISIS-2 and 1230–1400 for ISIS-1.

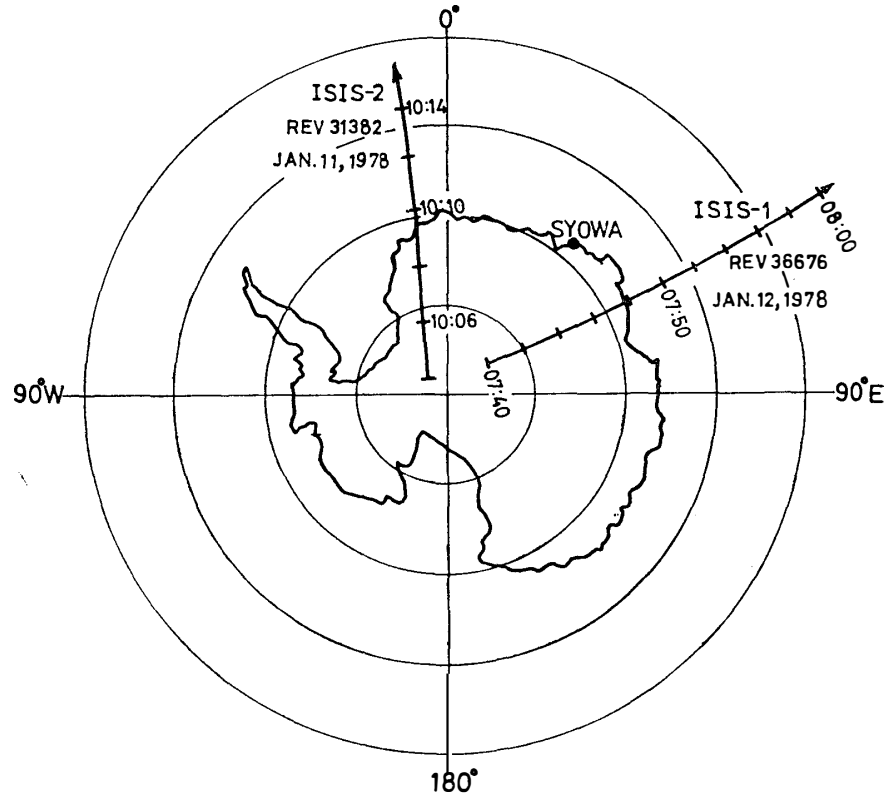

Fig. 41. Ground tracks of ISIS-2 satellite revolution of 31382 in the period of 1004–1014 UT (0700–0930 LT) on January 11, 1978, and ISIS-1 36676 of 0740–0800 UT (1230–1400 LT) on January 12, 1978. The satellite altitude was 1450 km for ISIS-2 and 2915–3530 km for ISIS-1.

Figure 42 shows latitudinal dependence of the attenuation and the cutoff frequency of multiple ion cutoff observed by the both satellites. A common feature of decreasing attenuation with increasing latitude is recognizable. In the top panel, the attenuation curves for the waves from these satellites are compared (solid line: ISIS-1, broken line: ISIS-2). The attenuation observed at a higher altitude (ISIS-1) is greater than that observed at a lower altitude (ISIS-2) by 4 to 12 dB. This can be explained by the change of wave normal direction with altitude according to Snell's law as will be discussed in Section 3.3.6.

The cutoff frequency observed at the higher altitude is lower than the other by 15%. This suggests that the fractional abundance of the light ion increases at the higher altitude. As the observation was made in the austral summer, the major ion constituents at the satellite level were O^+ and H^+ as shown in Fig. 30. The ratio of these two ions can be estimated from the observed cutoff frequency by using the following equation,

$$f_{c1} = f_L = f_{Hp}(\eta_O + \eta_H / 16), \tag{29}$$

where η_O and η_H are the fractional abundances of O^+ and H^+ ions, respectively. The estimated ion compositions are shown in the third (ISIS-1) and sixth (ISIS-2) panels from the top. The relative abundance of H^+ ion is greater at higher altitudes. This is due to the fact that the scale-height of H^+ ion is much greater than that of O^+ ion.

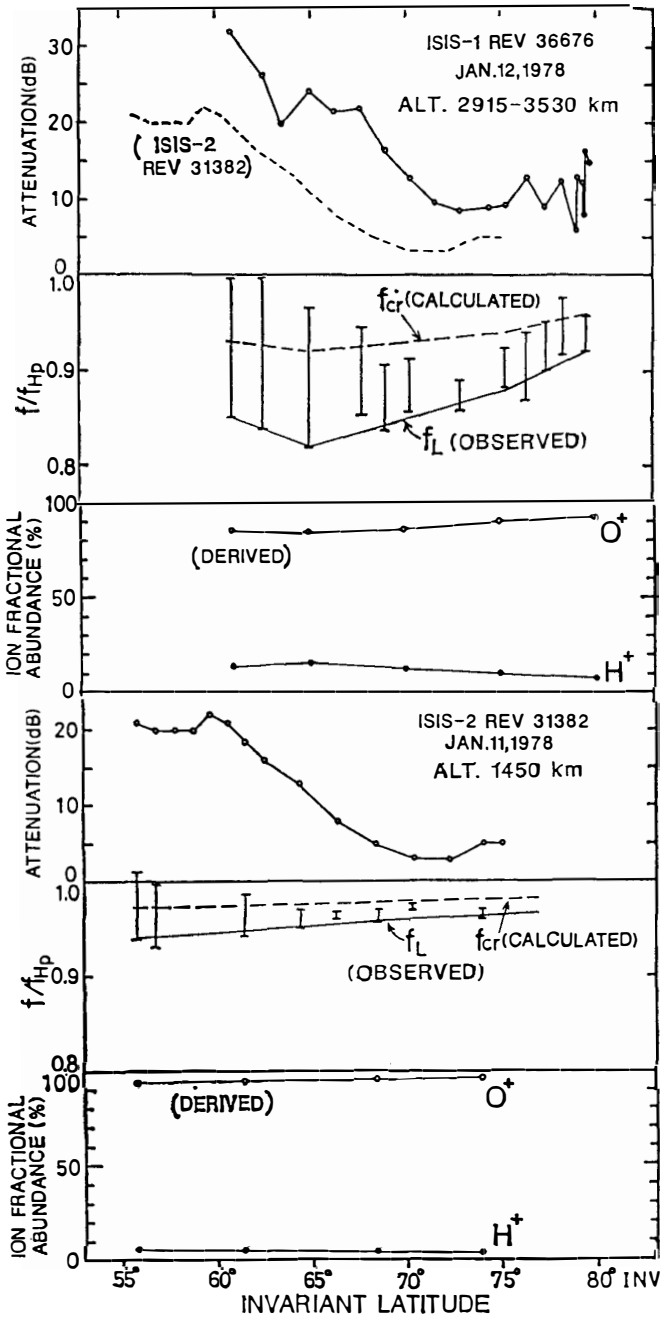

Fig. 42. Latitudinal dependences of the attenuation and the cutoff frequency of multiple ion cutoff observed by ISIS-1 (the top two panels) and ISIS-2 (the fourth and the fifth panels), whose observations were made closely in time (0740–0800 UT on January 12, 1978 for ISIS-1 and 1004–1014 UT on January 11, 1978 for ISIS-2). The ground tracks of the satellites are shown in Fig. 41. Fractional abundances of O^+ and H^+ ion derived from the observed cutoff frequencies are shown in the third and the sixth panels.

Based on the estimated ion composition, f_{cr} can be calculated from the following equation:

$$f_{cr} = f_{Hp} \sqrt{\eta_O + \eta_H / 256}\,. \tag{30}$$

The result is shown by broken lines in the second and fifth panels, and this agrees well with f_{cu} except for those cases with a strong attenuation above 15 dB. This comfirms the relationship between the observed values (f_{cu} and f_{c1}) and the calculated values (f_{cr} and f_L) described in Section 3.3.3.

3.3.6. Discussion

The attenuation at the multi-ion cutoff is explainable by an R to R mode coupling

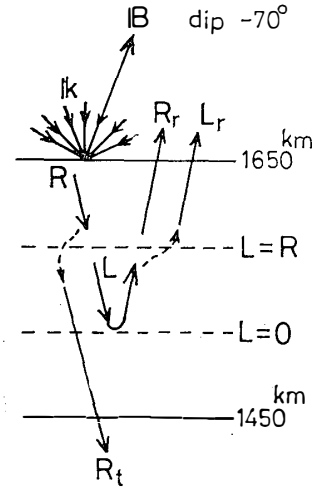

Fig. 43. A model for the calculation of the R to R mode coupling rate with full wave method. Fractional ion abundances are chosen as $H^+ : He^+ : O^+ = 10^3 : 20 : 9 \times 10^3$ (cm^{-3}) at an altitude of 1450 km. The magnetic dip angle is assumed to be $-70°$, and the wave frequency 400 Hz. The ionosphere is assumed to be horizontally stratified layers, and the top and the bottom layer of the calculation is 1650 km and 1450 km, respectively. R, R_r, L_r, and R_t denote the incident R-mode wave, reflected R and L-mode waves, and the penetrated R-mode wave, respectively.

rate in the region which includes the crossover and $L=0$ altitudes, and the mode coupling rate can be calculated by the full wave method. Figure 43 illustrates a case used in the calculation. Fractional ion abundances are chosen as $H^+ : He^+ : O^+ = 10^3 : 20 : 8.98 \times 10^3$ (cm^{-3}) at an altitude of 1450 km, which is a typical value in the summertime polar ionosphere at 65° INV as shown in Fig. 30. The magnetic dip angle is assumed to be 70°. The incident wave frequency is chosen to be 400 Hz. This is a typical cutoff frequency observed by ISIS-2 at 70° INV. The ionosphere is assumed to be horizontally stratified layers. The starting altitude of the calculation is 1650 km, where an angle of incidence is defined. The altitude of the bottom layer in the calculation is 1450 km, which is equal to the altitude of ISIS-2. In the figure, R, R_r, and L_r represents the amplitude of the incident R-mode wave, reflected R and L-mode waves at the altitude of 1650 km, respectively. R_t denotes the amplitude of the penetrated wave at the altitude of 1450 km, which is originated from the input R-mode wave *via* mode coupling, and this forms the residual part in the frequency range less than the cutoff in the power spectrum of ELF hiss. Thus the attenuation at the lower cutoff is given by the ratio of R and R_t. When R is set to be unity, R_r, L_r and R_t give the reflection rate of R and L-mode, and the penetration rate of R-mode, respectively. The attenuation at the cutoff is given as $A = 20 \log_{10} R_t$. These values were calculated for various incident wave normal angles, and they are shown in Fig. 44 as a function of wave incident angle. This result is very similar to the one given by ALTMAN *et al.* (1975), though a different ion composition is used in their calculation. In order to obtain an attenuation of 20 dB, the wave normal at the incident level of 1650 km should lie outside the cone of 39° half angle with respect to $\boldsymbol{B}_0$. In our observation, the case with attenuation over 25 dB is rare. This is due to an initial distribution of the wave normal of ELF hiss. Some of the wave normals always occupy the above-mentioned cone and this increases the penetration rate and prevent the attenuation from increasing higher than 25 dB.

In order to investigate the effect of ion composition on the mode coupling rate, a full wave calculation was made with several models of ion compositions. As previously mentioned in Section 3.3.2, there are two sets of crossover and $L=0$ cutoff frequencies for three ion species of H^+, He^+, and O^+ at ISIS satellite altitude: the one is between

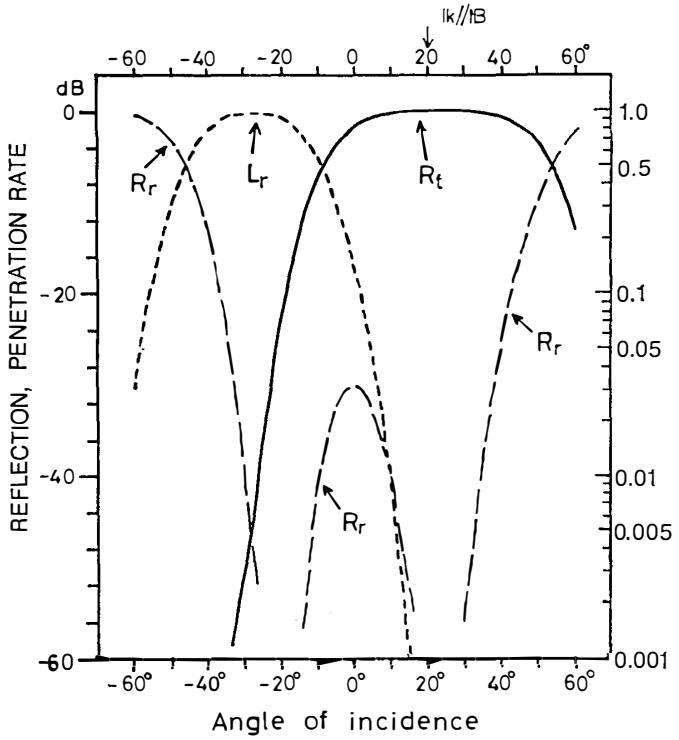

Fig. 44. Incident angle dependences of the reflection rate of R and L-mode waves (R_r and L_r) and the penetration rate of R-mode wave (R_t).

f_{Hp} and $f_H(H_e^+)$, and the other is between $f_H(He^+)$ and $f_H(O^+)$. For simplicity, a full wave calculation is made in an altitude range where only one set of crossover and $L=0$ cutoff frequency is met, so that contribution of each $L=0$ cutoff feature is separately obtained. Here, crossover and $L=0$ cutoff due to H^+ and He^+ are analyzed with five models of ion composition shown in Table 1. In these models, the fractional abundance of O^+ is kept constant, *i.e.* $10^3\,cm^{-3}$, while the ratio of H^+ to He^+ concentration, ρ_i, is varied from 0.01 to 100. These values are defined at the altitude of 1450 km, and the ion composition at other altitude is given by the diffusive equilibrium condition. Figure 45 shows altitude variations of f_{Hp}, $f_H(He^+)$, f_{cr} and f_L for these models.

In model *A*, Δh (distance between crossover altitude and $L=0$ altitude; see Fig. 33) is a few kilometers, which is shorter than the wave length of ELF waves at this altitude by one order of magnitude. This suggests the increase of the R to R mode coupling rate. A similar condition is satisfied in model *E* in the altitude greater than 1600 km, where the increase of the mode coupling is also expected.

For these models, the transmission rate of downgoing R-mode waves, R_t, is calculated by the full wave method over the altitude ranges shown by the horizontal bars in Fig. 45 including the f_{cr} and f_L altitudes. In these calculations, the direction of $\boldsymbol{B}_0$ is assumed to be vertical for simplicity. Figure 46 shows R_t *vs.* ψ for five values of ρ_i and wave frequency f (Fig. 46a), and R_t *vs.* ρ_i for five values of ψ (Fig. 46b). It is found from Fig. 46a that the attenuation is mainly dependent on ψ, and not much dependent on ρ_i, nor f as long as the attenuation is within 20 dB and ρ_i is not extremely

Table 1. Five models of ion composition for the full wave calculation of Figs. 35 and 36.

Altitude : 1450 km

Model	Fractional abundance			Composition		
	H^+	He^+	O^+	H^+	He^+	O^+
A	10^2 cm^{-3}	10^4 cm^{-3}	10^3 cm^{-3}	0.9%	90.1%	9.0%
B	10^3	9×10^3	10^3	9.1	81.1	9.1
C	5×10^3	9×10^3	10^3	45.5	45.5	9.1
D	9×10^3	10^3	10^3	81.8	9.1	9.1
E	10^4	10^3	10^3	90.1	0.9	9.0

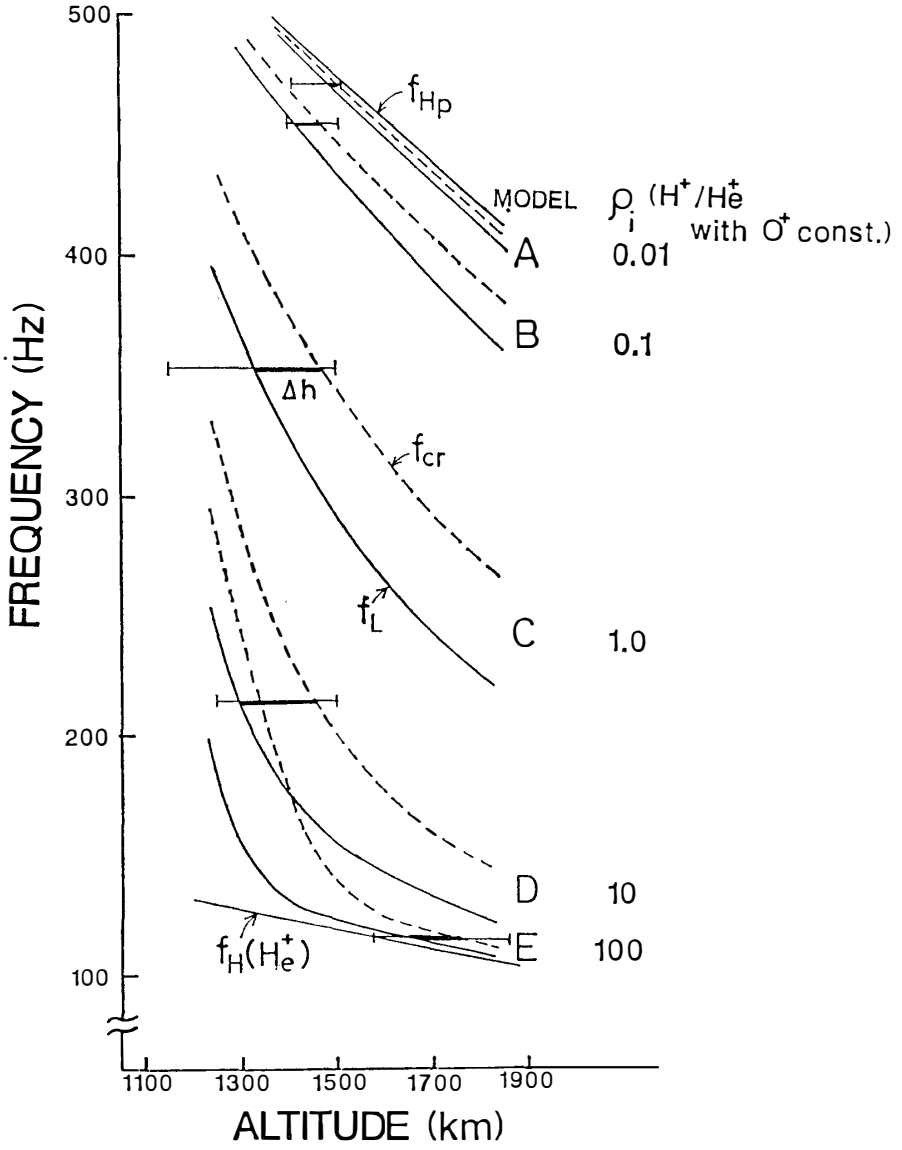

Fig. 45. Altitude variations of f_{Hp}, $f_H(He^+)$, f_{cr} and f_L for the ion composition models A–E shown in Table 1. A thin horizontal bar shows the altitude range for the full wave calculation, and a thick horizontal bar shows the distance Δh between the crossover and the $L=0$ altitude.

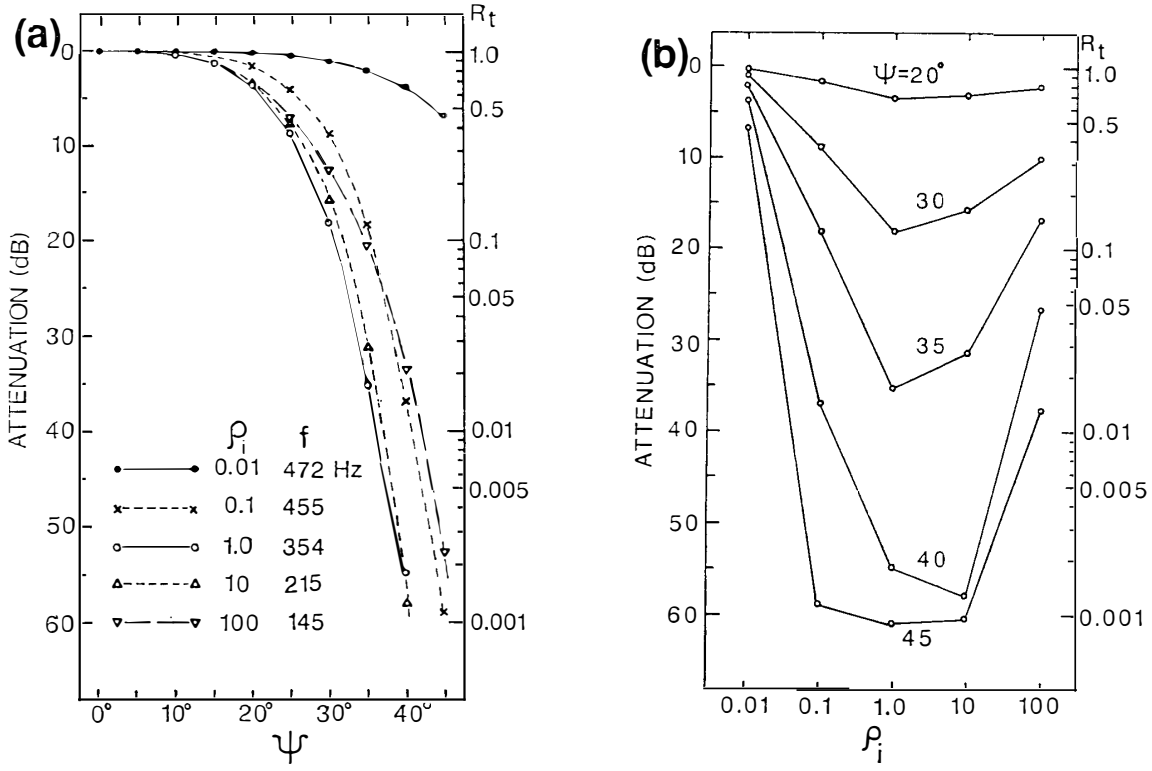

Fig. 46. (a) A plot of the attenuation at $L=0$ cutoff (, or the penetration rate, R_t) vs. ψ for five values of ion concentration ratio of H^+ to He^+, ρ_1. The direction of $\boldsymbol{B}_0$ is assumed to be vertical. (b) A plot of the attenuation rate (, or R_t) vs. ρ_i for five values of ψ.

small.

In Fig. 46b, the attenuation for $\psi=20°$ is almost constant of 4 dB except for $\rho_i=0.01$. If the penetration cone is defined as the attenuation within 4 dB, the width of the cone is not much dependent on the ion composition except for the case of very small ρ_i. For $\rho_i=0.01$, the width of the cone is increased as much as 40°. This seems to be closely related to the fact that Δh is much smaller than the wave length at this altitude. For $\psi=30°$, the attenuation is sensitive to ρ_i in a manner that it becomes maximum near $\rho_i=1.0$ and becomes smaller for either very large or very small value of ρ_i. Similar dependence on ρ_i is found for Δh, as shown in Fig. 45. So, Δh has a strong positive correlation with the attenuation.

A similar full wave calculation is made with different ion composition models in which the ratio of H^+ to O^+ concentration is varied with the fractional abundance of He^+ kept constant, and the result is shown in Appendix 2. It is found from these calculations that $L=0$ cutoff characteristics mainly depend on as long as the ion concentration ratio ρ_i is within moderate value of 0.1 to 10 and the attenuation is within realistic observational value of ~20 dB. This means that if the attenuation at the cutoff shows considerable difference at different altitudes, the difference is rather attributable to altitudinal change in ψ (expected from Snell's law), than to altitudinal change in ρ_i expected from diffusive equilibrium condition. This is an important fact in the comparison of $L=0$ cutoff features observed by ISIS-1 and ISIS-2 satellites.

In the summertime polar ionosphere at the altitude of 1400 km, the fractional

abundance of O^+ ion is much greater than that of H^+ or He^+ ion by more than one order of magnitude and it gradually increases at higher latitudes as shown in Fig. 30. Therefore Δh at higher latitudes must be very small. In fact, ISIS-2 observation in summertime (Fig. 34) shows that Δf, which is equivalent to Δh (see Fig. 33), is very small above 65° INV. These results suggest that the topside ionosphere in high latitudes with a high O^+ concentration has a small Δh value, which is less than the wave length of ELF wave, and this in turn enlarges the width of the penetration cone and causes the decrease or disappearance of the attenuation at the lower cutoff, as in the case of $\rho_i=0.01$ in Figs. 45 and 46.

In the wintertime polar ionosphere, there is a latitudinal transition of the dominant ion from O^+ to H^+, as shown in Fig. 30. In the region where H^+ dominates in the ion composition, the altitude variation of f_{cr} and f_L is similar to that of model E ($\rho_i=100$) shown in Fig. 45. In this case, the attenuation at the cutoff is expected to be greatly reduced as shown in Fig. 46, where the attenuation is reduced for large ρ_i value, and a considerable part of the wave energy can pass through the $L=0$ altitude in R-mode and continues to propagate downward. Figure 47 illustrates this case. These waves again undergo polarization reversal at the second crossover altitude of the f_{cr2} curve, and they are reflected at the second $L=0$ altitude given by the f_{L2} curve. Thus, the lower cutoff below $f_H(He^+)$ is newly formed. ELF observation by ISIS-2 in winter shown in Fig. 35 shows this case.

The ray tracing of ELF waves starting from the geomagnetic equator, described in the preceding chapter, tells that only those waves with initial wave normals lying within a certain window can escape from the LHR reflection and are accessible to the polar ionosphere. Their wave normals tend to direct away from the earth, or poleward,

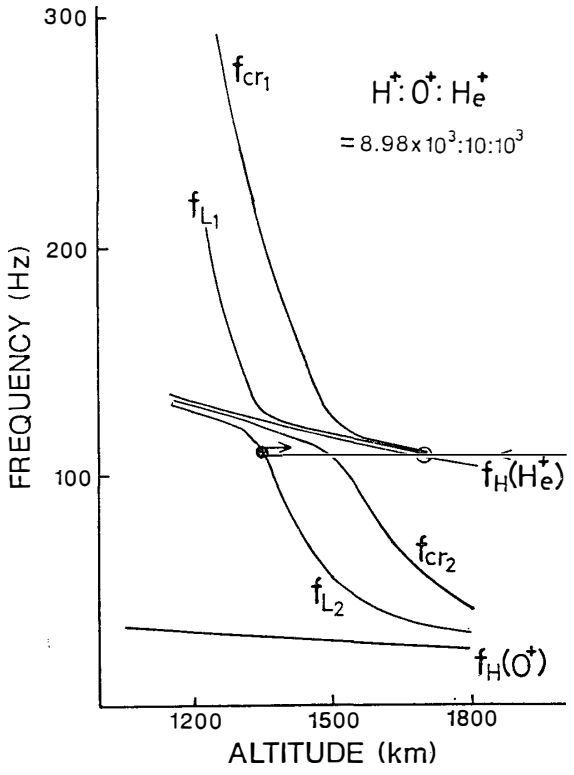

Fig. 47. Altitude variations of $f_H(He^+)$, $f_H(O^+)$, f_{cr1}, f_{L1}, f_{cr2} and f_{L2} for ion composition model E. Transition of the cutoff from a point on the f_{L1} curve (open circle) to another point on the f_{L2} curve (solid circle) is illustrated.

at higher altitudes where the curvature of the field line and the altitude dependence of the refractive index curve work to push the wave normal outward. However at lower altitudes where the vertical electron density gradient is steep, the wave normal is pull back to the vertical. The boundary between these two regions is usually formed at an altitude of 3000 km, where most wave normals become perpendicular to the earth's magnetic field $\boldsymbol{B}_0$. The orbit of ISIS-1 satellite passes through this altitude. So, the wave normal angle of ELF hiss observed by this satellite is expected to be nearly perpendicular to $\boldsymbol{B}_0$. On the other hand, ISIS-2 passes through the region where the wave normal is becoming nearer to the vertical. Therefore, the wave normal angle at the altitude of ISIS-2 is considerably smaller than that observed by ISIS-1. In Fig. 45, the attenuation of the cutoff observed by ISIS-1 is stronger than the one observed by ISIS-2 by 4–12 dB. It is true that $L=0$ cutoff frequency at ISIS-1 altitude ($\sim$250 Hz) is different from that at ISIS-2 altitude ($\sim$400 Hz). However, the attenuation at $L=0$ cutoff is not much dependent on the wave frequency, but mainly dependent on ψ as discussed before. Therefore, the above difference in the attenuation is considered to be due to the change of wave normal angle between ISIS-1 and ISIS-2 altitudes. The incident angle dependence of the attenuation shown in Fig. 44 tells that the wave normal angle at the altitude of ISIS-1 should be larger than the one at the altitude of ISIS-2, and this is consistent with the results from the ray tracing described above.

3.4. Seasonal variation of ELF/VLF emissions observed by ISIS satellites and on the ground

3.4.1. Introduction

Natural ELF emissions known as polar chorus and ELF hiss are the most common and the most intense emissions observed at high latitudes (*e.g.*, UNGSTRUP and JACKEROTT, 1963; EGELAND *et al.*, 1965). From the ground-based measurement, it was found that both types of emission are observed during local geomagnetic daytime, and have a seasonal variation such that peak intensities are detected in the local summer (HELLIWELL, 1965; ITO *et al.*, 1986). SUZUKI and SATO (1987) analyzed 750 Hz band ELF emission data observed at the geomagnetically conjugate pair stations of Syowa Station, Antarctica and Husafell in Iceland, and found north-south hemispheric asymmetry of the emission intensity. They found that the emission intensity is stronger in the summer hemisphere, and the summer-winter intensity ratio is about 6 dB. As these emissions are considered to be generated in the geomagnetic equatorial plane, it is difficult to attribute this asymmetry to a source mechanism. The seasonal change of the propagation media is notable at the polar ionosphere, where the electron density in the sunlit hemisphere is greater than that in the dark hemisphere by more than an order of magnitude. NAGANO (1980) calculated the seasonal variation in the ionospheric absorption of ELF/VLF waves with a full-wave method, and showed that the absorption in summertime is stronger than that in wintertime by 2.5 dB in ELF range due to the increased electron-neutral collision rate caused by the increased neutral gas pressure in the D region of the summer ionosphere. This feature is opposite to the observed seasonal variation of the emission intensity. So, the observed asymmetry must be attributed to the propagation above the ionosphere. In fact, ELF emissions

observed above the ionosphere by polar orbiting satellites (KELLEY *et al.*, 1975) showed summer-winter asymmetry of the emission intensity similar to that observed by the ground-based observation. They found that the averaged emission intensity in the summer hemisphere is about 3 times (4.8 dB) stronger than that in the winter hemisphere. They explained this with an asymmetric leakage of plasmaspheric hiss from the low altitude boundary of plasmasphere. That is, the boundary is not well definable in summertime due to an enhanced electron density in the trough region of the ionosphere, and the plasmaspheric hiss can efficiently cross the boundary and be refracted downward into the high-latitude ionosphere.

We try here to study the seasonal variation of the ELF hiss intensity above and below the polar ionosphere in statistical basis. We dealt with the ELF/VLF observation data for 234 passes of ISIS-1 and 2 satellites over Syowa Station from January 1976 to December 1979. Besides, ELF/VLF data observed on the ground at Syowa Station in 1978 are used for comparison with the satellite data. A discussion was made on a possible effect on ELF wave propagation from a north-south asymmetry of electron density profile in the ionosphere, and it is shown that the seasonal variation is attributable to this asymmetric propagation.

3.4.2. ISIS VLF observation

ISIS satellite is transmitting an AGC (automatic gain control) signal of the VLF receiver *via* PCM channel and wide-band VLF data *via* FM channel. The AGC signal gives the total emission intensity observed in the frequency band of 50 Hz–25 kHz, which is much wider than a typical frequency bandwidth of ELF emissions of 500 Hz–2 kHz. However, in the dayside polar ionosphere, only ELF hiss and chorus are usually observed in the above-mentioned frequency band, except for the cusp region in wintertime where impulsive auroral hiss of much wider frequency bandwidth is often observed (YOSHINO *et al.*, 1981). Hence, the AGC signal intensity can be regarded as the ELF wave intensity in the dayside polar ionosphere except for the cusp region. The local time and latitudinal dependences of this signal are analyzed as follows.

The AGC signal along a satellite orbit is given in MLT-INV coordinate. For a proper normalization of the data, MLT and INV were divided into bins of 2 hours by 5 degrees, and the AGC signal is averaged in each MLT-INV bin for summer and winter seasons. The distribution of the number of orbits in these bins are shown in Fig. 48 for summer (upper panel) and for the rest of year (lower panel). Taking account of input-output characteristics of the VLF receiver and signal loss due to a sheath impedance of the antenna, the AGC signal level can be converted into wave electric field strength E (Appendix 3). In the comparison of wave intensity, a judgement with E leads to a misunderstanding because E changes according to $1/\sqrt[4]{N_e}$ and N_e shows a marked seasonal variation at the satellite altitude. In order to exclude this effect, the power flux P must be used for comparison. P is the product of E and B, the wave magnetic field strength. However, B was unavailable in ISIS VLF experiment. Therefore, by assuming an appropriate value of the refractive index n, P is obtained from E by the following relation

$$P(\mathrm{W/m^2}) = \frac{\{E(\mathrm{V/m})\}^2}{120\pi n}. \tag{31}$$

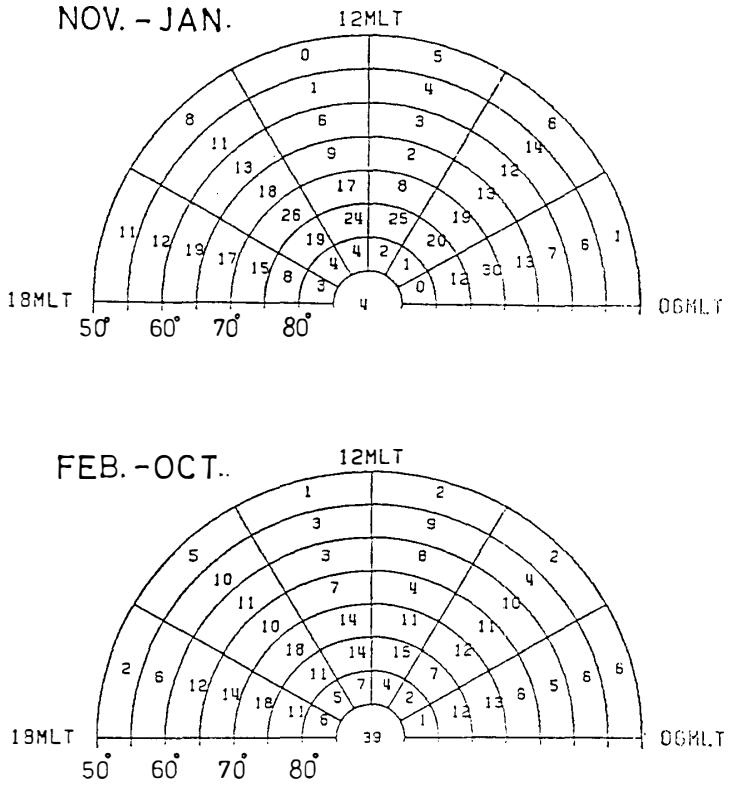

Fig. 48. Numbers of ISIS satellite orbits in each MLT-INV bin of 2 hours by 5 degrees for summer months (November–January, upper panel) and the rest of the year (lower panel).

In ELF range, the condition for *QL* (quasi longitudinal) approximation

$$\frac{4f_p^2}{f^2 f_H^2} \gg \frac{\sin^4\psi}{\cos^2\psi}, \tag{32}$$

is satisfied for a wide range of ψ, so that n under *QL* approximation is given by

$$n = 9\times 10^3 \sqrt{N_e} \,/\, \sqrt{f(f_H \cos\psi - f)} \,. \tag{33}$$

In the polar region at the altitude of ISIS satellites, f_H is 790–900 kHz for ISIS-2 and 370–450 kHz for ISIS-1. For f and ψ, 1 kHz and 45° are assumed as the typical values. During ISIS VLF experiment, the data on N_e was not available. However, by means of a worldwide map of electron and ion densities in the altitude range of 972–1220 km obtained by ISS-b satellite (RADIO RESEARCH LABORATORIES, 1981) and the scale height of electrons obtained from ISIS-2 topside sounder ionogram (MATUURA, 1979), the latitudinal and local time distributions of N_e at the altitude of ISIS satellites are obtained. Table 2 shows the distribution of N_e in each MLT-INV bin of 2 hours by 5 degrees at the altitude of ISIS-2 satellite for summer and winter. By substituting these values of N_e into eqs. (33) and (31), the electric field measured by ISIS was converted to P, and the averaged values of P for one spin period (19 s for ISIS-2 and 23 s for ISIS-1) become the data base for the following analysis.

The power spectra of ELF hiss observed by polar orbiting satellites often show a

Table 2. Models of the electron density (in $10^3/cm^3$) distribution in each MLT-INV block of 2 hours by 5 degrees at the altitude of ISIS-2 satellite for summer (upper table) and winter (lower table).

Summer

Latitude (deg.)	Local time					
	06–08	08–10	10–12	12–14	14–16	16–18
50–55	19	18	15	11	8.2	6.6
55–60	18	19	17	13	8.0	4.7
60–65	18	20	19	15	8.1	3.8
65–70	18	21	21	17	8.9	3.5
70–75	19	22	23	19	11	3.6
75–80	19	23	25	21	14	4.1
80–85	20	24	26	23	20	5.0

Winter

Latitude (deg.)	Local time					
	06–08	08–10	10–12	12–14	14–16	16–18
50–55	1.8	3.4	5.4	7.0	6.6	3.9
55–60	2.3	4.1	6.2	7.4	6.5	3.8
60–65	2.7	4.9	7.1	7.8	6.3	3.4
65–70	3.3	5.8	8.0	8.2	5.8	2.7
70–75	3.9	6.9	8.8	8.4	5.0	1.7
75–80	4.5	7.7	9.4	8.6	4.1	0.8
80–85	4.8	8.4	10	8.7	3.2	0.4

latitudinal dependence of the frequency bandwidth such that the bandwidth decreases in higher latitude. Figure 49 shows a series of power spectra of ELF hiss emissions observed by ISIS-2 on September 29, 1977. A logarithmic scale is used in the ordinate. In the figure, the spectra illustrated by broken lines are those observed simultaneously at Syowa Station. The frequency bandwidth of the emissions decreases with increasing latitude. The typical bandwidth of the emission is 2 kHz for latitudes below 60° INV, 1.5 kHz for 60°–65° INV, 1 kHz for 65°–70° INV and 0.6 kHz above 70° INV, respectively. By using these values, the power flux density P' (W/m² Hz) can be estimated from P.

Figure 50 shows latitudinal dependence of P and P' for summer (solid line) and winter (broken line) in the local time range of 08–12 MLT, when the intensity showed a daily maximum. Here, the definition of summer or winter is the period of solstitial 2 months, *i.e.*, June–July and December–January. The number of data points in each latitudinal division of 5 degrees is shown at the top of the figure for the both seasons. In Fig. 50a, P decreases with increasing latitude for the both seasons. This is possibly due to the decreasing bandwidth of the emission in higher latitude shown in Fig. 49, because P' shown in Fig. 50b has much smaller latitudinal dependence within 2 dB in the latitude range of 60°–80° INV. At around 80° INV, there is a strong decrease in the emission intensity as much as 10 dB. This corresponds to the high latitude boundary of ELF hiss reported by KELLEY *et al.* (1975). Figure 50c shows summer–winter ratio of P' in dB scale. In the latitude range of 60°–80° INV, the intensity in winter is lower by 3–5 dB as compared with that in summer. This summer–winter ratio is

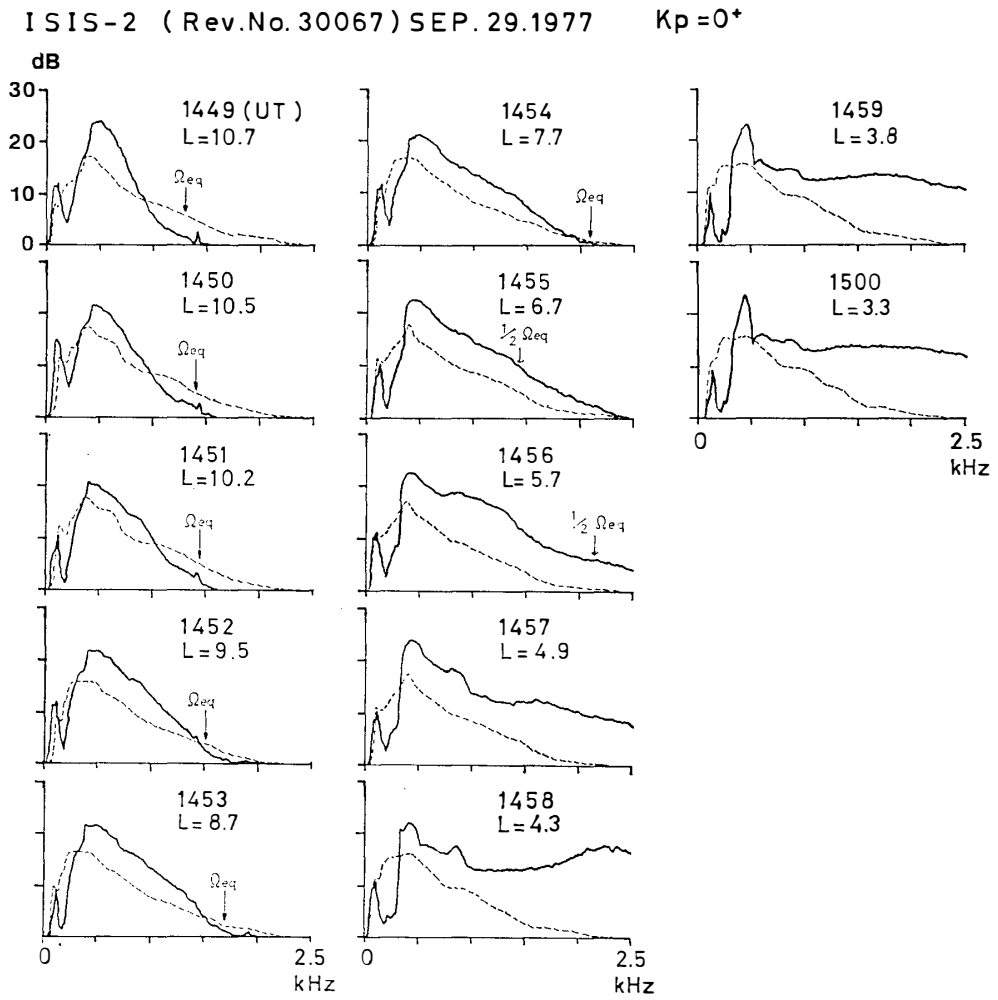

Fig. 49. Power spectra of ELF hiss along ISIS-2 satellite orbit observed on September 29, 1977. In each panel, Ω_{eq} denotes electron gyro frequency at the magnetic equatorial plane for the L-value of the satellite. The spectra illustrated by broken lines are those observed at Syowa Station, simultaneously.

almost equal to the summer–winter ratio obtained by Ogo 6 and OV1-17 satellites (KELLEY *et al.*, 1975). In the latitude range of 55°–60°, which is expected to be inside the plasmapause in a quiet or moderate condition of geomagnetic activity, the wintertime intensity is almost equal to the summertime one. Hence, the summer–winter asymmetry of the ELF hiss intensity seems to be restricted to the region outside the plasmapause in an altitude range of 1450–3500 km. Similar latitudinal characteristics are found in the ground-based observation and will be discussed in Section 3.4.4.

Figure 51a shows the local time variation of P' in a latitudinal range of 60°–70° INV for summer (solid line) and winter (broken line), whereas Fig. 51b shows the local time variation in the summer–winter ratio of P'. It is clear that the intensity was strongest in the morning hours of 08–10 MLT for the both seasons, and it decreased with local time in the afternoon hours. This local time variation is similar to that of ELF hiss intensity in the equatorial plane outside the plasmasphere (TSURUTANI and SMITH, 1977), which suggests that ELF hiss observed by ISIS was directly propagated from the equatorial plane and not much affected by the plasmaspheric hiss

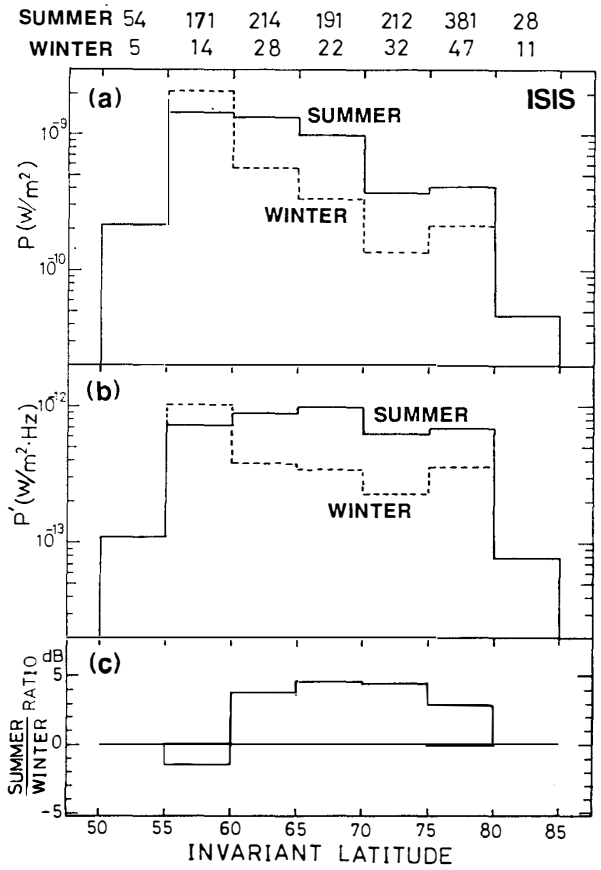

Fig. 50. (a) Latitudinal dependence of the power flux P (W/m²) of ELF waves observed by ISIS in the local time range of 08–12 MLT for summer (solid line) and winter (broken line). (b) The power flux density P′ (W/m²·Hz). (c) Latitudinal dependence of the summer–winter ratio of P′. The number of data points in each latitudinal division of 5 degrees is shown at the top of the figure for both seasons.

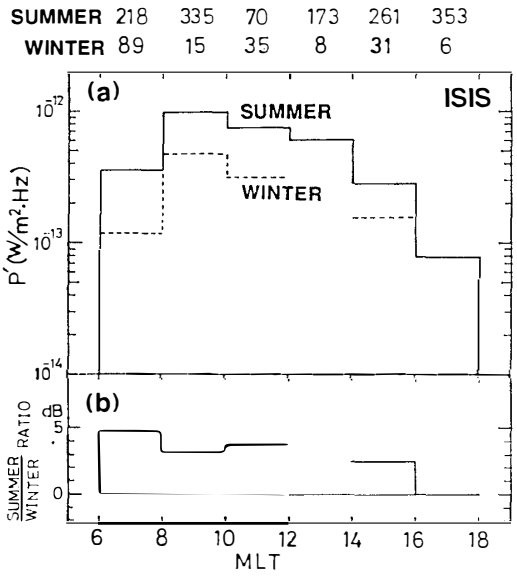

Fig. 51. (a) Local time variation of P′ of ELF waves observed by ISIS in the latitude range of 60°–70° INV for summer (solid line) and winter (broken line). (b) Local time variation in the summer–winter ratio of P′. The number of data points in each local time division of 2 hours is shown at the top of the figure for the both seasons.

which could be leaked out from the lower boundary of the plasmasphere.

3.4.3. Ground-based ELF/VLF observation at Syowa Station

At Syowa Station, the magnetic component of ELF/VLF emissions has been observed by an air-core loop antenna. During 1978, the intensity in frequency bands of 750 Hz, 1.0, 2.0, 8.0 and 20 kHz were continuously registered on a pen recorder. In the present study, 750 Hz band was analyzed as a representative frequency of ELF hiss. The recorded intensity was sliced into 5 levels every 10 min according to the levels shown in Table 3, and they become the data base for the present data analysis. The representative values shown in the table were used in obtaining the emission intensity.

Figure 52 shows the local time variation in the averaged emission intensity for summer months (November and December) and winter months (May–August) in 1978 in the same format as Fig. 51. These months were chosen to suit with the definition of summer and winter used in the analysis of ISIS VLF data, though the ground-based

Table 3. Slice levels for the 750 Hz band ELF wave intensity observed at Syowa Station, and the representative values corresponding to signal levels of 0 to 4.

Level	Intensity range ($W/m^2 \cdot Hz$)	Representative value ($W/m^2 \cdot Hz$)
0	1×10^{-15}	5×10^{-16}
1	$1 \times 10^{-15} - 2 \times 10^{-15}$	1.5×10^{-15}
2	$2 \times 10^{-15} - 5 \times 10^{-15}$	3.5×10^{-15}
3	$5 \times 10^{-15} - 1 \times 10^{-14}$	7.5×10^{-15}
4	1×10^{-14}	2×10^{-14}

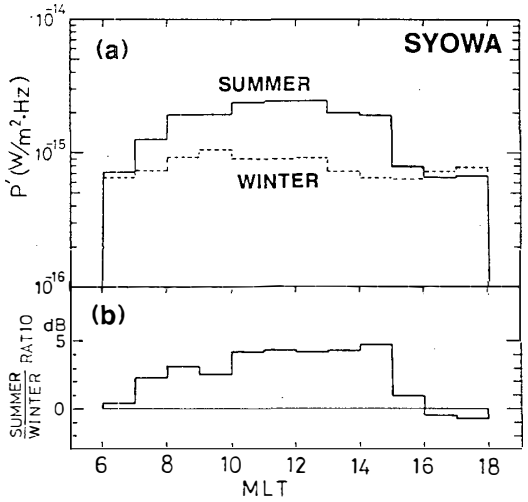

Fig. 52. (a) Local time variation in the power flux density P' ($W/m^2 \cdot Hz$) of ELF waves observed at Syowa Station for summer months (November and December, 1976–1979, illustrated by solid line) and winter months (May–August, 1976–1979 illustrated by broken line). (b) Local time variation in the summer–winter ratio of P'.

data in January and February were missing. The local time variation in summer shows a peak intensity just after 12 MLT (15 LT). This is different from the local time variation observed at a satellite altitude, where the peak intensity appears in 08–10 MLT. This discrepancy is ought to be attributed to the propagation from the satellite altitude to the ionosphere, especially due to the transmission rate in the sunlit ionosphere because ground-based observation of ELF emission at Syowa and Iceland conjugate pair stations showed that a peak intensity appeared near the local noon at each station (SUZUKI and SATO, 1987). The local time variation in winter is within 2 dB, which is smaller than that in summer by 4 dB. The peak intensity in winter takes place in 09–10 MLT, similarly to the satellite observation.

The intensity ratio between the two seasons shown in Fig. 52b gradually increases with local time from 2.3 dB at 07 MLT to 4.7 dB at 15 MLT. SUZUKI and SATO (1987) reported a greater intensity ratio of 6 dB in 10–14 MLT in the year of 1984. The above difference can be attributed to the different epoch of the observation. The summer–winter intensity ratio observed on the ground is almost the same as that at the satellite altitude shown in Fig. 51. This will indicate that the observed seasonal variation is mainly due to a modification of ELF waves during their propagation from the source region to the satellite altitude of 1450–3500 km, because the propagation below the satellite altitude causes only a small effect on the seasonal variation. At 16–18 MLT,

the emission intensity in winter exceeds the one in summer. This is possibly due to a contamination by auroral hiss, which is active in the evening in winter. Similar local time dependence is found in the satellite data shown in Fig. 51, though with less reliability due to a small number of data points.

3.4.4. Discussion

Below the satellite altitude there will be several mechanisms which can contribute to a seasonal variation in the transmission rate of ELF waves in the *D*-region ionosphere. One of the possible causes is a seasonal variation in electron-neutral collision rate caused by a change of neutral gas pressure with season (NAGANO *et al.*, 1980). This brings about a greater ionospheric absorption of ELF waves by 2.5 dB in summer than in winter. Another possible mechanism is the ionospheric absorption of ELF waves at the time of high energy particle precipitation, which can be inferred from an increase in CNA (cosmic noise absorption) of HF waves. As CNA shows a seasonal variation such that it increases in winter in auroral zone (*e.g.*, BASLER, 1963; HARGREAVES and COWLEY, 1967), the absorption of ELF waves at the time of particle precipitation is expected to be large in winter. However, a comparison of the seasonal variations in the ELF wave intensity observed at the satellite altitude and on the ground, schematically illustrated in Fig. 53, indicates that the seasonal variation observed on the ground is also seen at the satellite altitude. This means that the cause of the seasonal variation must be located mainly above the satellite altitude, and the polar ionosphere gives only a small effect on the seasonal variation of ELF hiss intensity. This is partly due to the fact that the above two processes cause opposite effects on the seasonal variation, and they may cancel each other. It is difficult to separate the effects from these different processes quantitatively with our data alone.

KELLEY *et al.* (1975) explained the seasonal variation of ELF hiss intensity at the

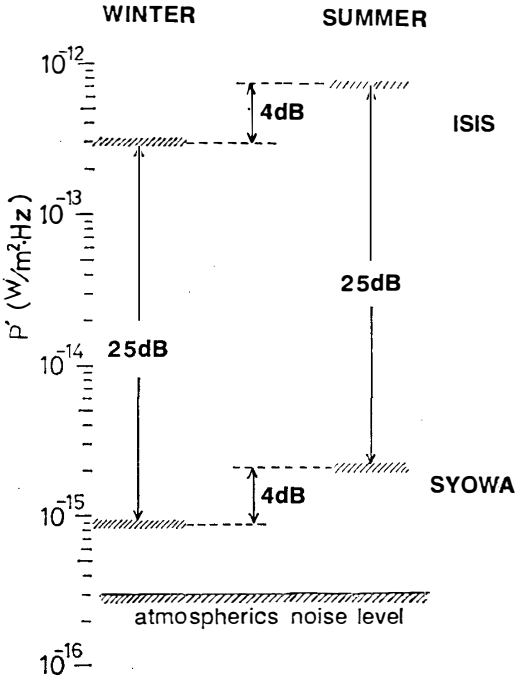

Fig. 53. Schematic illustration of the averaged power flux density of ELF waves observed by ISIS satellites and on the ground for summer and winter seasons.

satellite altitude by a leakage of plasmaspheric hiss from the lower boundary of the plasmapause in summer. If this process is working, ELF hiss observed in high latitudes should show a constant frequency band peculiar to plasmaspheric hiss. However, the power spectra of ELF hiss observed by ISIS illustrated in Fig. 49 show a systematic decrease in bandwidth with increasing latitude. This is similar to the L-value dependence of the emission frequency in the equatorial plane outside the plasmapause (TSURUTANI and SMITH, 1977). Hence, the ELF hiss observed by ISIS could be thought to propagate from the equatorial plane and not much affected by the leaked plasmaspheric hiss. Therefore, the seasonal intensity variation is ought to be attributed to the propagation from the equatorial plane to the satellite altitude in asymmetric electron density profiles in the summer and winter hemispheres.

As discussed in Section 2.5, the time derivative of wave normal angle, $\partial\psi/\partial t$, is controlled by four factors: (1) latitudinal electron density gradient, (2) vertical electron density gradient, (3) height gradient in electron density, and (4) altitude variation of the geomagnetic field. The factors (1) and (2) work to turn the wave normal towards the earth, whereas (3) and (4) away from the earth. In the altitude above 3000 km, the effects of (3) and (4) are greater than that of (1) and (2), which causes an increase in ψ with decreasing altitude with a slope $\partial\psi/\partial h$, where h denotes altitude, as shown in Fig. 4b. When the electron density gradient along a ray path increases, the slope is expected to decrease. As the ψ_i-window is formed by those curves of wave normal angle, a larger window width is expected for smaller values of $\partial\psi/\partial h$ attained in the summer hemisphere where the electron density gradient increases along a ray path.

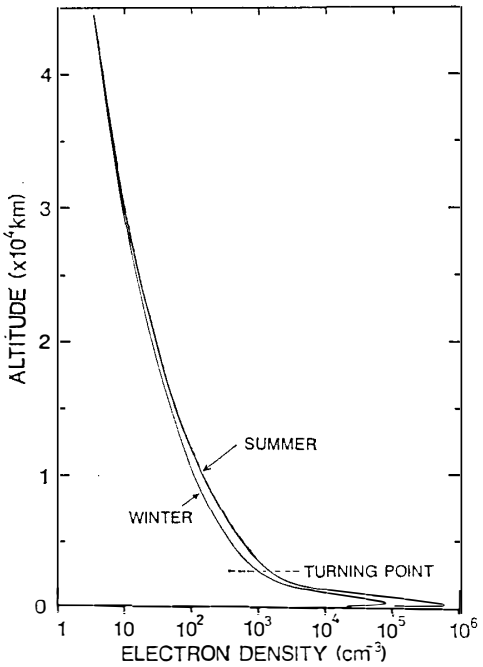

Fig. 54. Electron density profiles for the summer and winter seasons used in the calculation of ψ_i-window.

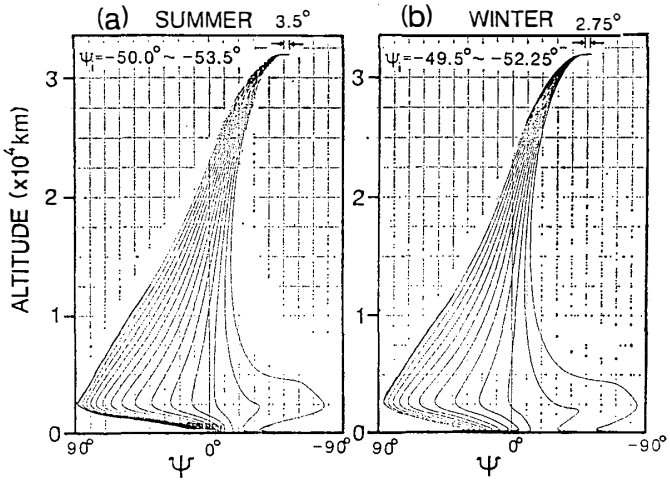

Fig. 55. (a) shows the curves of wave normal angle of the penetrating ray paths of 1.5 kHz waves for summer, and (b) shows those for winter. It is found that the ψ_i-window is 3.5° for summer and 2.75° for winter.

In order to confirm this expectation, ψ_i-window is calculated for two electron density profiles shown in Fig. 54 for the summer and winter hemispheres. Figure 55a shows the curves of wave normal angle of the penetrating ray paths of 1.5 kHz waves for summer, and Fig. 55b shows the curves for winter. It is found that the ψ_i-window is 3.5° for summer and 2.75° for winter. This suggests that more wave energy is transferred from the equatorial plane to the satellite altitude in the summer hemisphere, and the wave intensity at the satellite altitude is expected to increase in summer. As this seasonal effect is caused by a change in the width of ψ_i-window, the effect is valid only in the altitude below the turning point of wave normal angle at 3000 km, where the existence of waves is limited only to "penetrating ray path", which starts from the equator with an initial wave normal angle within the ψ_i-window. No seasonal dependence is expected above the turning point, where dominant waves are of "non-penetrating ray paths" starting with an initial wave normal angle outside the ψ_i-window.

KELLEY *et al.* (1975) found "poleward skewing" of the wave intensity, that is, a peak wave intensity occurred in higher latitudes when observed at a lower altitude. They explained this trend by a propagation of plasmaspheric hiss from the plasmasphere to the high-latitude ionosphere. However, the ray tracing from the equatorial plane to the polar ionosphere in Section 2.4 shows that a poleward skewing is a general feature of the penetrating ray paths as shown in the right panel of Fig. 6. Hence, the poleward skewing of ELF wave intensity would not be regarded as the evidence for leaked plasmaspheric hiss.

Ground-based ELF/VLF wave observations in the auroral zone showed a seasonal variation such that the intensity in summer was stronger than that in winter by 4–6 dB (HELLIWELL, 1965; ITO *et al.*, 1986; SUZUKI and SATO, 1987; Present work). However, the observation at $L=4$ showed an opposite trend, *i.e.* the intensity in 2–4 kHz range was stronger in winter, and this was explained by an increased ionospheric attenuation in summer similar to an increased CNA (cosmic noise absorption) in the same season (ROSENBERG and DUDENEY, 1986). ELF/VLF observations at the altitude of ISIS satellites in Section 3.4.2 showed a similar latitudinal dependence of the seasonal variation: strong intensity in summer in latitudes higher than 60° INV, while strong intensity in winter in the range of 55°–60° INV ($L=3$–4). This means that the seasonal variation of ELF wave intensity observed at $L=4$ on the ground cannot be fully attributed to the ionospheric effect. The propagation above the satellite altitude is also effective in producing the observed seasonal variation of ELF intensity.

Finally, the satellite-ground intensity difference of ELF waves illustrated in Fig. 53 is discussed. It was found that the intensity difference is 25 dB for the both seasons. According to NAGANO *et al.* (1980), the ionospheric absorption in quiet geomagnetic activity was estimated to be about 10 dB for ELF waves. The rest of the attenuation of 15 dB can be attributed to the multi-ion cutoff described in Section 3.3 as follows. In this cutoff, the down going wave is strongly attenuated at $L=0$ cutoff frequency. The attenuation usually shows a latitudinal dependence, and it is about 15 dB at $L=6$. The cutoff frequency is a function of altitude: 250–400 Hz at the altitude of ISIS satellites and 800 Hz at the level of the ionosphere at $L=6$. Hence, most of the frequency components of ELF hiss observed at Syowa have been reduced by about 15 dB in the course of propagation from the satellite altitude to the ionosphere.

4. Ducted Propagation Outside the Plasmapause

4.1. Introduction

Chapter 2 dealt with the propagation characteristics of whistler mode ELF waves under uniform electron density distribution by a 2-dimensional ray tracing, and the results of calculations were confirmed by ISIS satellite observation of ELF waves. In the magnetosphere, another type of whistler mode wave propagation is possible when a column of electron density enhancement is formed along the earth's magnetic field line. In this type of propagation, waves propagate in the region of density enhancement with a snakelike path under conditions of $f<0.5f_H$ and $\psi<\cos^{-1}(N_m/N_b)$, where f denotes the wave frequency concerned, f_H the electron gyro-frequency, ψ the wave normal angle with respect to the earth's magnetic field $\boldsymbol{B}_0$, N_m the maximum value of the enhanced electron density, and N_b the background electron density. The above density enhancement along the field line is called field-aligned duct for ELF waves, or simply "ELF duct", and this type of propagation is called "ducted propagation".

The nature of the duct in the plasmasphere was fairly well known from the analysis of whistlers observed on the ground (SMITH, 1961; HELLIWELL, 1965; STUART, 1977) and by satellites (SMITH and ANGERAMI, 1968; ANGERAMI, 1970). The L values of the ducts obtained by the nose frequencies of whistler traces were mostly in the range of 2.6–3.6 (STUART, 1977). The diameter of the duct was estimated to be 400–500 km in the geomagnetic equatorial plane at $L=3$, and the electron density enhancement was estimated to be 10–20% above the background (SMITH and ANGERAMI, 1968; ANGERAMI, 1970).

Outside the plasmapause, the occurrence of whistler is very rare, and this fact causes a difficulty in finding out the evidence of ducted propagation from ground-based observations. However, satellite observations of wave normal angles in the magnetosphere made it possible to distinguish ducted propagation from nonducted one by examining wave normal distribution. BURTON and HOLZER (1974) measured the wave normal distribution of chorus emissions by tri-axial search coil magnetometer on board Ogo 5 satellite. They found two groups of wave normal distribution, which corresponds respectively to ducted and nonducted propagations. In ducted propagation, ψ was confined within a cone whose axis was parallel to $\boldsymbol{B}_0$ and the half angle of 40°, in the observations in low and middle latitudes (magnetic latitude up to 50°). This corresponds to the electron density enhancement of 30% above the background. The absolute value of this enhancement is at most several electrons/cm^3, and this enhancement rate becomes relatively small at a low altitude due to the increase in background

electron density. At a certain altitude around several hundreds to several thousands of km, the enhancement is no longer sufficient to confine the wave and the duct disappears. From the end point of duct, the wave propagates downward in nonducted mode. This type of propagation is called "partly ducted propagation" (CERISIER, 1974; TIXIER and CHARCOSSET, 1978). Periodic emissions, excited at regular intervals of several seconds, are considered to show other evidence of the occurrence of ducted propagation outside the plasmapause. HELLIWELL (1963) observed periodic emissions accompanying whistlers, and he found that the repetition period of periodic emissions was the same as the two-hop group delay of whistlers. Therefore, he suggested that the observed periodic emissions are whistler mode waves triggered near the magnetic equator by whistler mode wave packets echoing between the two hemispheres along the geomagnetic field line. Conjugate observations of periodic emissions revealed that emissions were recorded alternately in opposite hemisphere (LOKKEN *et al.*, 1961; MATSUDO and SATO, 1986). This feature supports the idea of echoing wave packets the two hemispheres. The echoing of wave packets is most efficiently realized along a duct. The repetition period of emissions is attributable to a ducted propagation, in which a wave packet bounces between the two hemispheres with a constant period.

This chapter is devoted to the discussion on the occurrence rate of ducted propagation near $L=6$, as well as spatial extent of periodic emission at the satellite altitude and on the ground, through the analysis of periodic emissions observed at Andøya in Norway, and Syowa Station in Antarctica, and by ISIS satellite over Antarctica. The wideness of the receiving area for ELF emissions is explained in terms of "partly ducted propagation", in which the ray paths diverge during the course of downward propagation from the ELF duct exit to the ionosphere.

4.2. Occurrence characteristics of periodic emissions

In ELF wave propagation outise the plasmapause, the occurrence rate of ducted propagation has not been well known. This is partly due to a small occurrence rate of ELF wave phenomena identified as ducted propagation, such as whistler trains and periodic emissions. In this section, the occurrence rate of periodic emissions is obtained from ELF/VLF data at Andøya (69.2°N, 16.0°E) in northern Norway and at Syowa Station (69.0°S, 39.6°E), Antarctica in the period of March 1–26, 1982. This gives an estimation on the occurrence of ducted propagation outside the plasmapause.

Figure 56 shows the location of Andøya and the geomagnetic conjugate point of Syowa Station, which are located at the same geomagnetic latitude but separated by 1600 km longitudinally. At both stations, ELF/VLF signals in the frequency range of 50 Hz–10 kHz were recorded continuously on audio tapes. From these data, the intensity at the frequency bands of 750 Hz and 1.25 kHz were picked up and digitized with sampling rate of 12 Hz. Figure 57 shows an example of periodic emission observed at the both stations on March 14, 1982 in the time interval of 0910:50–0911:10 UT. The upper panel of Fig. 57 shows the intensities of 1.25 kHz band emissions at the both stations, whereas the lower panel shows the cross correlation function between them. It is evident that the intensity rises alternately in the opposite hemisphere. In order to find out the periodicity in the emission, the intensities of 1.25 kHz band emissions observed at the both stations were analyzed by FFT (Fast Fourier Trans-

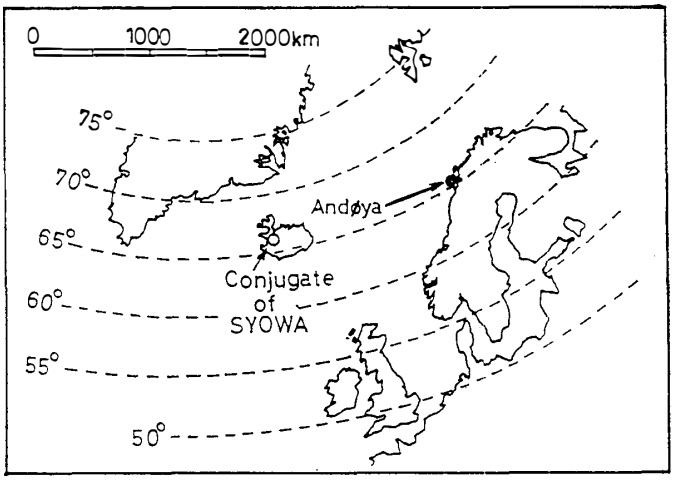

Fig. 56. Location of Andøya in northern Norway and the geomagnetic conjugate point of Syowa Station, Antarctica. Broken lines indicate geomagnetic latitude.

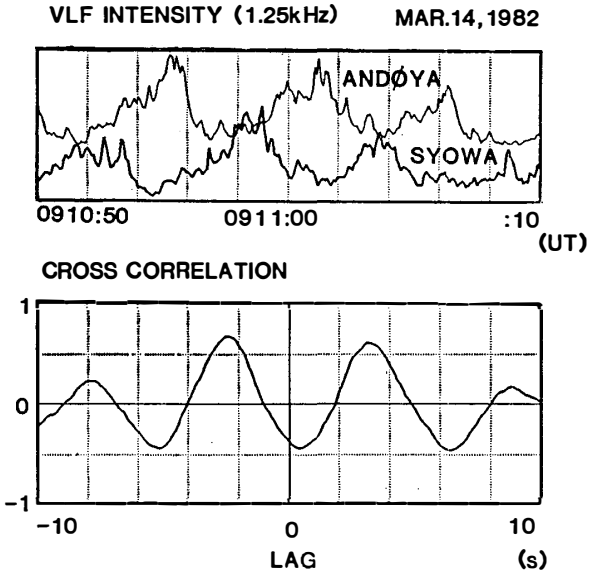

Fig. 57. Intensity records of 1.25 kHz band periodic emission observed at Andøya and Syowa on March 14, 1982 in the time interval of 0910:50–0911:10 UT (upper panel). A cross correlation function between these intensity values is also shown (lower panel).

form) and the results were displayed as frequency-time spectrograms. Figure 58 shows an example of the frequency-time spectrogram for the event observed at the time interval of 1200–1400 UT on March 10, 1982. Figures 58a and 58b show the power spectra for Andøya and Syowa, respectively, and Fig. 58c shows the phase spectra between them. In gray scale display of Fig. 58c, a dark color represents out of phase (180°) relation. A noticeable band at 0.2 Hz in each panel indicates the occurrence of periodic emissions. Phase spectra are sometimes useful in identifying periodic emissions when their occurrence is intermittent and the power spectra do not show noticeable peaks. By means of the data during March 1–26, 1982, periodic emissions identified from the frequency-time spectrograms are summarized in Table 4. In the

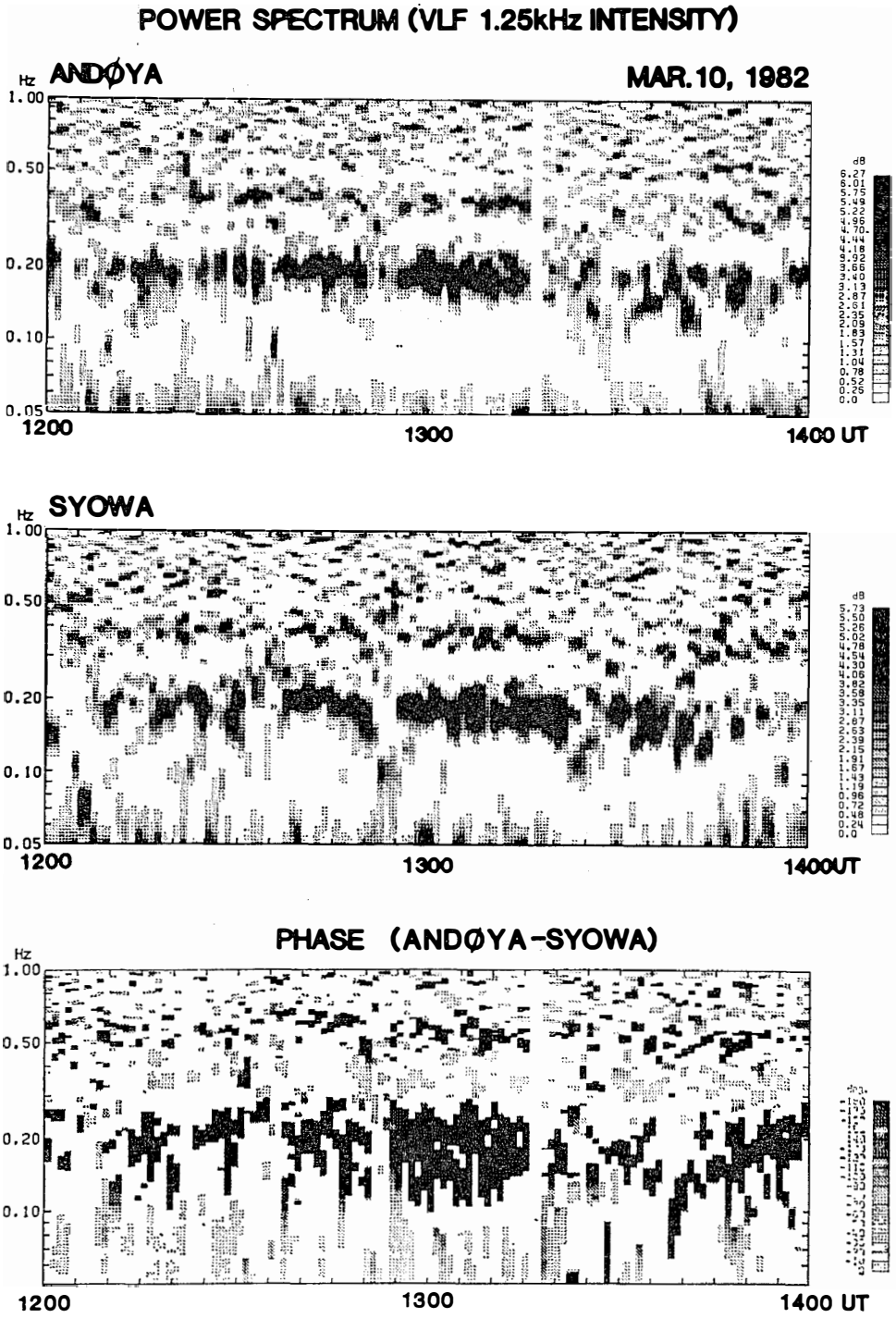

Fig. 58. Frequency-time spectrograms of the intensities of 1.25 kHz band emission observed at Andøya and Syowa in the time interval of 1200–1400 UT on March 10, 1982. (a) and (b) show the power spectra for Andøya and Syowa, respectively, and (c) shows the phase spectra between them. In gray scale display of (c), a dark color represents out of phase (180°) relation. A noticeable band at 0.2 Hz in each panel indicates the occurrence of periodic emissions.

Table 4. Summary of the occurrence of periodic emissions observed during March 1–26, 1982. N and S denote the occurrence of periodic emissions in the northern hemisphere (Andøya) and in the southern hemisphere (Syowa Station), respectively.

Date		04 UT		08		12		16
1982 March	1	N		N				
	5					N	S	
	6		S		S			
	8			N	S	N	S	
	9	N	S	N				
	10			N		N	S	
	11			N				
	12					N		
	14			N	S			
	15					N	S	
	16						S	
	17				S			
	19			N				
	23	N						

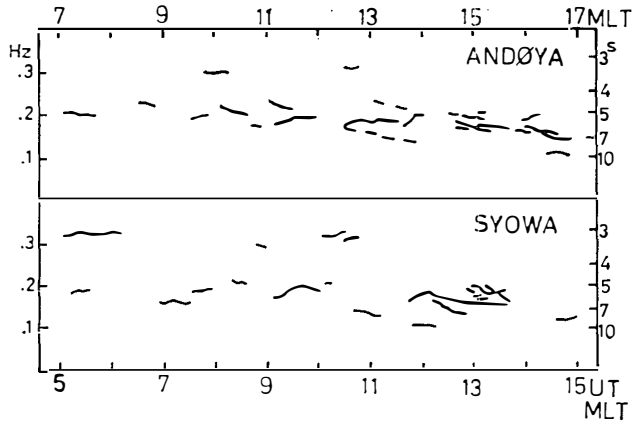

Fig. 59. Repetition intervals of periodic emissions observed at Andøya and Syowa in March 1982 as a function of magnetic local time.

table, symbols N and S denote the occurrence of periodic emissions in the northern hemisphere (Andøya) and in the southern hemisphere (Syowa), respectively, for each of the time intervals of 04–08, 08–12 and 12–16 UT. The repetition intervals of the periodic emissions obtained from the frequency-time spectrograms are summarized in Fig. 59 as a function of magnetic local time. The repetition interval ranges from 3 s to 10 s with its mean value around 5 s, and it becomes longer towards evening hours. This is possibly due to the increase of electron density with local time in the dayside magnetosphere often observed by GEOS satellites (*e.g.* DÉCRÉAU *et al.*, 1982; XIAO-TING and CAUDAL, 1987). As the group velocity of whistler mode waves is inversely proportional to the square root of the electron density along the propagation path, the above local time variation of the electron density will cause a decrease in the group

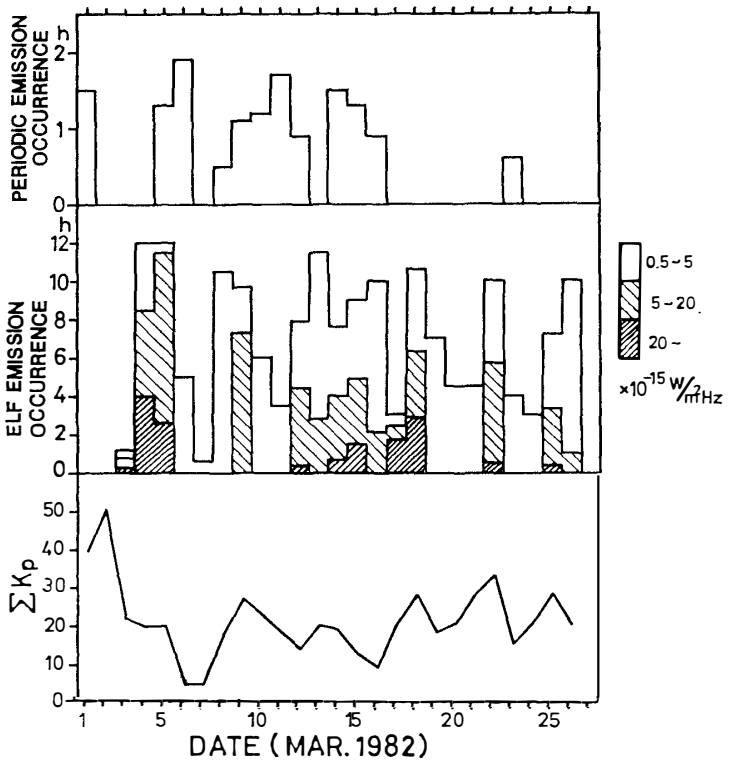

Fig. 60. Daily duration of periodic emissions of 1.25 kHz band observed at Andøya (upper panel), and that of 1.25 kHz emissions for three intensity levels, i.e. 5×10^{-16}, 5×10^{-15} and 2×10^{-14} W/m²·Hz (lower panel). Daily sum of Kp index is also shown at the bottom of the figure.

velocity and an increase in the bounce period of ELF waves with local time.

In Fig. 60, the upper panel shows the daily duration of periodic emissions of 1.25 kHz band observed at Andøya, and the lower panel shows the daily duration of 1.25 kHz emissions observed at Andøya for three intensity levels, *i.e.* 5×10^{-16}, 5×10^{-15} and 2×10^{-14} W/m² Hz. The daily sum of *Kp* index is also shown at the bottom of the figure. The daily occurrence rate of periodic emissions, defined as the total daily duration of periodic emissions divided by that of ELF emissions above 5×10^{-16} W/m² Hz in their intensity, lie within a range of 5–50% for the days of periodic emission occurrence, and the averaged occurrence rate during March 1–26 is 6%. This means that the occurrence rate of ducted propagation near $L=6$ is relatively low, and the majority of ELF emissions observed on the ground is thought to be propagated in nonducted mode. This inference is consistent with the ELF wave observation by ISIS satellites described in Sections 3.2 and 3.3, *i.e.*, the wave normal direction obtained from the spin-modulated characteristics and $L=0$ cutoff characteristics of ELF waves distributed around a certain large angle with respect to $\boldsymbol{B}_0$, and this feature is only explainable by nonducted propagation. In VLF range, waves propagated in nonducted mode are seldom observed on the ground, because they are totally reflected at the bottom of the ionosphere due to a large incident angle. However, in ELF range, a significant wave field is observed on the ground even when the wave is totally reflected. The wave field leaks out from the ionosphere to the ground in evanescent mode with

an attenuation of several dB, because the wavelength of ELF wave is much longer than the distance from the bottom of the ionosphere to the ground (KIMURA *et al.*, 1978).

Although the duration of each periodic emission event is only 10–120 min as shown in Fig. 59, Fig. 60 indicates a tendency that once periodic emissions occur, they appear frequently on several consecutive days. This will mean that once the condition for periodic emission occurrence is set up in the magnetosphere, it remains for several days.

4.3. Spatial extent of periodic emissions

A regular repetition of periodic emissions suggests that these emissions propagate along field-aligned ducts. Consequently, when a periodic emission is observed in one hemisphere, the emission originated from the same source is expected to reach the geomagnetic conjugate point in the opposite hemisphere. Although Andøya is separated 1600 km from the conjugate point of Syowa Station, periodic emissions were often observed simultaneously at the both stations, as shown in Table 4. This suggests that the longitudinal extent of periodic emission is as wide as 1600 km on the ground. A similar feature was reported by BRICE (1965) that periodic emissions in the frequency band of 1.2–1.7 kHz were observed simultaneously at two conjugate pairs of stations: Quebec City in Canada and Eights Station in Antarctica, Great Whale River in Canada and Byrd Station in Antarctica. These two conjugate pairs are separated by 1000 km in latitude and 500 km in longitude. He reported another case that a periodic emission in the frequency band of 2.5–3.0 kHz was observed at Seattle and Byrd. The conjugate point of Byrd is located 3100 km apart from Seattle. Figure 61 shows the locations of these observation sites (solid circles and triangles) and their geomagnetic conjugate points (open circles and triangles). Circles surrounding these sites have a diameter of 2200 km.

If wave frequency is higher than the cutoff frequency of the earth-ionosphere wave guide, the wave can propagate over a long distance with a small attenuation. Periodic emissions observed at Seattle and Byrd might have propagated in the wave guide mode, because the wave frequency is higher than the cutoff frequency of wave guide mode, f_c, which is about 2 kHz in the daytime. In other cases, a wide extent of the emission received on the ground cannot be explained by a propagation below the ionosphere, because the wave frequency is lower than f_c. Therefore, the above example of a wide extent of the wave receiving area must be attributed to a spread of periodic emissions from the topside ionosphere.

In fact, periodic emissions were observed by ISIS-2 satellite in a wide latitude range of 50°–75° INV at an altitude of 1400 km (SATO, 1984). Figure 62 shows the intensity records of 850 Hz band periodic emissions (bandwidth is 42 Hz) simultaneously observed at ISIS-2 and at Syowa Station on August 8, 1981, where the emission amplitude is shown in an arbitrary linear scale. The ground-based data at Syowa Station show the persistent periodic emissions during 1455–1512 UT, while the ISIS-2 data show the dependence of the emission intensity on the satellite position with no emission at latitudes higher than 75° INV after 1506:40 UT. Figure 63 shows the geomagnetic foot point of ISIS-2 satellite orbit projected onto a geographic map of Antarctica with the geomagnetic coordinates shown by broken lines. The spatial

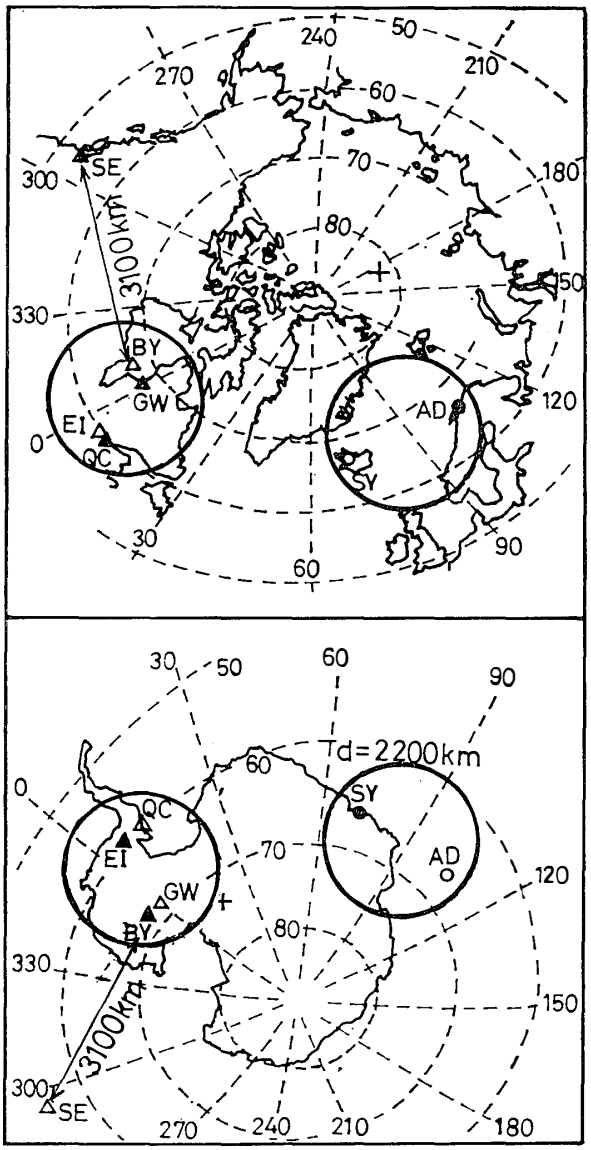

Fig. 61. Spatial relationship between VLF stations where periodic emissions were simultaneously observed. The stations are marked by solid circles and triangles, whereas their geomagnetic conjugate points are shown by open ones.

intensity distribution of the periodic emission observed at the satellite is schematically illustrated in gray scale along the satellite orbit. The latitudinal extent of the region of highest intensity level (marked as black) is 1100 km at an altitude of 1450 km. The extent is broadened to as much as 2000 km at the level of the ionosphere if the maximum deviation of ray paths from the field line is taken as 20° (HELLIWELL, 1965). The above extent is comparable to the one inferred from the ground-based observations of periodic emissions shown in Fig. 61. The extent of the second-highest intensity level is 4700 km at an altitude of 1450 km. This value may have been underestimated because the low latitude boundary of this emission must have been beyond the limit of the satellite telemetry reception from Syowa Station. This wide extent is explained by a spread of

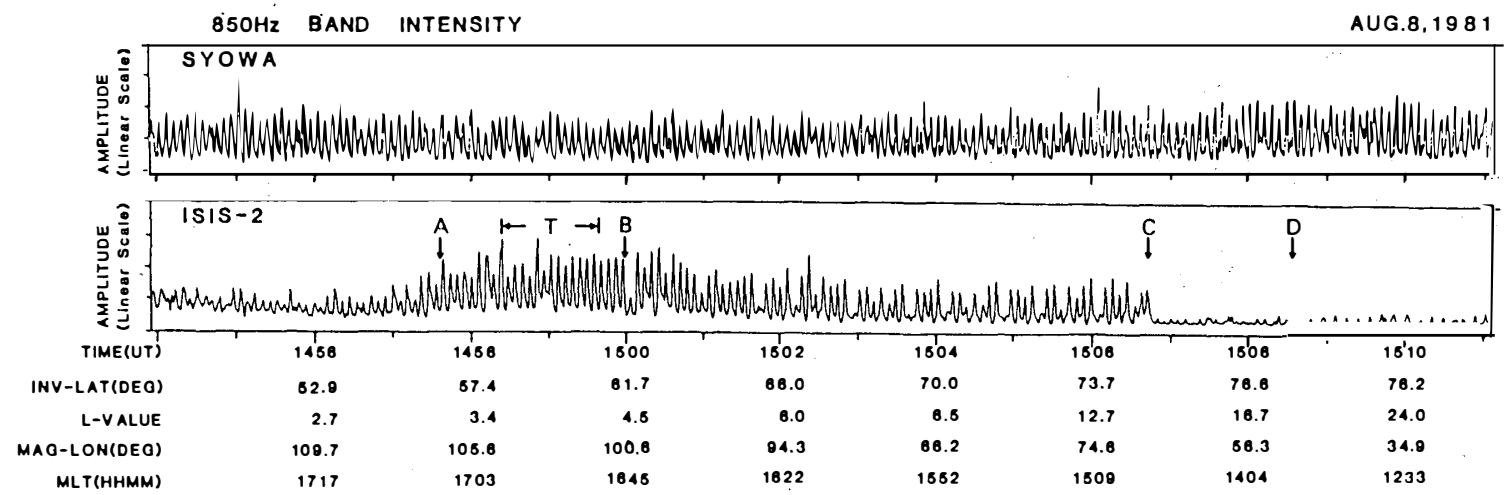

Fig. 62. Intensity records of 850 Hz band periodic emission simultaneously observed at ISIS-2 (upper panel) and at Syowa Station (lower panel) on August 8, 1981. Amplitude of the emission is shown by arbitrary lineary scale (after SATO, 1984).

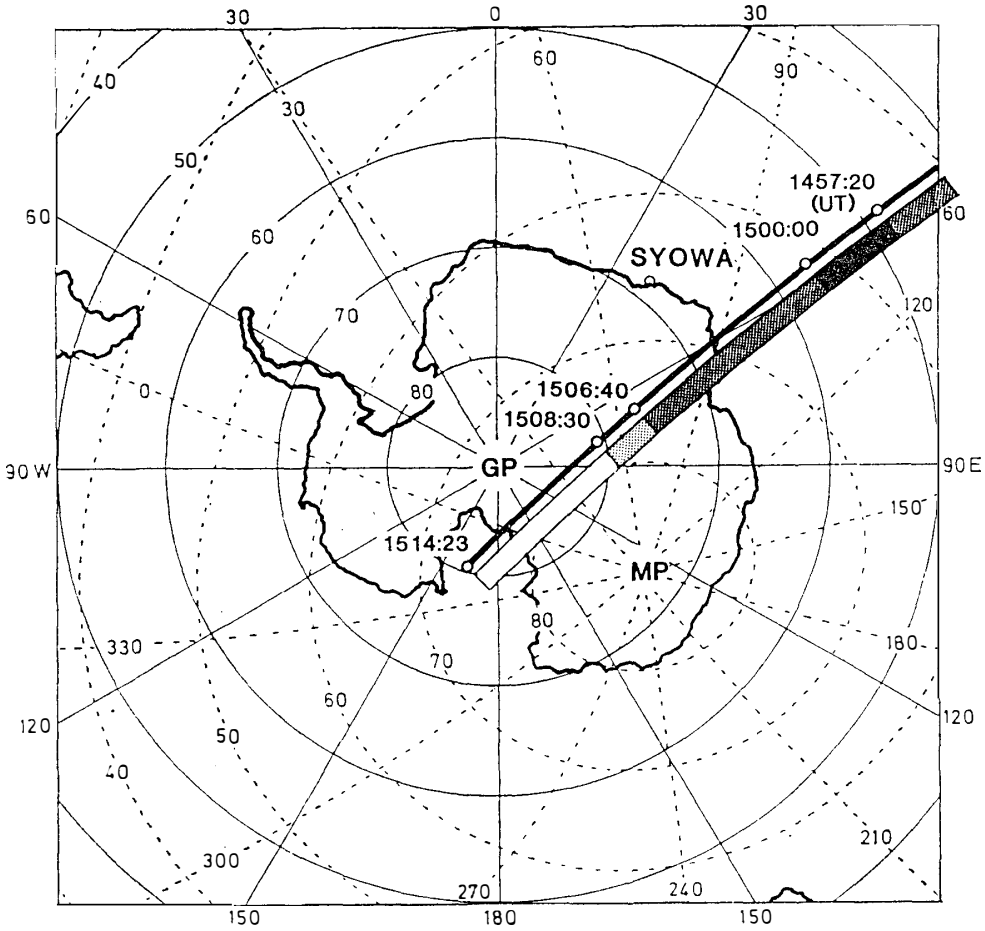

Fig. 63. Geomagnetic foot point of ISIS-2 satellite orbit projected onto a geographic map of Antarctica with the geographic coordinate shown by broken lines. The spatial intensity distribution of the periodic emission observed at the satellite is schematically illustrated in gray scale along the satellite orbit (After SATO, *1984).*

upgoing waves reflected at the bottom of the ionosphere. A similar idea was adopted in the explanation for a wide latitudinal extent of ducted whistlers observed by ISIS-2 (THOMSON and DOWDEN, 1977). Figure 64 shows the frequency-time spectrogram for the intensity of 850 Hz band periodic emissions shown in Fig. 62. The upper panel is for the ISIS-2 observation, and the lower panel for the observation at Syowa Station. The repetition period observed by the satellite remains almost unchanged at 0.2 Hz for the whole interval of periodic emission occurrence, although the satellite moved from 50° INV to 75° INV in the above time interval.

There are two possibilities in understanding the spread of periodic emissions in the topside ionosphere: one is a large dimension of ELF duct, and the other is "partly ducted propagation", *i.e.*, the waves released from duct exit spread widely as they propagate downward. In the former interpretation, the required size of the duct on the equatorial plane is about 4 R_E in order to explain the observed extent of wave arrival region on the ground shown in Fig. 61. This size is too large for a usual ELF duct. Moreover, the bounce period of whistler mode waves must vary significantly within such a wide range of L shells due to the spatial dependence of field line length

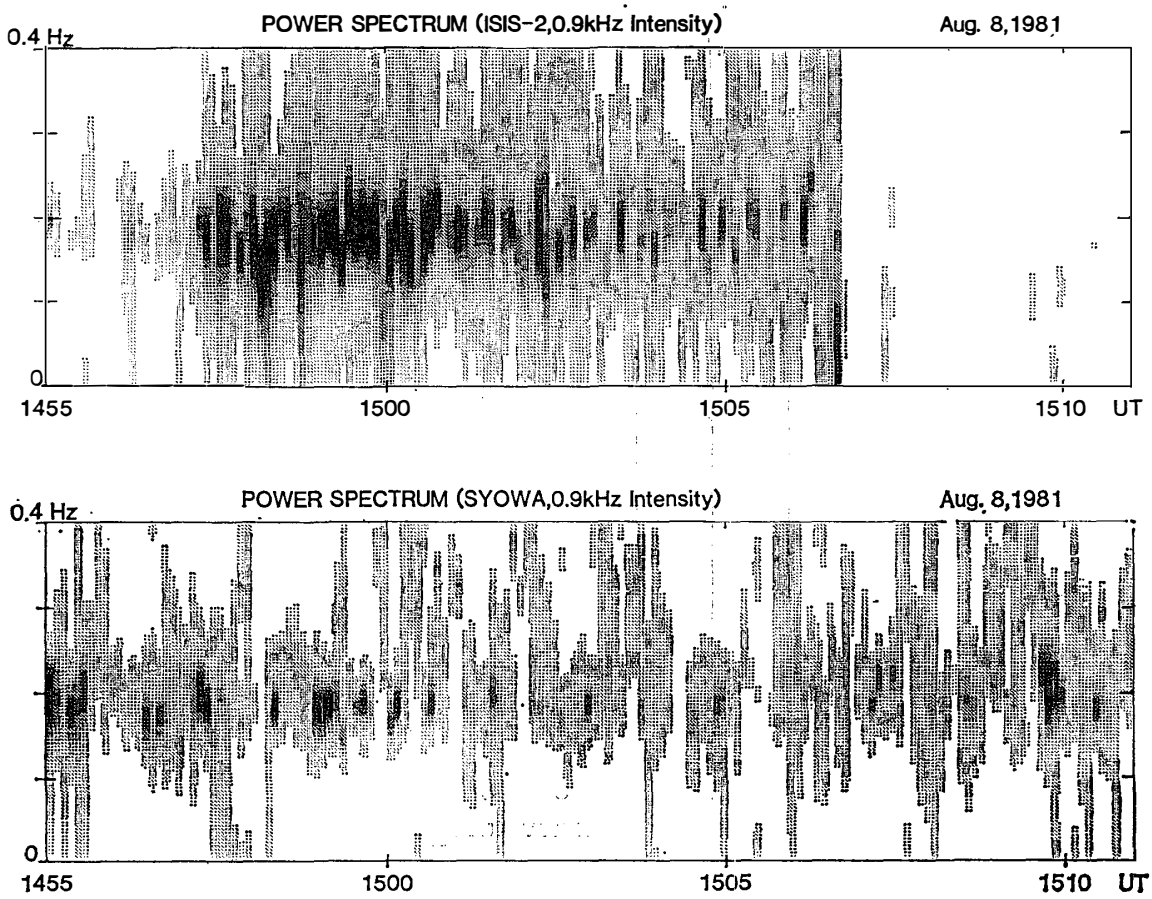

Fig. 64. Frequency-time spectrogram for the intensity of periodic emissions shown in Fig. 62. The upper panel is for the ISIS-2 observation and the lower panel the observation at Syowa Station.

and electron density for different L values However, the satellite observation of periodic emissions showed a constant repetition interval for a wide latitudinal range as shown in Fig. 64. Therefore, the extent of the emission observed on the ground and at the satellite altitude must be explained by the latter interpretation, *i.e.*, partly ducted propagation. In this propagation mode, the spatial extent of waves at the ionosphere and on the ground is dependent upon the altitude of the end point of duct. The following section shows the relationship between the altitude of the end point and the extent of waves at the ionosphere after an analysis by ray tracing method.

4.4. Diverging of ray paths from ELF duct exit

In Section 4.3, it is found that periodic emissions extend both latitudinally and longitudinally on the ground as shown in Fig. 61. Hence a 3-dimensional ray tracing is required in understanding the above extent. However, in the case of large dip angle of the geomagnetic field, propagation characteristics in the off-meridian plane is not much different from the one in the meridian plane. The dip angle at Andøya and Syowa Station is fairly large (78° and 65°, respectively). Therefore, the ray paths in the meridian plane can be obtained by a 2-dimensional ray tracing, and the results can be applied also to the estimation of longitudinal deviation of ray paths.

Figure 65 shows three models of electraon density profile used in the following

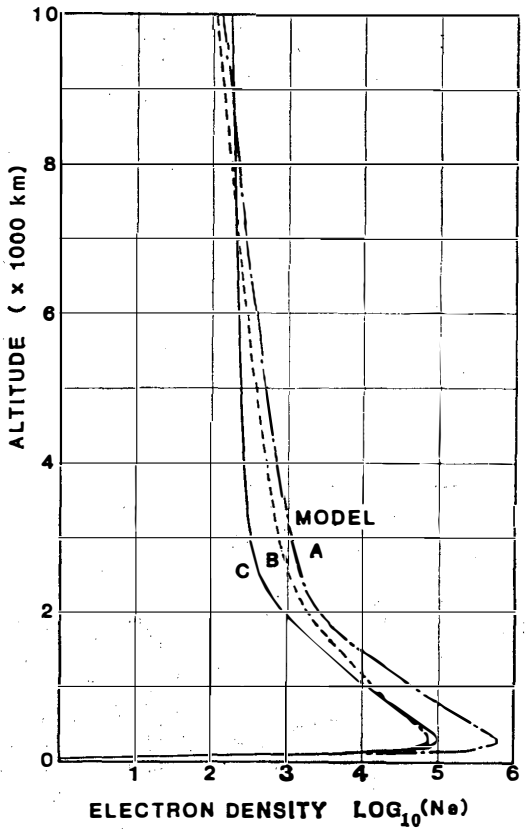

Fig. 65. Three models of electron density profile used in the ray tracing.

ray tracing. In models A and B, diffusive equilibrium distribution in the lower altitude and collision free distribution in the higher altitude are smoothly connected by an arc-tangent function (AIKYO and ONDOH, 1971) at the altitudes of 2000 and 1430 km, respectively. The former simulates the profile in the summertime and the latter the one in the wintertime. Model C is a simple diffusive equilibrium model with the reference height of 600 km and the electron temperature of 2400 K.

By means of the ray tracing method, we calculated the relationship between the altitude of the duct exit and the spread of the ray paths at the ionosphere, after assuming three altitudes of the exit point: 9000, 6000 and 3000 km.

In the first case, the duct exit was assumed at an altitude of 9000 km along the field line of $L=6.1$. In Fig. 66, ray paths of 1.5 kHz waves for electron density models A, B and C are illustrated in Figs. 66a, 66b and 66c. The ray paths labeled as 1 to 7 are calculated for the following different wave normal angles given at the end point of duct: $\psi_i=60°$, 40°, 20°, 0°, $-20°$, $-40°$, and $-60°$. The angle ψ_i is measured from the earth's magnetic field $\boldsymbol{B}_0$, and a positive value of ψ_i is given to the wave normal directing poleward. The wave normal measurement of ELF hiss outside the plasmapause revealed that ψ was confined within a cone whose axis is parallel to $\boldsymbol{B}_0$ and the half angle of 40° in the case of ducted propagation (BURTON and HOLZER, 1974). In this paper, the ray paths were calculated for a wider range of ψ_i from $-60°$ to 60°. Later, it will be shown that the ray paths with ψ_i greater than 40° are not effective in increasing the wave extent at the altitude of the ionosphere. In the figure, some of

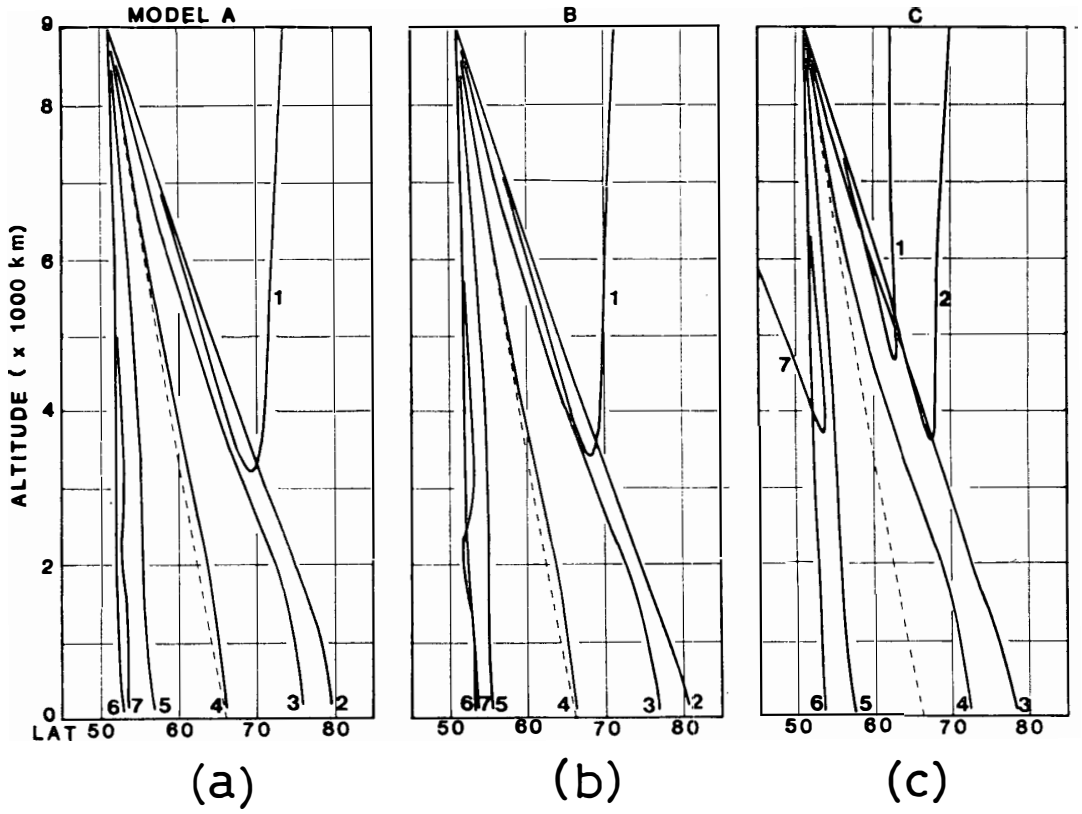

Fig. 66. Calculated ray paths of 1.5 kHz wave from the end point of duct located at an altitude of 9000 km at $L=6.1$. Ray paths for models A, B and C are shown in (a), (b) and (c), respectively. Ray paths labeled 1 to 7 are calculated for the following wave normal angle given at the end point of duct: 60°, 40°, 20°, 0°, −20°, −40° and −60°. The thin broken lines show the magnetic field line of $L=6.1$.

the ray paths show reflection in the altitude range of 3200–4700 km. As the wave frequency of 1.5 kHz is lower than the LHR frequency in this altitude range (about 3 kHz for these models), the reflection is considered to be the LHR reflection explained in Section 2.3. To confirm this inference, the wave normal angles along these ray paths were examined. Figure 67 shows the wave normal angles along the ray paths shown in Fig. 66c. The wave normal angles for ray paths 1, 2 and 7 become perpendicular to $\boldsymbol{B}_0$ at altitude of 4700, 3200 and 3500 km, respectively. At these altitudes, the condition for LHR reflection, *i.e.* $f \leq f_{\mathrm{LHR}}$ and $\psi=90°$, is satisfied and the wave is reflected as shown in Fig. 66c.

The arriving latitude of rays at an altitude of 100 km showed a dependence on the electron density profile model, *e.g.* the ray path labeled as 4 arrives at 66° in models A and B, and at 72° in model C. However, the latitude range occupied by these rays at the altitude of 100 km is not much different between these three models (28° in models A and B, and 25.5° in model C).

In the second case, the duct exit is assumed to lie at an altitude of 6000 km at $L=6.1$. Figure 68 shows the calculated ray paths from the duct exit with initial wave normal angles in the range of −60° to 60° for three electron density models A, B and C. The altitude dependence of the wave normal angles along the ray paths for model

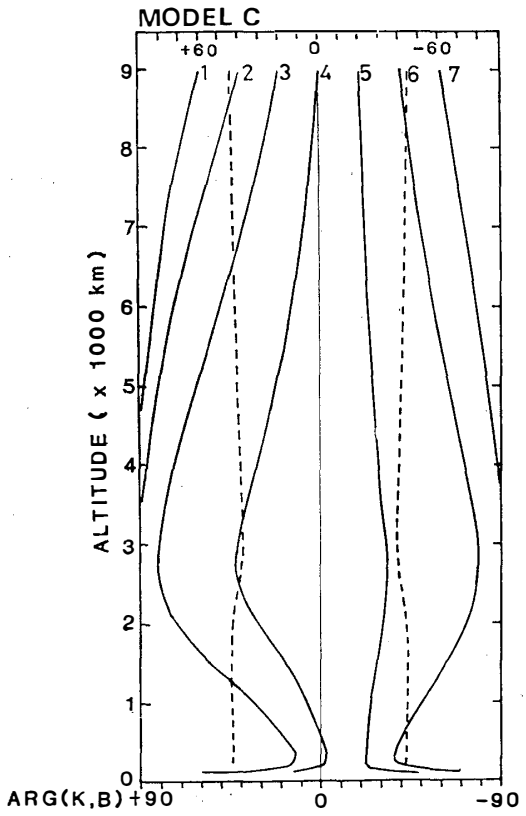

Fig. 67. Wave normal angles along the ray paths shown in Fig. 66c. The broken lines show inflection angle, ψ_{IA}.

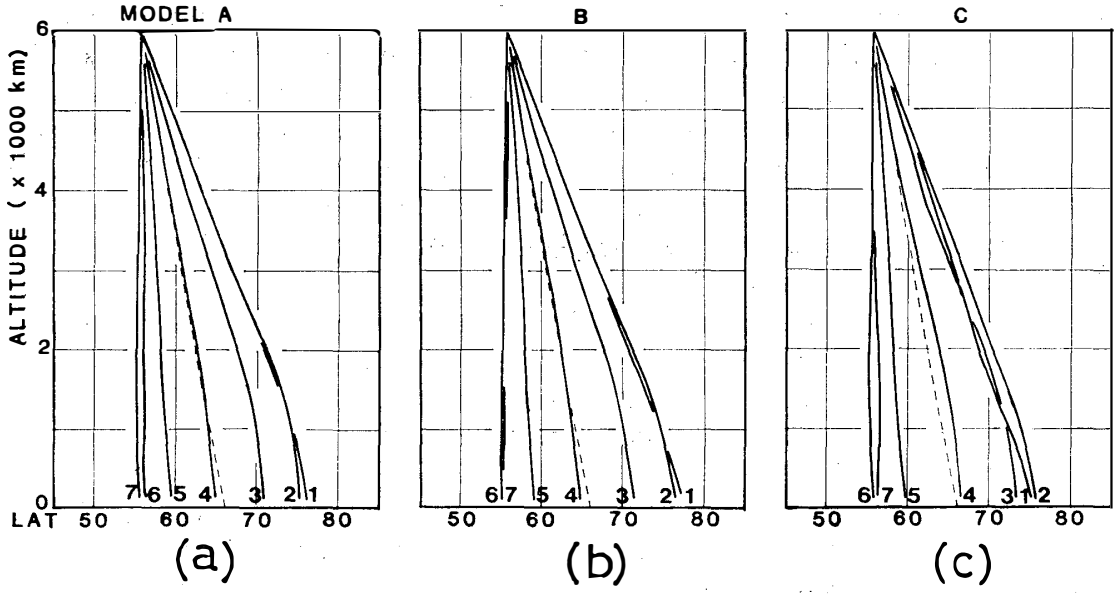

Fig. 68. The same as Fig. 66 except that the altitude of the end point of duct is 6000 km.

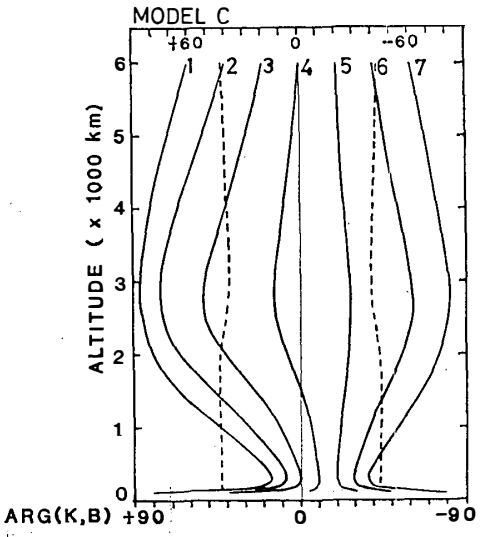

Fig. 69. Wave normal angles along the ray paths shown in Fig. 68c. The broken lines show ψ_{IA}.

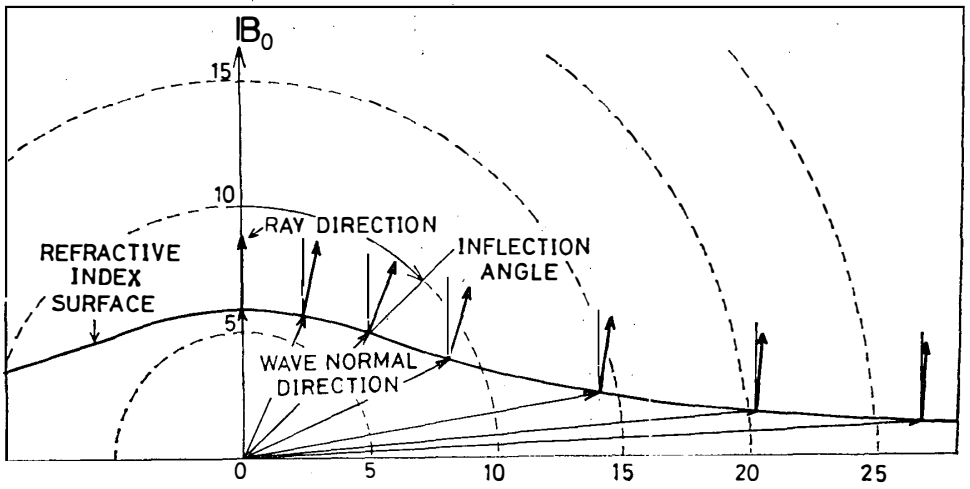

Fig. 70. Relation between the wave normal direction and the ray direction for the refractive index curve at an altitude of 3000 km.

C is shown in Fig. 69. In Fig. 68, none of the ray paths show reflection. This comes from the fact that the wave normal angle along these ray paths does not reach 90° as shown in Fig. 69, and the condition for LHR reflection is not satisfied.

In Fig. 68, the arriving latitude of ray paths at an altitude of 100 km is in order of the value of ψ_i as long as $|\psi_i|$ is within 40° (ray paths 2–6). However, when $|\psi_i|$ becomes as large as 60°, the above order is violated (ray paths 1 and 7 in Fig. 68c). The violation also occurs in the first case for $|\psi_i| = 60°$ (ray path 7 in Figs. 66a and 66b). This tendency is understood by examining the ray direction along the ray path for which the violation occurs. The ray direction is given as the normal of the refractive index curve, as shown in Fig. 70. The ray angle shows the maximum deviation from $\boldsymbol{B}_0$ when $\psi = \psi_{IA}$. For $\psi < \psi_{IA}$, the ray angle increases with increasing ψ, while for $\psi > \psi_{IA}$, the ray angle decreases with increasing ψ. The calculated value of

ψ_{IA} is illustrated by broken lines in Fig. 69. For the ray paths 1 and 7, the wave normal angle shown in Fig. 69 is larger than ψ_{IA} for most part of the propagation path. This means that the ray direction along these ray paths shows a smaller deviation from $\boldsymbol{B}_0$ as compared with that of adjacent ray paths. Thus, ray paths 1 and 7 are crossed over by adjacent ray paths, and the order of arriving latitude of the ray paths is changed. Hence the ray path with the wave normal angle exceeding ψ_{IA} for a considerable part of the propagation path makes little contribution to the spatial extent of ray paths at the altitude of the ionosphere. The spatial extent of waves is almost independent of the electron density profile. The range of latitude occupied by these ray paths is 21°, 22° and 20.4° for models A, B and C, respectively.

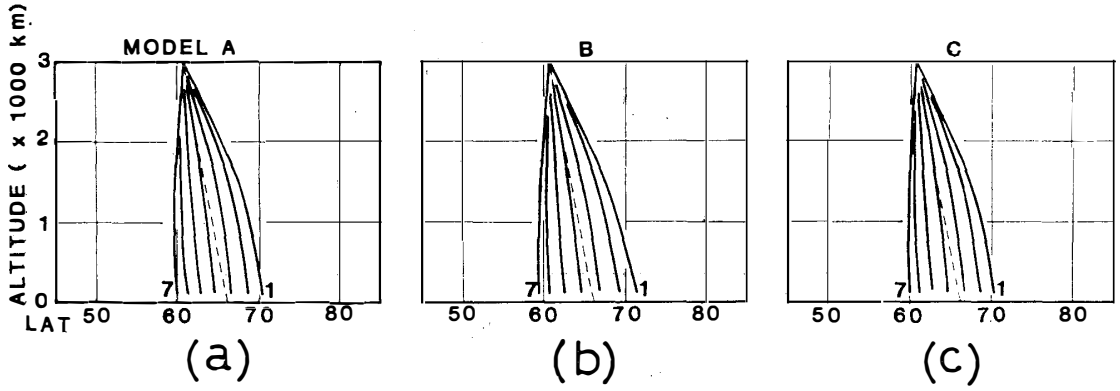

Fig. 71. The same as Fig. 66 except that the altitude of the duct exit is 3000 km.

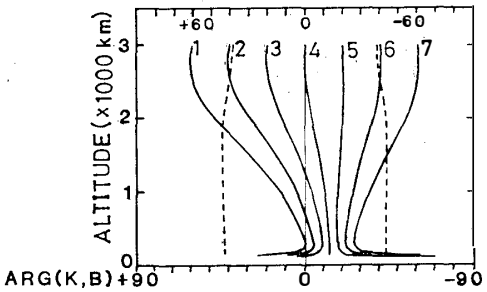

Fig. 72. Wave normal angle along the ray paths shown in Fig. 71c. The dashed lines show ψ_{IA}.

In the third case, the duct exit is assumed at an altitude of 3000 km at $L=6.1$. Figure 71 shows calculated ray paths from the duct exit with initial wave normal angles in the range of $-60°$ to 60° for three electron density models A, B and C. The altitude variation of the wave normal angle along the ray paths for model C is shown in Fig. 72. The inflection angle is shown by broken lines in the figure. Due to a steep electron density enhancement below 2000 km shown in Fig. 65, the wave normal approach the vertical according to Snell's law. This tendency keeps the wave normal angles within the inflection angle for most part of the propagation path. Consequently, the arriving latitude of the ray path is in order of ψ_i for all values of ψ_i.

In order to obtain the relationship between the initial wave normal angle ψ_i at the duct exit and the geomagnetic latitude λ of wave arrival at an altitude of 100 km,

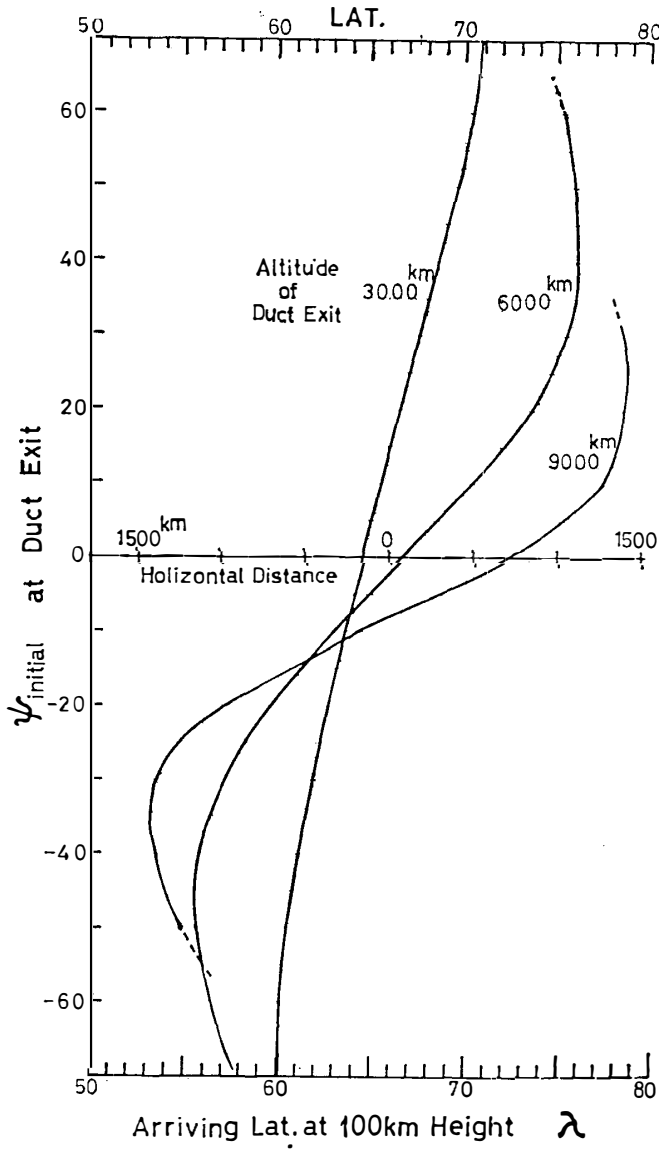

Fig. 73. Relationship between the initial wave normal angle ψ_i at the duct exit and the arriving geomagnetic latitude λ of ray path at an altitude of 100 km for three different altitudes of the duct exit. Holizontal distance measured from the foot point of duct at $L=6.1$ is also given in the abscissa.

a ray tracing was again carried out with a small increment of ψ_i for different altitudes of the duct exit, h_D. In the ray tracing, ψ_i was varied every one degree from $-60°$ to 60°, and h_D was assumed at 3000, 6000 and 9000 km. The electron density model C was used in this calculation. The relation between ψ_i and λ obtained from this calculation is shown in Fig. 73. Horizontal distance from the foot point of the duct at $L=6.1$ is also given in the abscissa. Terminations of the curves for h_D of 6000 and 9000 km indicate that the ray undergoes LHR reflection for further increase of ψ_i. There are maxima in the arriving latitude of the ray paths at ψ_i of 25° and $-32°$ for h_D of 9000 km, and at 37° and $-45°$ for 6000 km. These characteristics were already discussed in connection with the disorder in the arriving latitude of ray paths, and

explained by a change of ray direction when ψ exceeded ψ_{IA}. For h_D of 9000 km, the waves with ψ_i ranging from $-32°$ to 25° are responsible for the maximum spatial extent of ray paths at an altitude of 100 km. The required electron density enhancement in the duct is 18% above the background. For h_D of 6000 km, the required electron density enhancement to confine ψ_i to the range of $-45°$ to 37° is 40% above the background. Therefore, the spatial extent of ELF waves at an altitude of 100 km can be explained with the electron density enhancement within a reasonable range of 40% reported by BURTON and HOLZER (1974).

From the above ray tracing, the spatial extent of ray paths at an altitude of 100 km is estimated to be 1190, 2280 and 2880 km for h_D of 3000, 6000 and 9000 km, respectively. The spatial extent of the wave arrival on the ground is almost equal to the above values because of the following reason.

Snell's law requires that a downcoming whistler mode wave can reach the ground only when its wave normal lies within the acceptance cone of angle $\theta_0 \equiv \sin^{-1}(1/n_0)$, where n_0 is the refractive index for ionospheric peak electron density at an altitude of ~280 km. θ_0 is estimated to be $\pm 0.67°$ around the vertical for a wave frequency of 1.5 kHz. At the ionospheric altitude, wave normal angles of the ray paths leaving the duct bottom are in a range of $\pm 15° \sim \pm 27°$ around the vertical as illustrated in Figs. 67, 69 and 72. Therefore, only a little fraction of the wave can reach the ground, and the rest of the wave undergoes total reflection at the bottom of the ionosphere.

Taking account of the relationship between ray paths and wave normal angles shown in Figs. 66 to 72, transmission area must be within a narrow region of the ionosphere between the foot points of ray paths 4 and 5. Transmitted wave can spread wider on the ground, but its intensity will rapidly decrease due to spatial divergence. TSURUDA *et al.* (1982) observed Siple transmitter signal propagated from the Antarctica in ducted mode in Canada. They obtained an attenuation rate as high as -6 dB/100 km. A full wave calculation by NAGANO *et al.* (1986) also showed a steep attenuation of -10 dB/100 km. Hence, the spatial extent of the wave arrival on the ground is much smaller than that at the ionospheric altitude when the transmission were only through acceptance cone.

In the ELF range, however, totally reflected wave makes a considerable contribution to the ground wave field, because the free space wavelength of ELF waves is much longer than the distance between the ionospheric bottom and the ground, and a significant fraction of the wave field leaks out from the ionosphere to the ground in evanescent mode. NAGANO *et al.* (1987) obtained the leaked wave field intensity by a full wave calculation as 15 dB smaller than that of the transmitted wave through acceptance cone. This means that a narrow area (a few hundreds of km) of transmitted wave is surrounded by a wide area of leaked wave field, and the total spatial extent of the wave arrival on the ground is almost equal to that above the ionosphere obtained by ray tracing.

The area of periodic emission reception on the ground shown in Fig. 61 is explainable by "partly ducted propagation" in which the altitude of the duct exit is around 6000 km. The reception of periodic emissions over a wide area observed by ISIS-2 on August 8, 1981 is also explainable by "partly ducted propagation". Taking account of the reflection of waves at the bottom of the ionosphere, the configurations of the duct

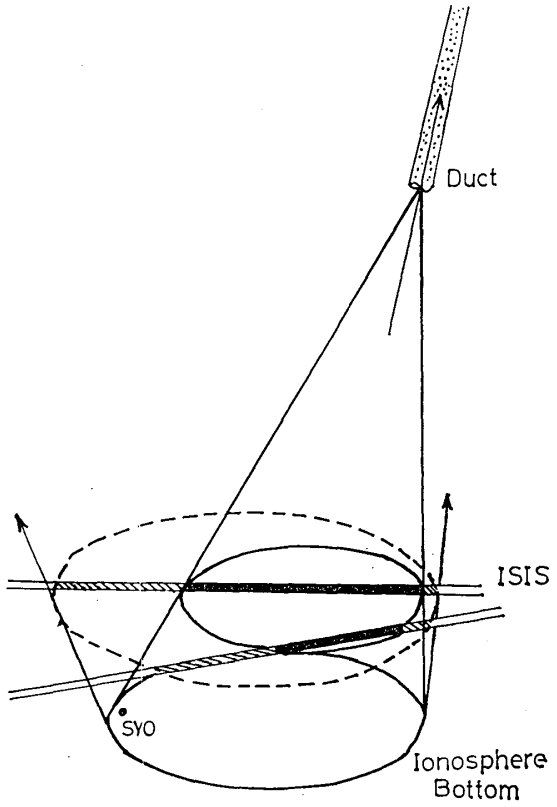

Fig. 74. Schematic illustration of the configuration of the duct and the spatial extent of the emission at the satellite altitude.

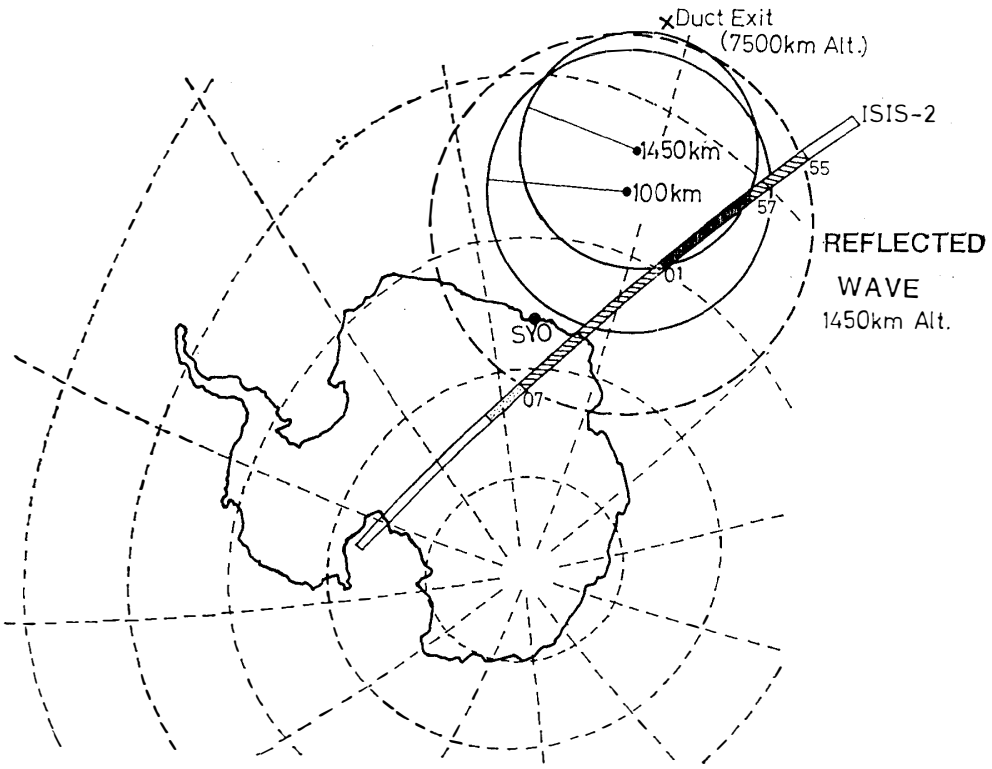

Fig. 75. Projection of the emission area at the altitude of ISIS-2 and at the bottom of the ionosphere onto a map of Antarctica when the duct exit is at an altitude of 7500 km at magnetic longitude of 89° and invariant latitude of 56°. Intensity distribution of periodic emissions observed by ISIS-2 is schematically illustrated in gray scale in the figure.

and the area of the emission reception at the satellite altitude are schematically illustrated in Fig. 74. In order to explain the spatial distribution of the periodic emission intensity shown in Fig. 63, the optimum position of the duct exit is at an altitude of 7500 km at magnetic longitude of 89° and invariant latitude of 56°. Assuming this position of the duct exit, the areas of downcoming and upgoing waves at the altitude of the satellite and the ionosphere are calculated, and they are projected onto a map of Antarctica as shown in Fig. 75. The intensity of the periodic emission along the satellite orbit shown in Fig. 63 is also illustrated in the figure for comparison.

4.5. Summary

Characteristics of periodic VLF emissions were discussed from a viewpoint of ducted propagation outside the plasmapause during their propagation from the high-altitude equatorial region to the near-earth level. In one-month continuous observation of ELF emissions at Andøya and Syowa in March 1982, periodic emissions were recorded in 6% of the whole interval. This means that the ducted propagation near $L=6$ occurs relatively infrequently, and the majority of ELF emissions observed on the ground seems to be of nonducted mode. This inference can be supported also from the ELF wave observation by ISIS satellites described in Sections 3.2 and 3.3, in which the wave normal direction obtained from the spin-modulated and $L=0$ cutoff characteristics of ELF waves forms a certain large angle with $\boldsymbol{B}_0$ direction, and this feature holds only in nonducted propagation.

The repetition interval of periodic emissions observed near $L=6$ ranges from 3 s to 10 s with its mean value around 5 s, and it becomes longer towards evening hours. This tendency is possibly due to an electron density increase in the evening in the dayside magnetosphere, which causes a decrease in the group velocity and an increase in the bounce period of whistler mode waves in the magnetosphere.

Multi-static ground-based observations and a polar-orbiting satellite observation of periodic emissions revealed that the spatial extent of the emission was as wide as about 2000 km at the ionospheric level and on the ground. This wide extent is explainable by "partly ducted propagation". Ray tracing of ELF waves from the duct exit to the ionosphere showed that the altitude of the duct exit must be 6000–7500 km in order to explain the observed extent.

5. Simultaneous Observations of ELF Emissions and Auroral X-ray

5.1. Introduction

Ray tracing of nonducted ELF waves in the magnetosphere described in Chapter 2 reveals that the ELF waves observed on the ground follow "penetrating ray paths" which have the characteristics of poleward skewing, *i.e.* the ray paths deviate to an outer L-shell during the course of downward propagation. Therefore, on the equatorial plane, the generation region of ELF waves must be located at a smaller L-value in comparison with that corresponding to the arrival altitude on the ground. Due to the above propagation characteristics, it is generally difficult to determine the source location of ELF waves from the ground-based wave observation alone.

In association with the ELF whistler-mode emissions in the magnetosphere, precipitation of high-energy electrons was often observed by Bremsstrahlung X-ray detectors on board balloons (ROSENBERG *et al.*, 1971; FOSTER and ROSENBERG, 1976; ROSENBERG *er al.*, 1981; WEST and PARKS, 1984; YAMAGISHI *et al.*, 1985; KREMSER *et al.*, 1986) and electron detectors on board satellites at synchronous orbits (PARK *et al.*, 1981; ISENBERG *et al.*, 1982; CORNILLEAU-WEHRLIN *et al.*, 1985) and at polar orbits (HOLZER *et al.*, 1974; IMHOF *et al.*, 1986). In these precipitation events, characteristic temporal variations were found in both the ELF wave intensity and in the precipitation count rates such as "bursts" in the time scale shorter than 10 s appeared in the early morning (ROSENBERG *et al.*, 1971; FOSTER and ROSENBERG, 1976; YAMAGISHI *et al.*, 1984), and "pulsations" with periods of 20–500 s appeared from the late morning to afternoon hours (WEST and PARKS, 1984; YAMAGISHI *et al.*, 1985). The close relationship between waves and precipitations suggests that the precipitation is caused by a resonant interaction of high-energy electrons with whistler-mode ELF waves in the magnetic equatorial region and the resultant pitch angle diffusion of electrons to the loss cone (*e.g.*, KENNEL and PETSCHEK, 1966; CORONITI and KENNEL, 1970; ETCHETO *et al.*, 1973; INAN *et al.*, 1982). As the precipitating electrons strictly follow a field line, a precipitation pattern observed on the ground is a sort of the projection of the wave-particle interaction region near the magnetic equaor onto the polar ionosphere. Hence the source location of ELF waves must be located on the field line at which the precipitation is observed in association with ELF.

In this aspect, Bremsstrahlung X-rays observed on the balloons launched from Norway and Syowa Station, Antarctica are compared with the ELF wave data simultaneously observed on the ground. In Section 5.2, relationship between the X-rays

and the ELF waves is studied with respect to their fluctuations with the time scale of tens of minutes for three balloon experiments which are carried out at the location of L-values 5 to 6. In Section 5.3, the relationship between rising-tone type quasi-periodic (QP) emissions and X-ray pulsations is studied. By analyzing in-phase relationship between the X-ray pulsation and ELF wave pulsation, the source locations of the different frequency components of QP emissions are determined in the magnetic equatorial region. In Section 5.4, relationship between ELF chorus bursts and X-ray bursts is examined. Mode of propagation, *i.e.* ducted or nonducted propagation, is inferred from the characteristics of the relationship with the X-ray.

5.2. Relationship between X-ray and ELF slow variations

5.2.1. B_5-28 experiment

A balloon (B_5-28) with a NaI(Tl) scintillation counter for measuring X-rays in the energy range of 20–150 keV together with VLF receiver was launched from Syowa Station (69.0°S, 39.6°E), Antarctica at 0550 UT on November 30, 1985 during the recovery phase of a magnetic substorm. Figure 76 shows the flight trajectory of this balloon. The balloon drifted eastward first, and then towards southwest. The balloon reached ceiling altitude of 32 km at 0710 UT, and then X-ray observations started.

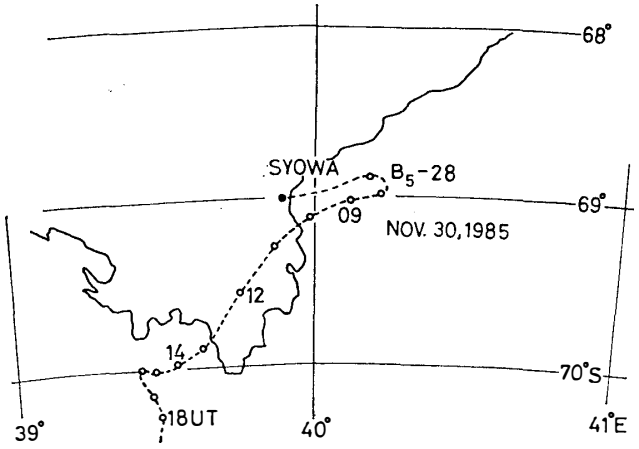

Fig. 76. Flight trajectory of B_5-28 balloon, launched from Syowa Station at 0550 UT on November 30, 1985. The balloon reached the ceiling altitude of 32 km at 0710 UT.

The ranges of L values and magnetic local time during the flight at the ceiling altitude are L=6.1–6.2 and 07–18 MLT, respectively. Presented in Fig. 77 is a summary plot of the balloon observation, *i.e.* the X-ray counting rate in the energy channels of 20–30, 30–40, 40–55, 55–88 and 88–150 keV, and the intensities of ELF emissions at the frequency of 750 Hz (the bandwidth is 40 Hz) and 1.5 kHz (the bandwidth is 75 Hz). A similarity in the time-profile of each energy channel suggests that the energy spectra of the X-ray did not change significantly during this balloon flight. The intensities of ELF waves tend to increase when the counting rates of X-rays decrease. This anti-correlation can be explained by a increased ionospheric opacity to ELF waves at the time of increased particle precipitation, which is revealed in an increased CNA of 30 MHz described in the following.

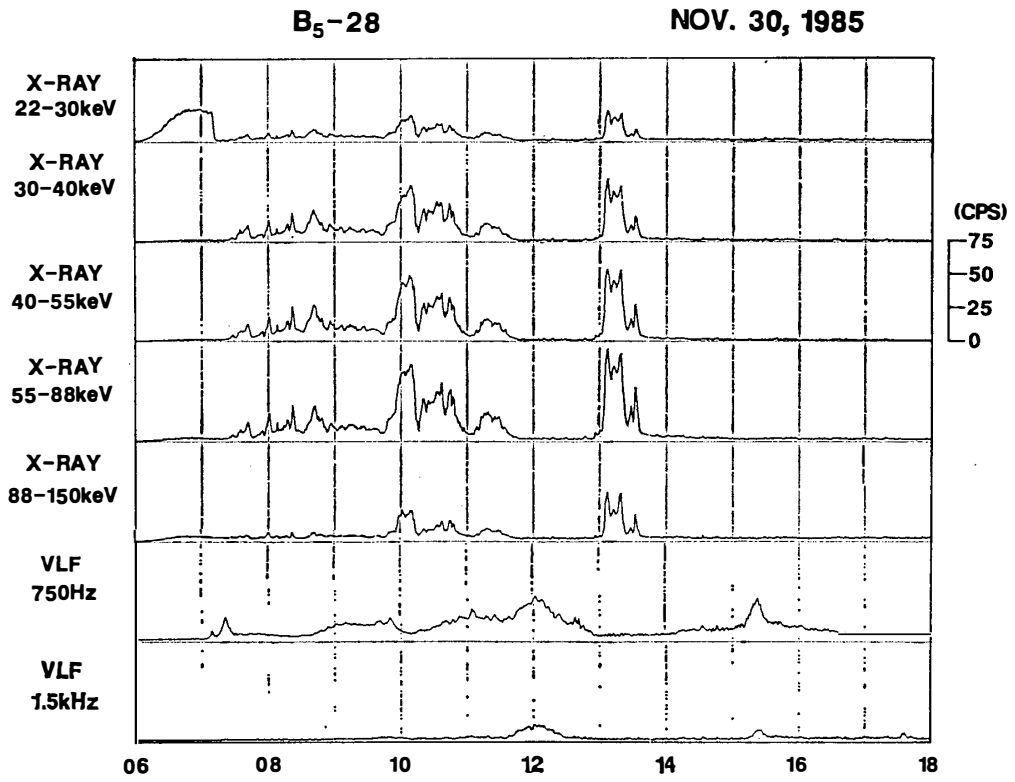

Fig. 77. A summary plot of the B_5-28 balloon observation with the X-ray counting rates in five energy channels (20–30, 30–40, 40–55, 55–88 and 88–150 keV) and ELF wave intensities at the frequency of 750 Hz and 1.5 kHz.

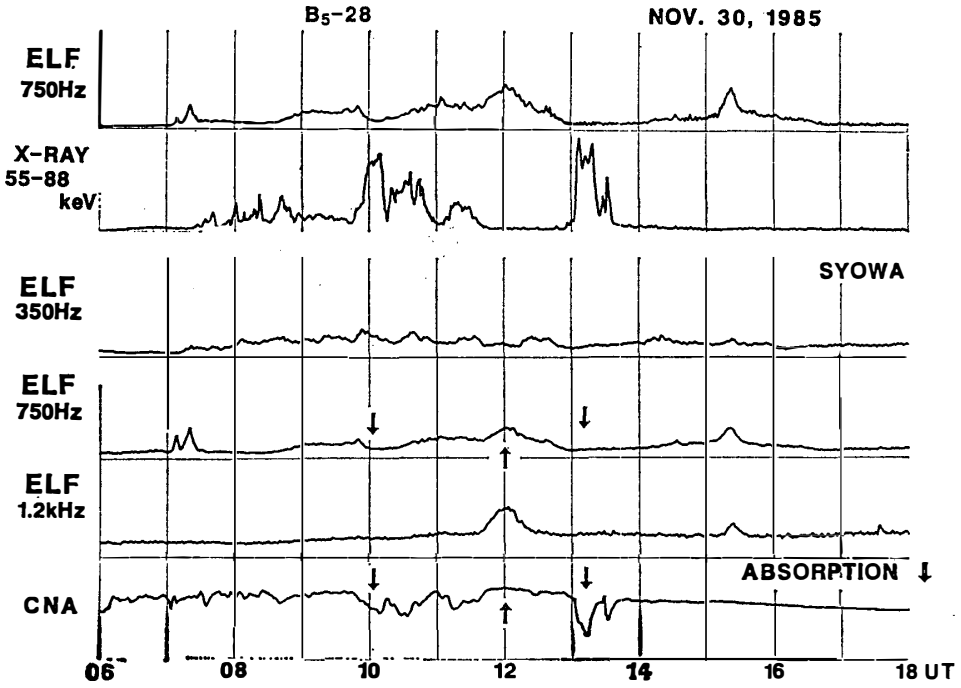

Fig. 78. A summary plot of the B_5-28 balloon observation and the simultaneous ground-based observation at Syowa Station. Top two traces show the ELF wave intensity at 750 Hz and the counting rate of X-ray in the energy channel of 55–88 keV observed by the balloon. The bottom four records are the ELF wave intensities at the frequency bands of 350 Hz, 750 Hz and 1.2 kHz, and the CNA of 30 MHz observed at Syowa Station.

In Fig. 78, the balloon observation is compared with the simultaneous ground-based observation at Syowa Station. The top two curves show the balloon observation of ELF wave intensity at 750 Hz and the counting rate of X-ray in the energy channel of 55–88 keV, and the following four records are the ground-based observation of ELF wave intensities at the frequencies of 350 Hz, 750 Hz and 1.2 kHz, and the CNA of 30 MHz. It is evident that the CNA increased with the X-ray intensity. ELF wave intensity at 750 Hz shows a general anti-correlation with CNA. This feature suggests that the 750 Hz wave observed on the ground was affected by the ionospheric absorption at the time of increased particle precipitation. On the other hand, ELF wave intensity at 350 Hz showed a positive correlation with CNA in the period of 0930–1200 UT in accordance with the expectation from the gyroresonance wave-particle interaction. The above correlation can be explained by a decreased ionospheric attenuation for the wave with its wavelength (800 km for 350 Hz wave) much longer than the distance between the ground and the bottom of the ionosphere.

5.2.2. AZCO EXW1 experiment

Figure 79 shows the flight trajectory of the balloon flight AZCO EXW1 launched from Abelvaer in the middle part of Norway at 21 UT on July 4, 1985. The balloon reached ceiling altitude of 34 km at 2230 UT, drifting westward with a speed of about

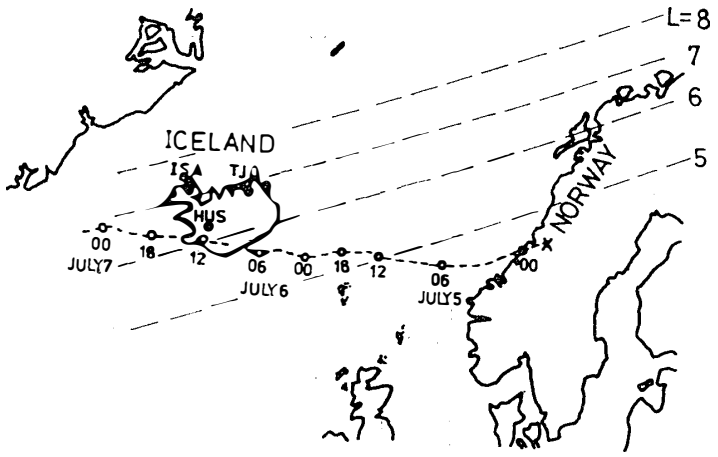

Fig. 79. Flight trajectory of AZCO EXW1 balloon launched from Abelvaer in the middle part of Norway at 21 UT on July 4, 1985. The balloon reached the ceiling altitude of 34 km at 2230 UT on July 4.

45 km/h and passed over the south coast of Iceland during 07–14 UT on July 6. Figure 80 shows a summary of the balloon X-ray observation during 06–18 UT on July 6, where the counting rates of X-ray in the energy bands of 25–50, 50–75, 75–100, 100–150 and 150–200 keV are illustrated. Figure 81 compares the balloon X-ray of 50–75 keV, shown in the top panel, with the ground-based observations of ELF waves at the frequencies of 750 Hz and 2 kHz, CNA, H component of magnetic variation and magnetic pulsation, observed at Husafell in Iceland, shown in the lower panel. General anticorrelation between X-ray and ELF waves and a close correlation between X-ray and CNA can be recognized in these data similar to previously described B_5-28 balloon experiment shown in Fig. 78.

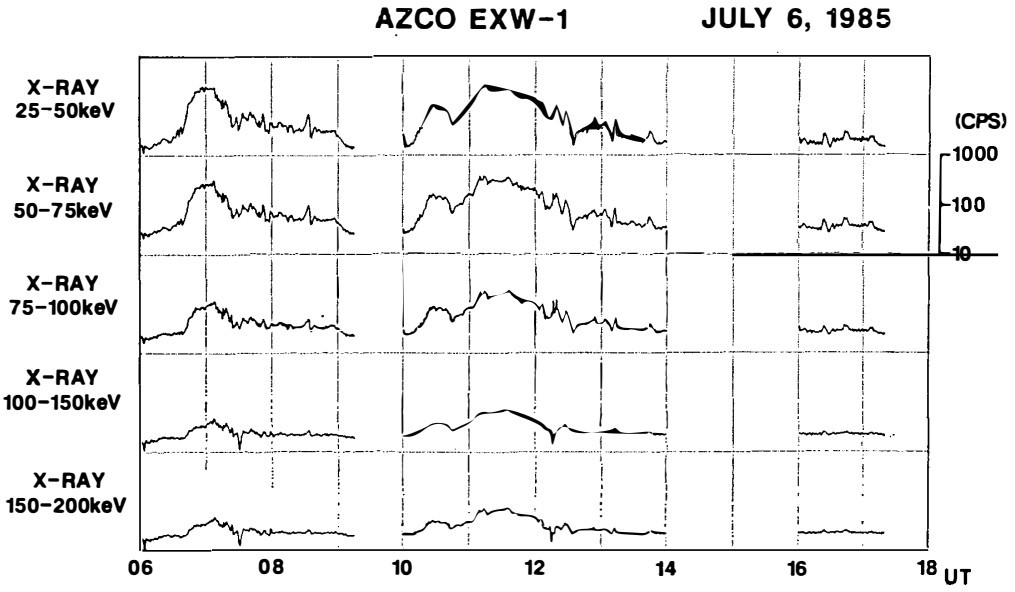

Fig. 80. A summary of the X-ray observation by AZCO-EXW1 balloon in the period of 06–18 UT on July 6, 1985. Counting rates in the energy channels of 25–50, 50–75, 75–100, 100–150 and 150–200 keV are shown.

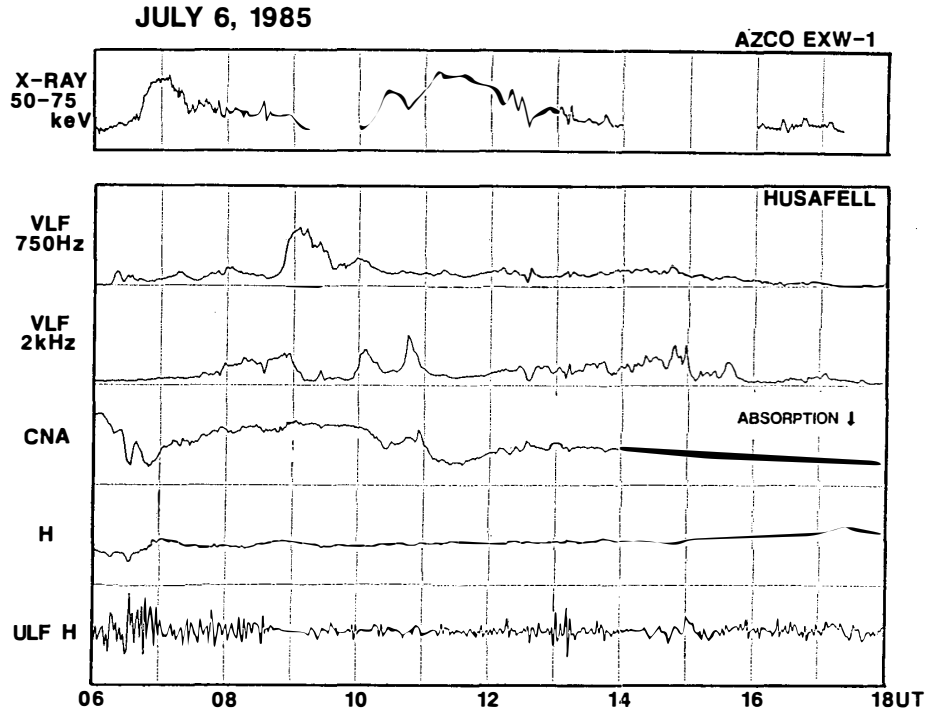

Fig. 81. A summary plot of the X-ray observed by AZCO EXW1 balloon (top panel) and the simultaneous ground-based observation at Husafell in Iceland (lower panel).

5.2.3. B_{15}-3N experiment

Presented in Fig. 82 is the flight trajectory of B_{15}-3N balloon, launched from Stamsund in northern Norway at 0632 UT on March 19, 1982. The balloon drifted eastward and the payload was cut down at 1026 UT over Finland. The balloon

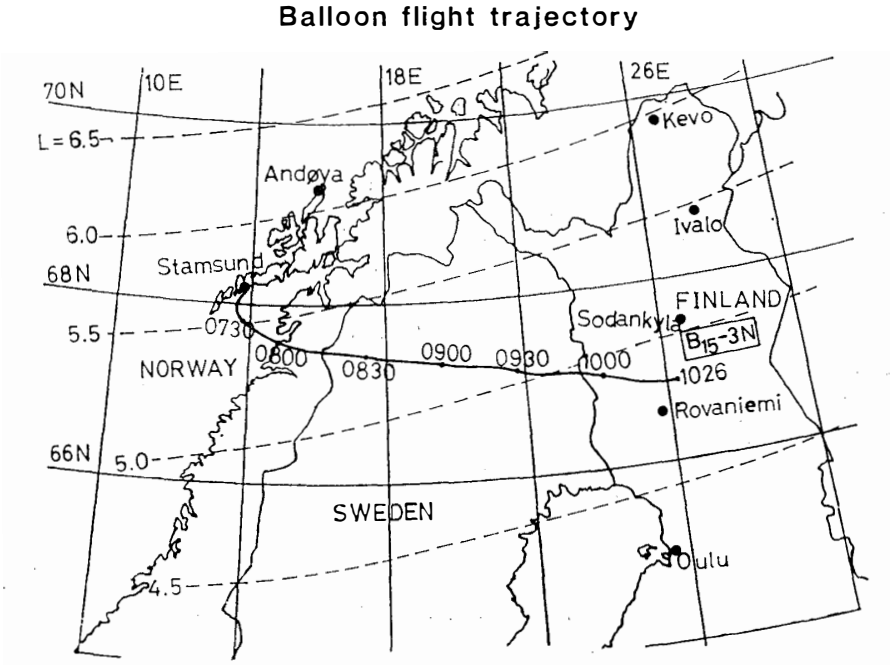

Fig. 82. Flight trajectory of B_{15}-3N balloon launched from Stamsund in northern Norway at 0632 UT on March 19, 1982. The balloon drifted eastward and the payload was cut down at 1026 UT over Finland. The balloon reached the ceiling altitude of 32 km at about 08 UT.

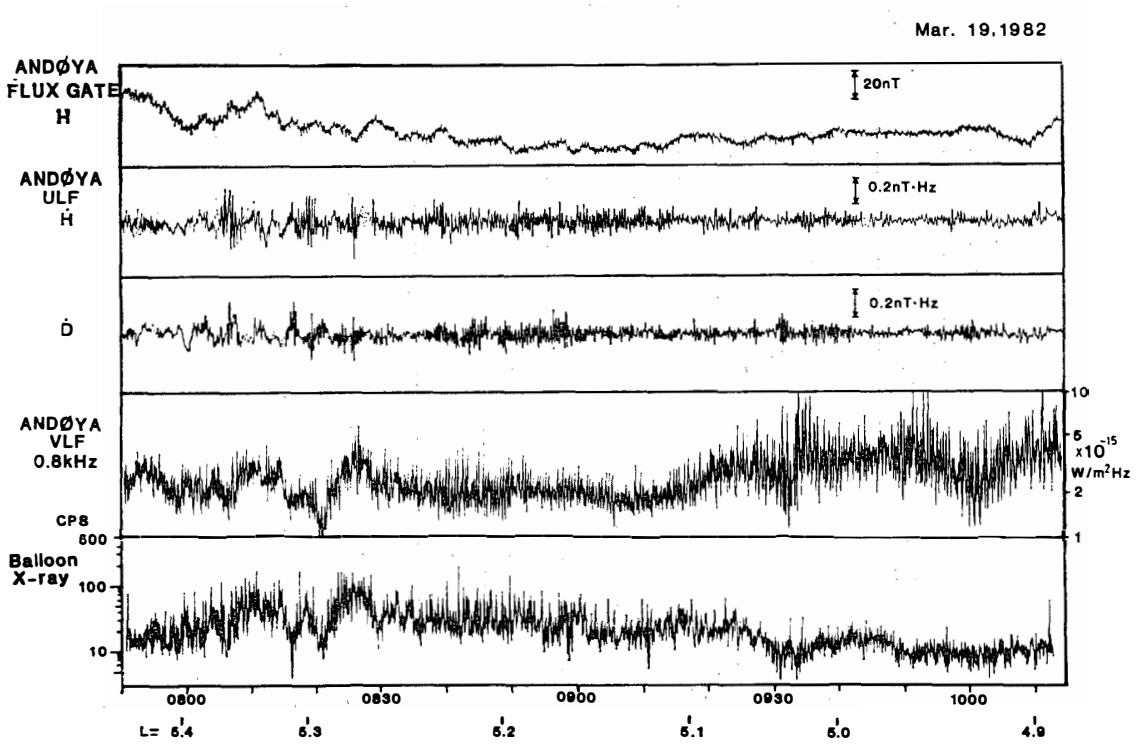

Fig. 83. Data summary of magnetic variation (H component), ULF magnetic pulsation (H and D components) and ELF emission intensity (0.8 kHz) recorded at Andøya, 160 km northeast of the launching place, and the counting rate of X-ray measured on B_{15}-3N balloon. Note that the intensity variation of ELF emission is quite similar to that of X-ray.

reached ceiling altitude of 32 km at about 0800 UT, thereafter the onboard X-ray observation being operative. The X-ray instrument of this balloon measured the temporal variation of the X-ray intensity with only one energy channel above 20 keV. The ranges of L-value and magnetic local time (MLT=UT+2.0~UT+2.5 hours) throughout the entire flight were L=5.4 to 4.8 and from 0950 to 1300 MLT, respectively.

Figure 83 shows the data summary of the X-ray counting rate observed by the balloon (bottom record) and the simultaneous ground-based observation of magnetic variation (H-component), ULF magnetic pulsations (H- and D-components), and 0.8 kHz ELF emission intensity recorded at Andøya, 160 km northeast of the launching place. It is evident that the X-ray data comprise rapid temporal variations such as bursts and pulsations which will be discussed later in Sections 5.3 and 5.4. Note that variations of ELF emission intensity observed at Andøya (L=6.1) and the X-ray observed on the balloon (L=5.4–4.9) were quite similar, suggesting that both phenomena are strongly related through a cyclotron wave-particle interaction in the magnetosphere. However in the other balloon experiment, in which the X-ray and the ELF waves were observed at almost the same L value, the time variations of X-ray and ELF waves were anti-correlated. Difference in the relationship between X-ray and ELF waves in these three balloon experiments can be understood in terms of the poleward skewing of the penetrating ray path discussed in Section 2.4. When the wave-particle interaction takes place near the magnetic equatorial plane, electrons precipitate along the geomagnetic field line, whereas ELF waves traverse the field line towards higher latitudes at the level of the ionosphere. Hence the highest correlation between X-ray and ELF wave is expected when the X-ray is observed on the lower latitude side of the wave observation site as in the case of B_{15}-3N experiment.

5.3. Relationship between QP emissions and X-ray pulsations

As seen in Fig. 83, a magnetic pulsation with periods of 20–30 s occurred throughout the B_{15}-3N balloon flight on March 19, 1982. It was also found that pulsations in ELF emission intensity and X-ray count rate were associated with magnetic pulsations. A close relation between these three different pulsating phenomena is seen in an expanded plot given in Fig. 84. Note here the one-to-one correspondence between increases in ELF emission intensity at 0.8 and 1.5 kHz and X-ray enhancements. On the other hand, the correlation between ELF emission and magnetic pulsation is not so good as the correlation between ELF emission and X-ray. This ELF pulsation is called quasi-periodic (QP) emissions (*e.g.*, SATO and KOKUBUN, 1980). The one-to-one correspondence between occurrences of QP emissions and X-ray enhancement suggests that QP emissions (whistler mode waves) modulate the pitch angle diffusion rate of energetic electrons trapped in the magnetosphere through a cyclotron wave-particle interaction. Further the close correlation between QP emissions and magnetic pulsations suggests that magnetic pulsations (hydromagnetic waves) in the magnetosphere modulate the growth rate of whistler mode waves. This is theoretically predicted by CORONITI and KENNEL (1970) although clear evidence for this theory has not been found so far. The frequency-time spectrogram of such QP emissions shows rising tone characteristics.

SATO and FUKUNISHI (1981) proposed a phenomenological model to explain the

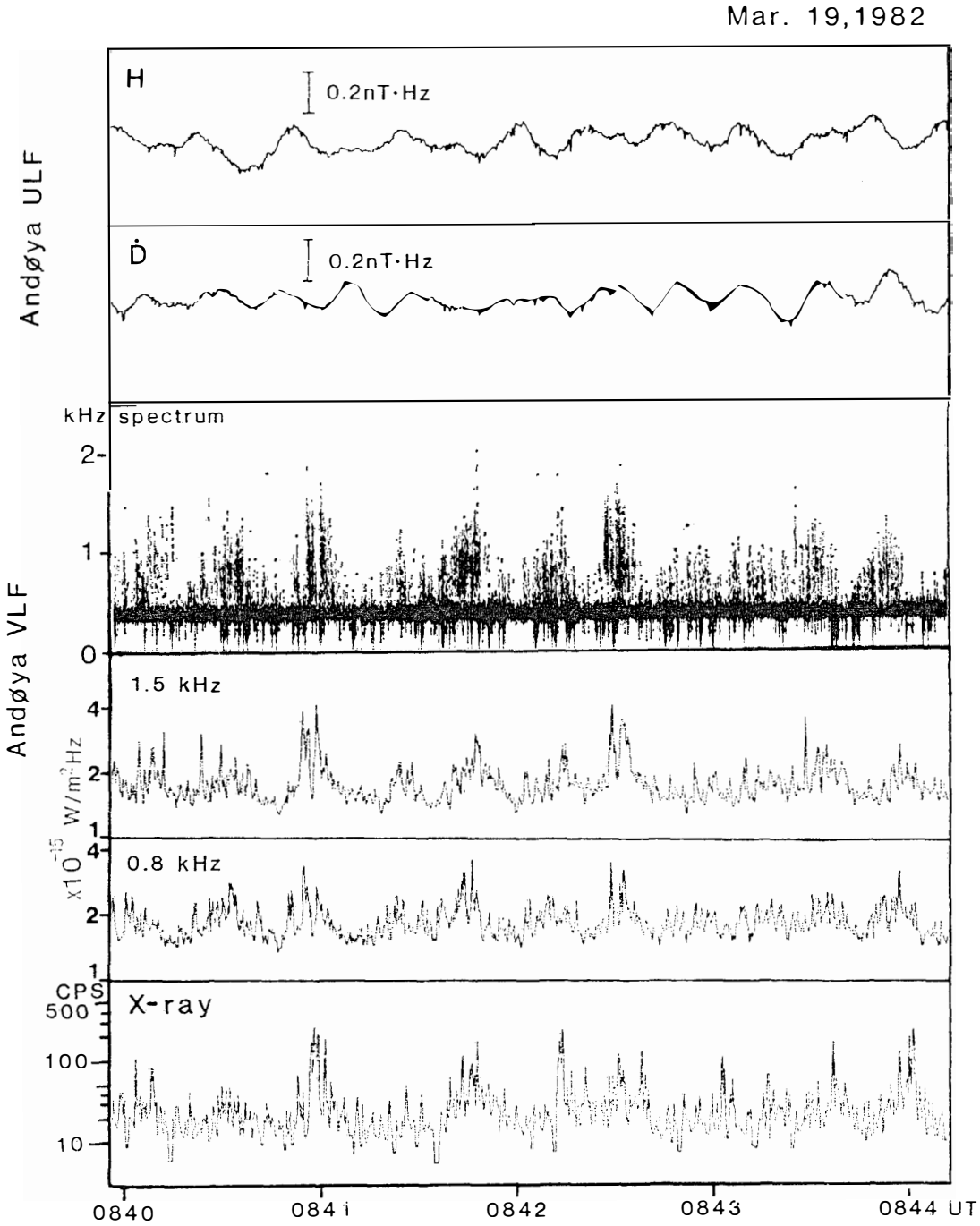

Fig. 84. Relationship between magnetic pulsation (H and D components), frequency-time spectrum of ELF emission and intensity variation at 0.8 and 1.5 kHz, and X-ray pulsation during the time interval of 0839:55–0844:15 UT. Note that the frequency-time spectrum of ELF emission shows rising tone characteristics.

rising tone type QP emissions. They assumed that compressional mode Pc 3 magnetic pulsations propagate in radial direction from the dayside magnetopause towards the earth. The growth rate of whistler mode waves is modulated by the compressional component of hydromagnetic waves through the electron cyclotron instability mechanism proposed by CORONITI and KENNEL (1970). The frequency of the maximum

growth rate is around $1/4 f_H$, where f_H is the local electron gyrofrequency in the equatorial plane (TSURUTANI and SMITH, 1977). Therefore, it is suggested that as the compressional mode waves propagate towards the earth, the generation region of whistler mode waves moves towards lower L shells with increasing emission frequency. The whistler mode waves excited in different L shells can be observed at the same station on the ground due to a spreading of ray paths during their propagation from the magnetic equatorial plane to the ground as discussed in Section 2.4. Consequently, rising-tone type QP emission is observed on the ground.

In this model, the generation region for each frequency component of rising-tone type QP emission is located in the equatorial plane in such a way that the higher frequency component is generated in the inner L shell. From the aspect of energetic electron precipitation, the precipitation observed in the inner L shell is caused by the higher frequency component of the QP emission. In order to confirm this hypothesis, we selected three frequency bands with center frequencies at 0.8, 1.5 and 2.25 kHz, and calculated the cross-correlation functions between the intensities of these frequency bands and X-ray count rates with a time window of 40 s.

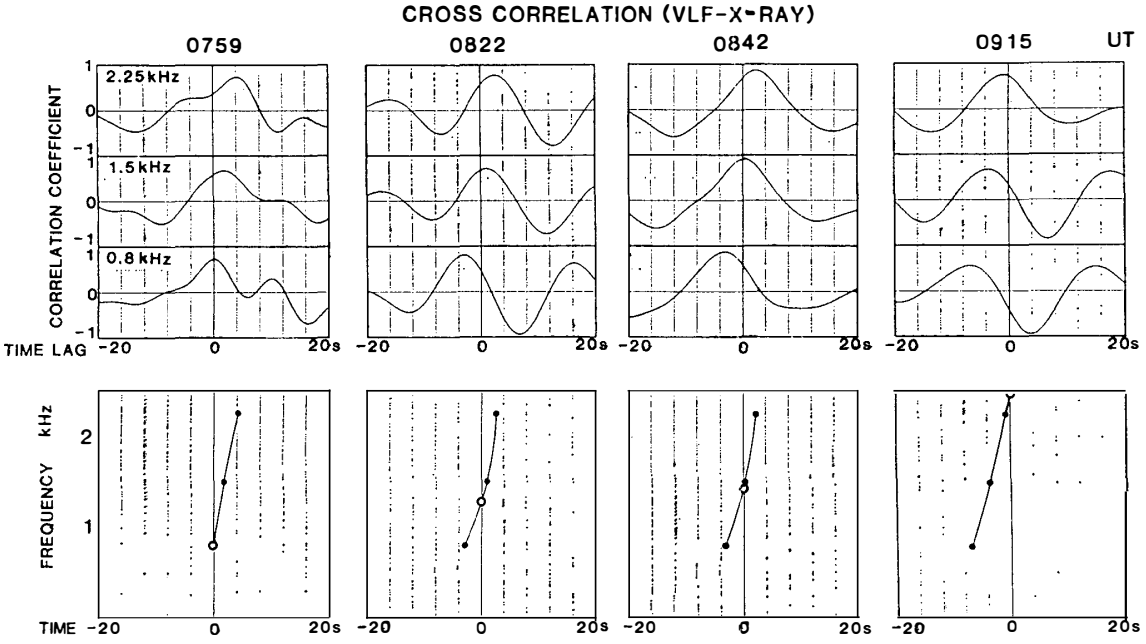

Fig. 85. Upper panels: cross-correlation function between X-ray count rate and ELF wave intensites at the frequency of 0.8, 1.5 and 2.25 kHz with the time window of 40 s for four time intervals. Lower panels: dependence of the time lag at the maximum correlation coefficient on the emission frequency. The open circles indicate "in-phase frequencies" at which the X-ray and ELF pulsations show in-phase relation. The minus sign of the time lag indicates that the ELF pulsation leads the X-ray pulsation.

Presented in Fig. 85 are examples of the cross-correlation functions calculated for four time intervals of 0759:20–0800:00, 0821:40–0822:20, 0841:40–0842:20 and 0914:40–0915:20 UT. The upper panels show the cross-correlation functions between X-ray and ELF wave intensities at the frequency bands of 0.8, 1.5 and 2.25 kHz, while the lower panels show the dependence of the time lag at the maximum correlation coefficient

on the emission frequency. The df/dt curves in the lower panel were calculated by a polynomial approximation for the three time lags at 0.8, 1.5 and 2.25 kHz. The minus sign of the time lag indicated that the ELF pulsation led the X-ray pulsation. The open circles in the lower panel indicate "in-phase frequencies" at which the X-ray and ELF pulsations show in-phase relation. It is found that the "in-phase frequencies" are 0.8, 1.3, 1.9 and 2.5 kHz for the four time intervals, respectively.

Figure 86 shows a temporal sequence of the relationship between the time lag at the maximum correlation coefficient and the emission frequency (df/dt curves) and the "in-phase frequencies" (open circles) during 0758–0917 UT. The notation is the same as given in the lower panels of Fig. 85. Note that two kinds of time scales are used

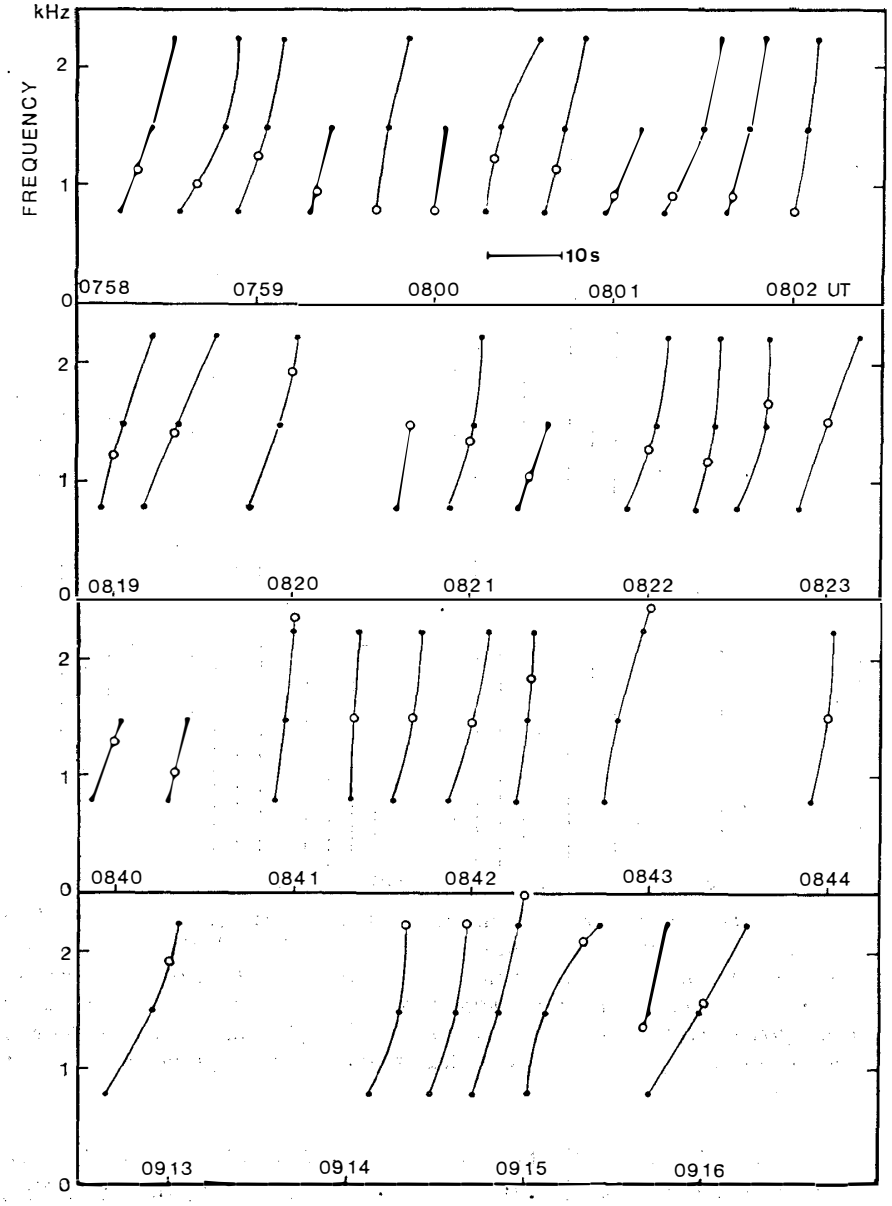

Fig. 86. Relationship between the time lag at the maximum correlation coefficient and the emission frequency (df/dt curves) and the "in-phase frequencies" (open circles) during 0758–0917 UT. The notation is the same as given in the lower panel of Fig. 85.

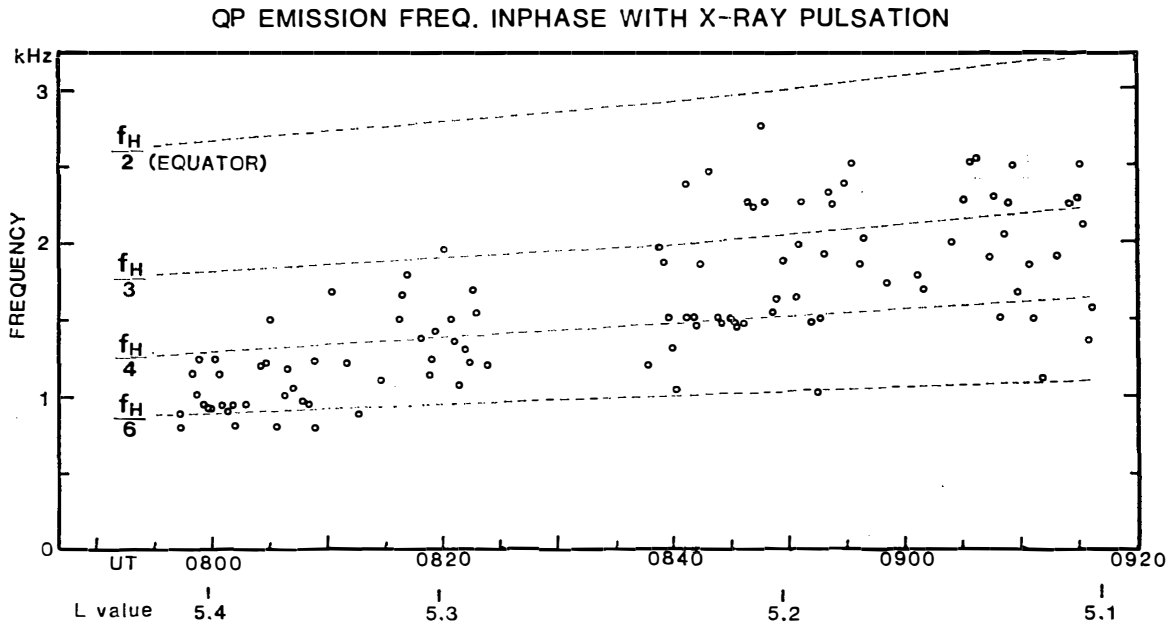

Fig. 87. Variation of "in-phase frequency" as a function of the balloon flight time. The balloon moved towards lower latitudes from $L=5.4$ at 0800 UT to $L=5.1$ at 0915 UT. The broken lines show fractional electron gyro-frequencies at the equatorial plane in the magnetosphere.

in the figure. Each df/dt curve follows the time scale indicated by a horizontal bar of 10 s in the top panel, whereas the time of appearance of each emission is shown by the universal time at the bottom of each panel. Only those plots of correlation coefficients above 0.5 are shown in the figure. Apparently there is a tendency that the in-phase frequencies marked by open circles increase with the flight time of the balloon. This tendency is further clearly demonstrated in Fig. 87, where the in-phase frequencies are plotted as a function of the flight time. The L values of the balloon position is also indicated on the abscissa. The balloon moved towards lower latitudes from $L=5.4$ at 0800 UT to $L=5.1$ at 0915 UT. The broken lines in the figure show the fractional electron gyrofrequencies at the geomagnetic equator. According to SATO and FUKUNISHI's model, the in-phase frequency is expected to increase when observed at lower L-value. Hence the variation of in-phase frequencies illustrated in Fig. 87 is considered not to be the temporal variation, but the spatial variation, or L dependence.

The balloon experiment further showed that the L dependence expected from the in-phase relation is larger than that expected from the L dependence of the equatorial gyrofrequency. The ratio of the emission frequency to the equatorial gyrofrequency increased from 1/6 at $L=5.4$ to 1/3 at $L=5.0$. It is likely that such an increase is caused by a change of the distribution function of trapped high energy electrons. If the first and second adiabatic invariants for high-energy electrons are conserved during their convecting motion to smaller L shells, both a hardening of the energy spectrum and an increase in pitch angle anisotropy are expected with decreasing L (*e.g.*, ASHOUR-ABDALLA and COWLEY, 1974). The effect of the hardening on the frequency of ELF-VLF emissions is discussed in the following. If we assume whistler mode waves to propagate parallel to the ambient magnetic field, the resonance condition of cyclotron

interaction is given as follows:

$$E_{res} = (mc^2/2)(f_H - f)^3/ff^2_p$$
$$= (mc^2/2)(1 - f/f_H)^3/(f/f_H)f^2_H/f^2_p \ , \qquad (34)$$

where E_{res} is the energy of the resonant electrons, m is electron mass, c is the light velocity, f_H, f_p and f are electron gyrofrequency, electron plasma frequency and whistler mode wave frequency, respectively. The magnetic field in the magnetosphere of $L=6$ is well approximated by a dipole magnetic field. The electron density distribution outside the plasmasphere usually follows L^{-4} relation (*e.g.*, ANGERAMI and CARPENTER, 1966). Therefore, L dependences of f_H and f^2_p are given as L^{-3} and L^{-4}, respectively. According to Ashour-Abdalla's calculation, the L dependence of electron energy increase associated with inward convection has been estimated to be L^{-2} and L^{-3} for 0° and 90° pitch angle electrons, respectively. By using the relation (34), it is found that the ratio f/f_H is independent on L for the energy increase of 0° pitch angle electrons, while the ratio decreases gradually with decreasing L for the energy increase of larger pitch angle electrons. In this situation the predicted increase of the ratio f/f_H from 1/6 at $L=5.4$ to 1/3 at $L=5.0$ may be attributed to an increase of pitch angle anisotropy with decreasing L, as suggested by ASHOUR-ABDALLA and COWLEY (1974). It is also inferred that precipitating electrons with energies outside the range of the detector contribute to the increase in the emission frequency. However, we have no information

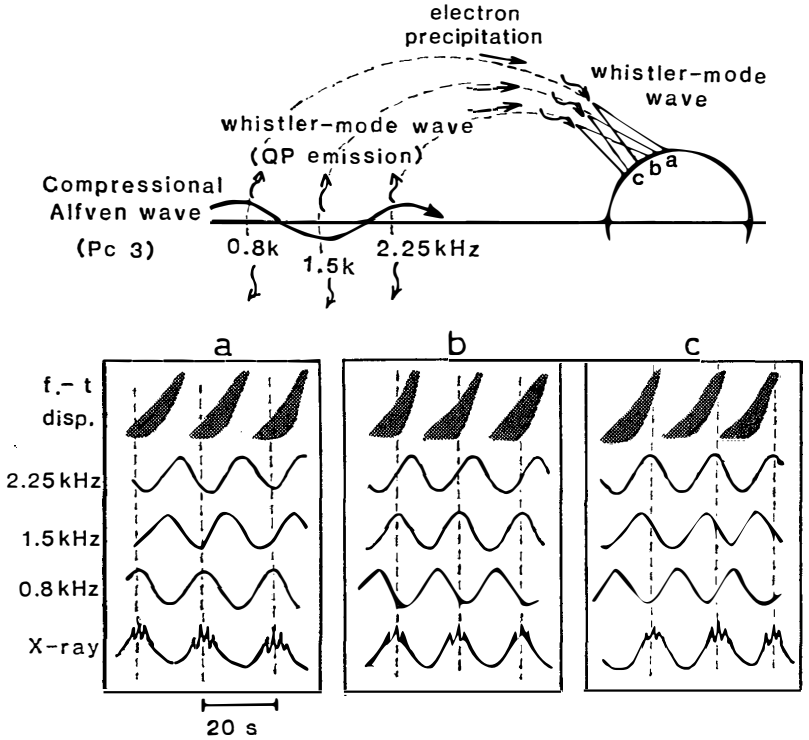

Fig. 88. Schematic illustration of the relationship between compressional mode Pc 3 magnetic pulsation, QP emission and associated electron precipitation. The lower three panels show the phase relation between X-ray pulsation observed on the balloon and QP emissions observed at the points a, b and c on the ground.

on precipitating electrons outside the 20–100 keV range since the X-ray detector with a single energy channel was used in the present experiment. Therefore, it is difficult to discuss on this matter in more detail.

Figure 88 illustrates schematically the relation between compressional Pc 3 magnetic pulsation, QP emission and associated electron precipitation. The lower three panels show frequency-time display of QP emission and the phase relation between X-ray count rate and QP emission intensity at 0.8, 1.5 and 2.25 kHz observed at the points a, b and c on the ground. It is assumed that QP emissions (whistler mode waves) modulate the pitch angle diffusion rate of trapped electrons into loss cones, and precipitating electrons are observed as X-ray pulsations at the foot of the geomagnetic field line. Note that whistler mode waves propagating towards the northern hemisphere interact with electrons moving towards the southern hemisphere, since the cyclotron wave-particle interaction is of a counter-streaming type. Therefore, it is assumed in this model that whistler mode waves propagate towards the both hemispheres. The difference in the traveling time of whistler mode waves and high energy electrons is omitted since it is estimated to be less than 1 s.

From the present observation, it is concluded that QP emissions were generated at least within L-value range of 5.0 to 5.4, which was covered by the balloon flight. The above L-values were smaller than that of ELF wave observation site of $L=6.1$. This configuration is understood well in terms of the poleward skewing characteristics of the "penetrating ray paths" discussed in Section 2.4. It is expected further that the precipitation region moves periodically from high to low latitudes as being synchronized to the occurrence of QP emissions. The speed of the equatorward motion is given as 50 km/s by the projection of Alfvén velocity in the equatorial plane onto the polar ionosphere. PARKS (1967) observed the motion of X-ray microburst region with 10–100 km/s. However, the observational results are not conclusive at present, and it is desirable in the future to observe X-ray pulsations with multiple balloons.

5.4. Relationship between chorus bursts and X-ray fast pulsations

Chorus and X-ray fast variation appear as groups of bursts, in which the duration of each element is a few tenth of a second, and repetition interval of the group several seconds. For the correlation study of both data in this time scale, it is important to include the effect of the propagation time difference between waves and electrons from the equatorial region to the ground, because above time difference is estimated to be 1 s and comparable to the time scale of these phenomena.

In Section 5.4.1, high time resolution (0.1 s) balloon X-ray data observed in northern hemisphere was compared with VLF waves observed on the ground near the balloon position and near the geomagnetically conjugate point in the opposite hemisphere. Above-mentioned propagation time difference was found and it was understood in terms of the counter-streaming type wave particle interaction and echoing of VLF waves in the magnetosphere.

In Section 5.4.2, balloon X-ray observed over Iceland was compared with ground VLF wave data observed at three stations in Iceland. Due to low time resolution of X-ray data (2 s), it was difficult to find out the above-mentioned propagation time difference. However, cross correlation study between X-ray and VLF waves showed

clear one-to-one correspondence between both bursts, and this feature is analyzed in terms of ducted propagation of VLF waves.

5.4.1. B_{15}-3N experiment

During the flight of B_{15}-3N balloon, X-ray microbursts with 0.5–2 s spacing were often observed. The VLF receivers at Andøya in northern Norway and at Syowa Station in Antarctica observed bursts of ELF waves (polar chorus) with similar time scales.

Figure 89 shows the relationship between these two phenomena observed at 0758–0759 UT on March 19, 1982. The upper panel shows frequency-time spectrograms of ELF waves observed at Andøya and Syowa, while the lower panel shows the counting rate of X-ray in the energy above 20 keV, ELF emission intensities at 1.25 kHz observed at Andøya and Syowa, respectively. It was found that both X-ray and ELF bursts appeared periodically with an interval of 4 s. It was also found that the X-ray observed in the northern hemisphere, appeared simultaneously with the ELF in the opposite hemisphere (Syowa), whereas it is out of phase with the ELF in the same hemisphere (Andøya). This feature can be more clearly recognized in Fig. 90, in which the top panel shows time profiles of balloon X-ray, ELF intensities at Andøya and Syowa Station during 0758:10–0758:30 UT, and the lower three panels show cross-correlation

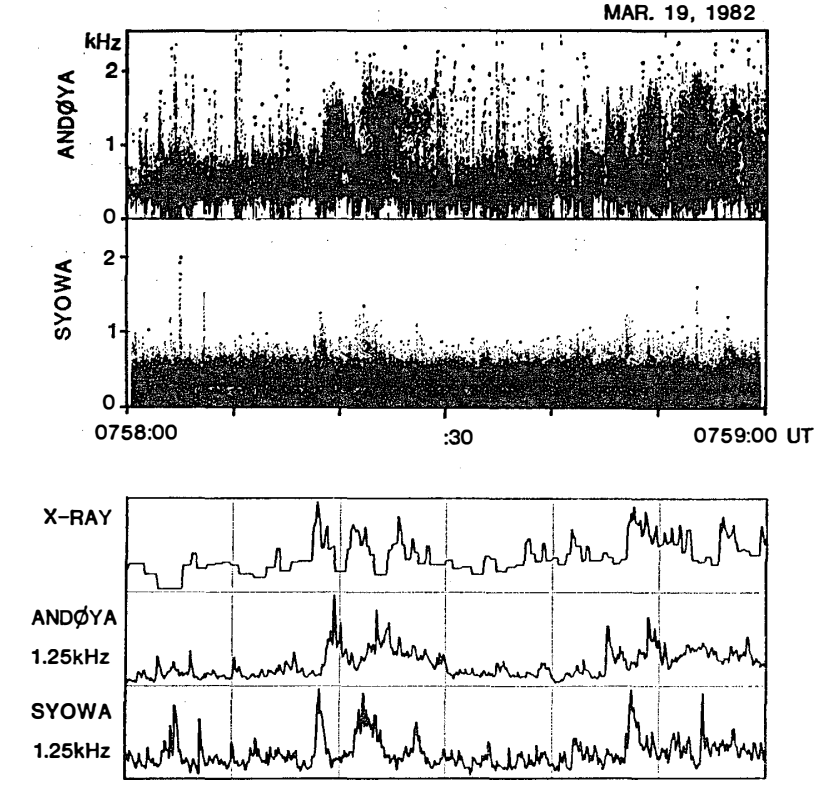

Fig. 89. A comparison of polar chorus emissions and X-ray micro-bursts during 0758–0759 UT on March 19, 1982. The upper panel shows frequency-time spectrograms of ELF waves observed at Andøya and Syowa, and the lower panel shows the counting rate of X-ray in the energy range above 20 keV, ELF emission intensities at 1.25 kHz observed in Andøya and Syowa, respectively.

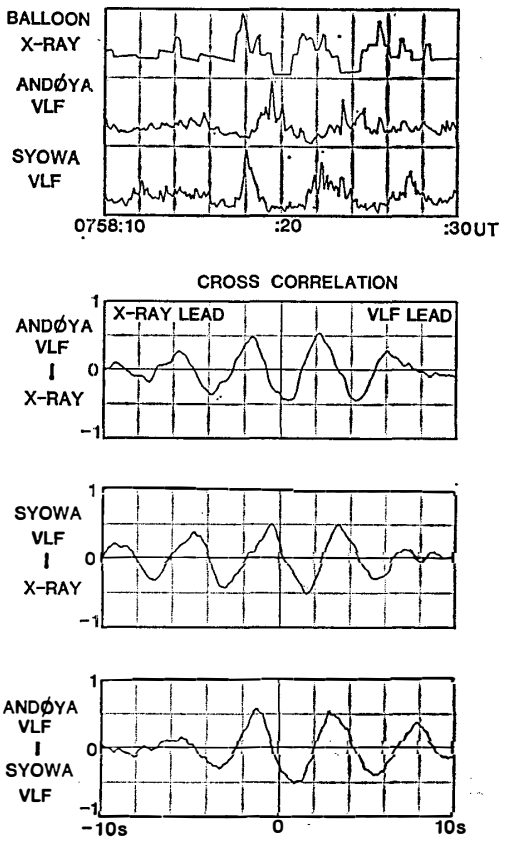

Fig. 90. Top panel shows time profiles of X-ray micro-bursts, ELF emissions observed at Andøya and Syowa, respectively, and the lower panels show cross-correlation functions between Andøya ELF and X-ray, Syowa ELF and X-ray, Andøya ELF and Syowa ELF, respectively.

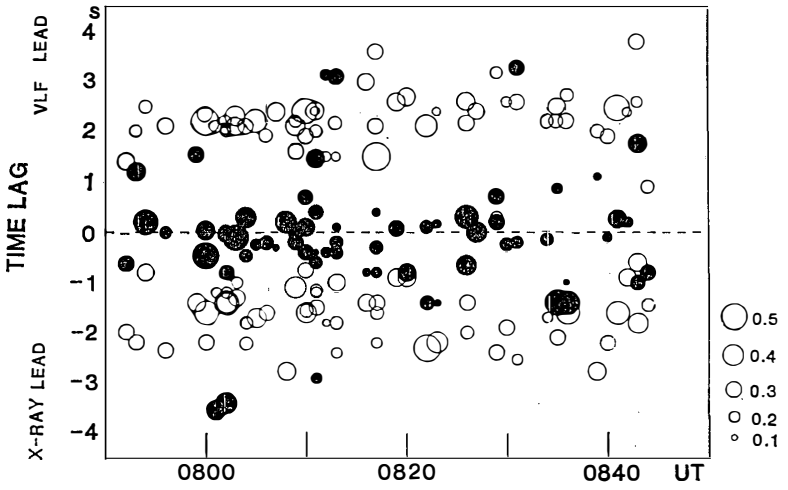

Fig. 91. A summary of the cross-correlation between X-ray micro-bursts and ELF bursts. Solid and open circles represent the close relationship between Syowa ELF and X-ray, and Andøya ELF and X-ray, respectively. Size of each circle indicates the peak value of the cross correlation function as shown at the right corner of the figure.

functions of Andøya ELF: X-ray, Syowa ELF: X-ray, and Andøya ELF: Syowa ELF, calculated for the same time. Such a close relationship between each element of X-ray and ELF bursts was sometimes found in this balloon flight.

Figure 91 summarizes the cross-correlation between them, where solid circles are the correlation between Syowa ELF bursts and X-ray, whereas open circles between

Andøya ELF bursts and X-ray. The size of each circle indicates the peak value of the cross-correlation function between X-ray and ELF. It is evident that Syowa ELF bursts and the X-ray generally appeared simultaneously, whereas Andøya ELF bursts led or lagged the X-ray by about 2 s. This feature is qualitatively understood in terms of the counter-streaming type wave-particle interaction, *i.e.* the electrons and waves involved in this process go to the opposite hemisphere with an echoing of wave packets between two hemispheres.

The occurrence rate of the close relationship between X-ray and ELF bursts with the correlation coefficient above 0.4 is only 6% of the whole interval of 0750–0845 UT. This low occurrence rate of close relationship is due to the fact that only a fraction of ELF emissions observed at Syowa Station and Andøya is related to the X-ray observed by the balloon X-ray. Most of the ELF emissions observed were caused by the precipitation outside the field of view of the X-ray detector on board the balloon.

5.4.2. AZCO EXW1 experiment

In AZCO EXW1 balloon experiment, X-ray micro-bursts were observed during 06–09 UT on July 6, 1985. VLF receivers at Husafell, Tjörnes and Isafjördur in Iceland observed bursts of ELF waves at the same interval. Figure 92 shows time profiles of X-ray count rate (top panel) and ELF wave intensity at Husafell (middle panel) for the above period. The bottom panel shows a gray scale display of the cross correlation function between X-ray and ELF for the same period with a time window of 2 min. In this panel, the ordinate shows a time lag between X-ray and ELF waves. A positive time lag indicates that X-ray lead ELF waves. A dark color in the gray

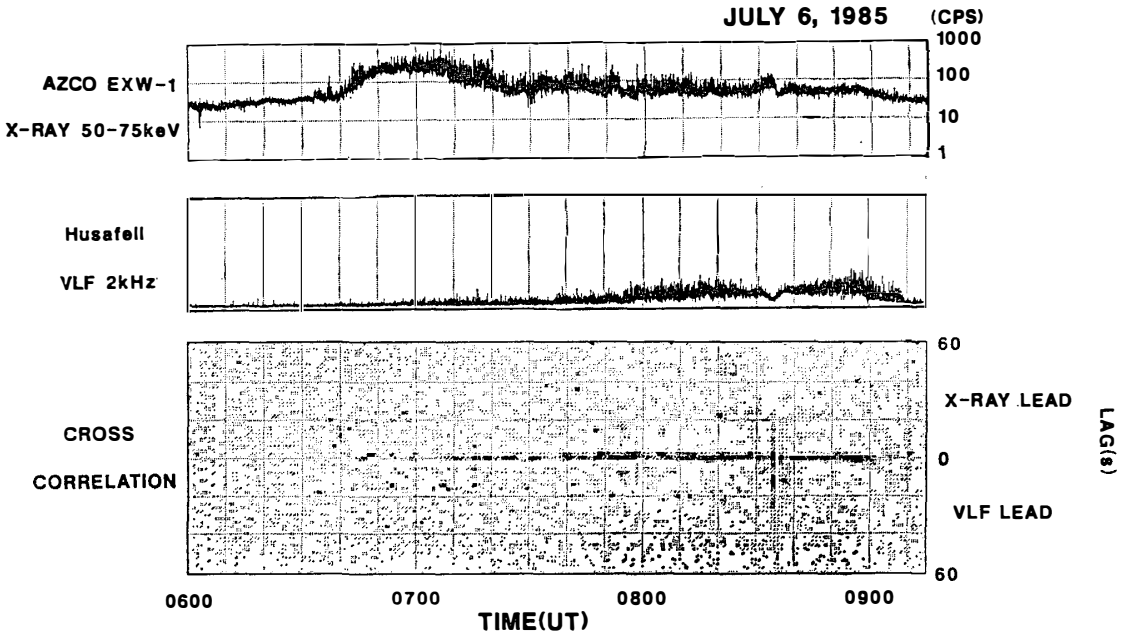

Fig. 92. Time profiles of X-ray microbursts count rate observed by AZCO EXW1 balloon (top panel) and ELF wave intensity observed at Husafell in Iceland (middle panel) during 0600–0915 UT on July 6, 1985. Bottom panel shows a gray scale display of the cross-correlation function between X-ray and ELF waves with a time window of 2 min for the above period. A dark color in the gray scale display represents a large positive value of the correlation.

scale display represents a large positive value of the cross-correlation coefficient. A noticeable and of high cross-correlation coefficient is found at the time lag equals to zero during 0705–0902 UT, suggesting that X-ray micro-bursts observed by the balloon were closely related to the ELF bursts observed on the ground. Due to low time resolution of X-ray and VLF wave data (2 s), the propagation time difference of 1 to 2 s between VLF waves and electrons discussed in Section 5.4.1 could not be detected in the present analysis.

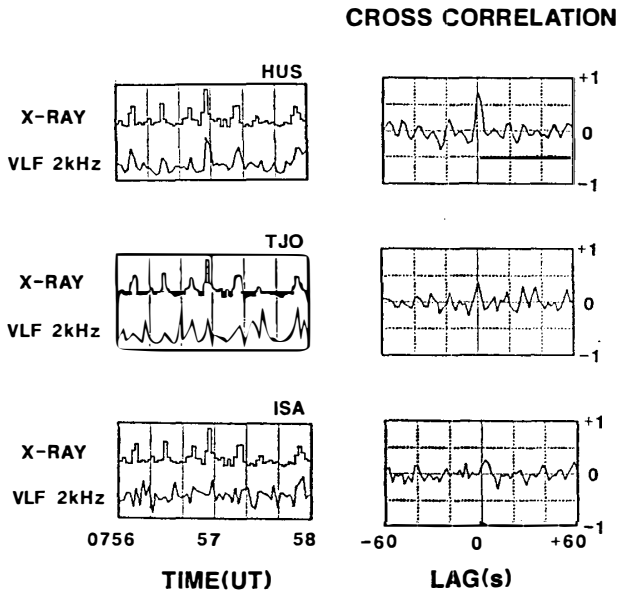

Fig. 93. Left panels: expanded records of the X-ray micro-bursts and the ELF bursts observed at Husafell (HUS), Tjörnes (TJO) and Isafjördur (ISA) at 0756–0758 UT on July 6, 1985. Right panels: cross-correlation functions between the X-ray and the ELF bursts for the same time interval.

Presented in the left panels of Fig. 93 are expanded records of the X-ray micro-bursts and the ELF bursts observed at three stations in Iceland, *i.e.* Husafell (HUS), Tjörnes (TJO) and Isafjördur (ISA) at 0756–0758 UT on July 6, 1985. The right panels show cross-correlation functions between the X-ray and the ELF bursts for the same time interval. It is evident that the cross-correlation function shows a narrow peak at the time lag near zero. The sharp correlation peak is due to an impulse-like feature of the bursts.

The cross-correlation functions for the three stations were successively calculated with a time window of 2 min from 0600 to 0915 UT, and they are shown as gray scale display in Fig. 94 in a way similar to the bottom panel of Fig. 92. Noticeable bands of high cross-correlation coefficients are found at the time lag of zero at each station, though the starting time of these bands is different at these three stations. Taking into account the distance between the balloon and the observation sites for ELF waves (200 km for Husafell, 270 km for Tjörnes and 370 km for Isafjördur), the observed feature suggests that the area of ELF waves having close relationship to the X-ray

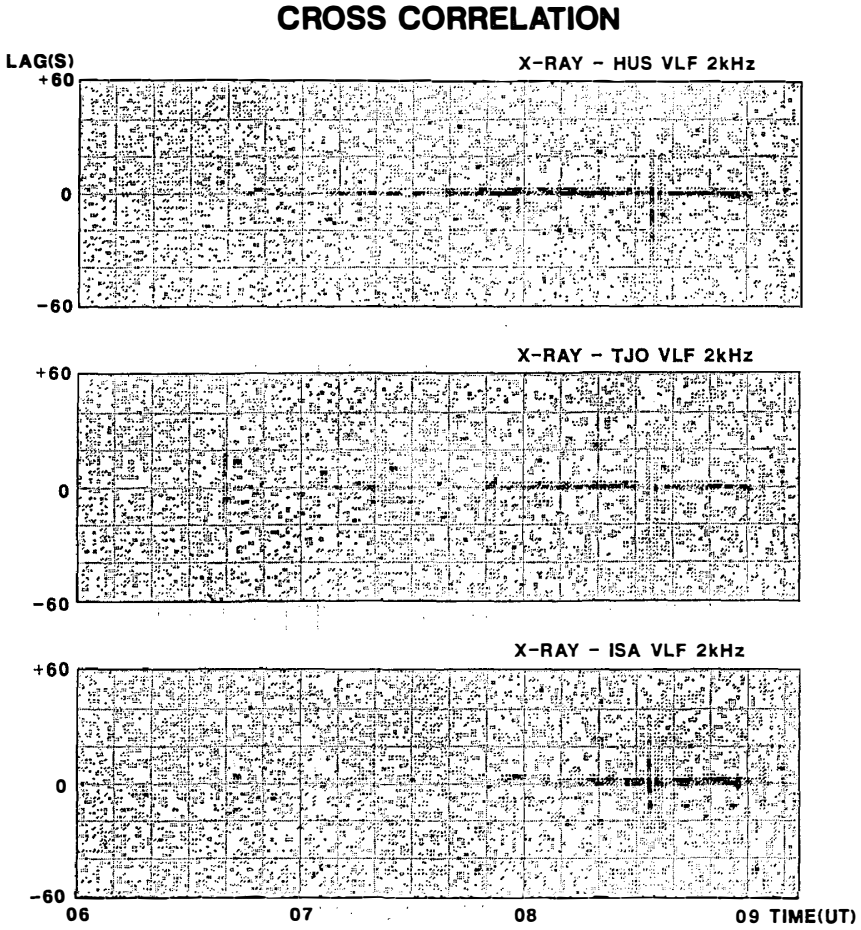

Fig. 94. Gray scale displays of the cross-correlation function between X-ray and ELF bursts observed at Husafell (top panel), Tjörnes (middle panel) and Isafjördur (bottom panel) in the same format as the bottom panel of Fig. 92.

extended with time from the nearest station to the balloon (Husafell) to the farthest station (Isafjördur).

In this event, the occurrence rate of close relationship between X-ray and ELF bursts with the correlation coefficient above 0.4 is 70% for Husafell in the period of 0710–0900 UT. This occurrence rate is much higher than that observed in B_{15}-3N experiment. The high occurrence rate of close relationship between X-ray and ELF bursts is explainable if ELF waves propagated in a duct formed along the geomagnetic field lines. In this mode of propagation, both precipitating electrons and ELF waves move along the same field line. Hence a close relationship between X-ray and ELF waves is expected at the foot point of the above field line.

An ELF duct terminates at an altitude where the plasma density enhancement of the duct is dissolved. The ELF wave trapped in the duct is released at the duct exit, and propagates downwards in nonducted mode. The wave spreads widely at the ionospheric level, and the width of the extent is dependent on the altitude of the duct exit as discussed in Section 4.4. BERNHARDT and PARK (1977) made numerical simulations of ionosphere and protonosphere in order to investigate diurnal variation and

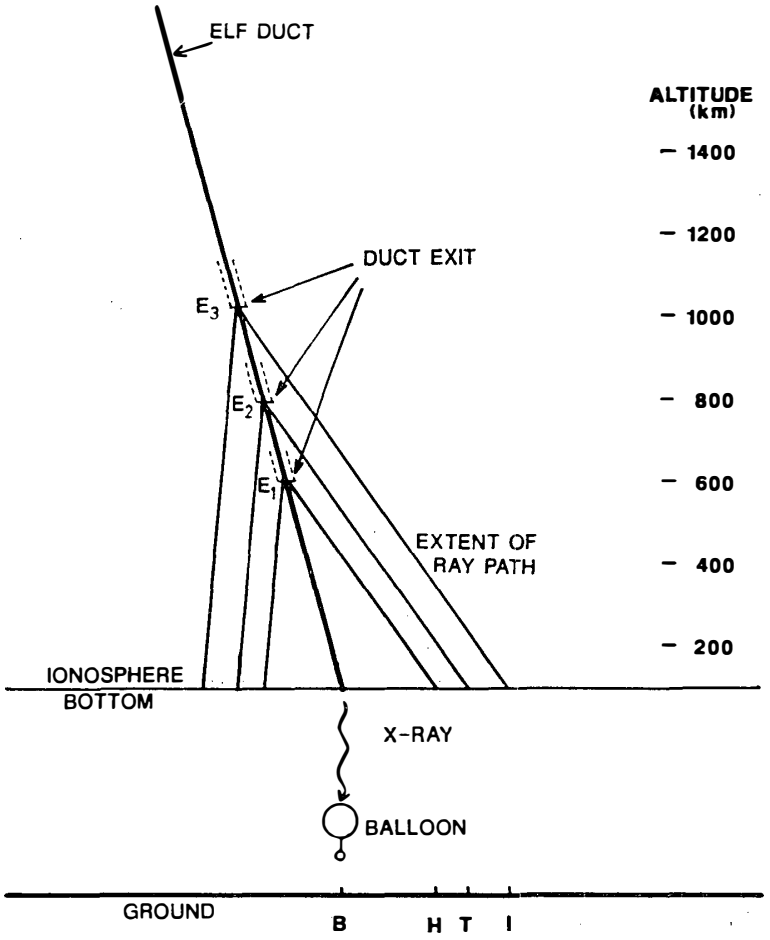

Fig. 95. A model of ELF wave propagation in AZCO EXW1 balloon experiment. The letters B, H, T and I stand for sub-balloon point, Husafell, Tjörnes and Isafjördur. The altitude of the duct exit increased with time from the point E_1 to E_3, and the spatial extent of ELF wave arrival at the ionospheric level increased from H to I.

decay of field-aligned plasma density enhancements capable of ducting VLF waves. According to their model, the altitude of the duct exit is 1100 km in the nighttime and 2000 km in the daytime during summer. There is a rapid upward shifting of duct exit in 04–06 LT due to an upward flow of thermal plasma from the ionosphere into the protonosphere. When such an upward shift of the duct exit occurs, the spatial extent of ducted ELF wave arrival on the ground also increases. The whole story is modelled in Fig. 95. The characteristics of the cross-correlation between X-ray micro-bursts and ELF bursts shown in Fig. 94 can be explained with this model. The dutc exit was assumed at the point E_1 at 0710 UT (0510 LT). At this time ELF waves involved in the wave-particle process could be observed only at Husafell (H). At 0750 UT (0550 LT), the duct exit was assumed at E_2, and the ELF waves could spread as far as Tjörnes (T). At 0810 (0610 LT), the duct exit was assumed at E_3, and the ELF waves reached the furthest station, Isafjördur (I). It is true that the balloon

moved as much as 40 km in the time interval of 0710–0810 UT as shown in Fig. 79. However, above distance is much shorter than those from the balloon to the three stations, *i.e.*, 200 km to Husafell, 270 km to Tjörnes, and 370 km to Isafjördue. So, the effect of the balloon motion was considered to be small.

5.5. Summary

Bremsstrahlung X-rays observed by balloons in the daytime auroral zone were compared with ELF waves simultaneously observed on the ground from a viewpoint that the X-rays are originated from high energy electron precipitations through a wave-particle interaction with whistler mode ELF waves in the magnetosphere. As the precipitating electrons strictly follow the magnetic field line, the feature of the precipitation observed at the ionosphere level gives useful information on the source location of ELF waves involved in the wave-particle process in the magnetic equatorial region. The temporal variations of the precipitation comprise characteristic time scales of slow variations (10 min–1 h), pulsations (10 s–10 min) and micro-bursts (0.1 s–10 s).

In reference to slow variations, a general anti-correlation was found between ELF waves and X-ray intensity variations when they were observed at almost the same L shell as in the case of B_5-28 experiment. This opposes an expectation from a gyro-resonance wave-particle interaction. However, this feature is understandable when taking account of an increased ionospheric opacity at the time of increased electron precipitation. However, a good correlation was found between X-ray and ELF wave intensity when X-ray was observed on the lower latitude side of the ELF observation site as in the case of B_{15}-3N experiment. This feature is explainable by the poleward skewing characteristics of the "penetrating ray path" discussed in Section 2.4. That is, when a wave-particle interaction takes place in the magnetic equatorial region, electrons precipitate along the geomagnetic field line, whereas the ELF waves follow the penetrating ray paths, which traverse the field line towards higher latitudes. Hence the highest correlation is expected when the X-ray is observed on the lower latitude side of the wave observation site.

In Pc 3 pulsation time-scale range, an in-phase relationship was discovered between rising-tone type QP emissions observed at Andøya (L=6.1) and X-ray pulsations observed by B_{15}-3N balloon at L=5.1–5.4. It was found that a higher frequency component of the emission was in-phase with the X-ray when observed at an inner L shell. This suggests that the generation region of the each frequency component of rising-tone type QP emissions is located in the equatorial plane in such a way that the higher frequency component of the emission is generated in an inner L shell. This observational result also supports SATO and FUKUNISHI's model of rising-tone type QP emission generation, in which the rising-tone emission is originated from a drifting motion of the wave generation region towards the inner L shell due to a propagation of compressional mode HM waves from the dayside magnetopause towards the earth.

In regard to micro-bursts (0.1 s–10 s), one-to-one correspondence was sometimes obtained between X-ray and ELF bursts. The occurrence rate of the cross-correlation coefficient above 0.4 is only 6% for B_{15}-3N balloon experiment, in which the X-ray was observed at L=5.3, 200 km southward from the observation site of ELF waves

at $L=6.1$. The rare occurrence rate of close relationship suggests that a large portion of ELF bursts observed at Andøya were generated by the electrons precipitated outside the field of view of the balloon X-ray instrument. Time lag between the occurrences of X-ray and ELF bursts is distributed around zero when they were observed in the opposite hemisphere, and around 2 s when observed in the same hemisphere. This feature is qualitatively understood in terms of the counter-streaming type wave-particle interaction, and the bouncing of wave packet in the magnetosphere.

In AZCO EXW1 experiment, much higher occurrence rate amounting even to 70% was obtained between balloon X-ray and ELF bursts observed at Husafell, located at about 200 km north of the balloon position. The frequent occurrence of the close relationship between X-ray and ELF bursts suggests that ELF waves were propagated in ducted mode, in which both the waves and electrons moved along the same field line, and a high cross-correlation coefficient is expected between them at the foot of the field line. Close relationship between X-ray and ELF bursts were also found at other two observation sites for ELF waves in Iceland, *i.e.* Tjörnes, 270 km geomagnetically NE of the balloon position, and Isafjördur, 370 km geomagnetically NNW of the balloon position. At these three stations, however, the starting time of the close relationship was delayed according to the distance from the X-ray observation point. This time delay in the high cross-correlation at these three stations is explainable by an upward shifting of the ELF duct exit with time due to an upward flux of ionospheric plasma in the morning hours, and the resultant extending of ELF wave arrival area on the ground.

6. Concluding Remarks

In this paper, propagation characteristics of ELF emission in high latitude magnetosphere are studied by 2-dimensional ray tracing, and the results are confirmed by ELF wave observations onboard ISIS satellites and on the ground at Syowa Station, Antarctica.

In Chapter 2, propagation characteristics of nonducted ray paths starting from the magnetic equatorial plane are analyzed. Most of ELF waves undergo LHR reflection before they reach usual polar orbiting satellite altitude of several thousands of kilometers. Only a part of nonducted ray paths are accessible to low altitudes, and they are called "penetrating ray paths". It is found that the wave normal angles of penetrating ray paths on the equatorial plane are confined within a narrow range of angle directing considerably inward (towards the earth). This range of equatorial wave normal angle is called "ψ_i window".

For most of the penetrating ray paths, wave normals turn away from the earth at high altitude mainly due to the effect of the magnetic field line curvature. On the other hand, a large vertical electron density gradient at low altitude gives as opposite effect on wave normal variation. The above two effects balance at an altitude of about 3000 km, where the wave normal angles show maximum deviation from $\boldsymbol{B}_0$. This point on a ray path is called "turning point" of wave normal angle. The wave normal angle of penetrating ray paths converges towards 90° with respect to $\boldsymbol{B}_0$ at the turning point. It becomes smaller with decreasing altitude, and becomes 45° at ISIS-2 satellite altitude of 1450 km. The penetrating ray paths show "poleward skewing" in low altitudes, *i.e.* the ray paths shift to higher latitude when the waves propagate downward.

In Chapter 3, wave normal direction of penetrating ray paths calculated in Chapter 2 is experimentally confirmed by ISIS satellite ELF observations.

First, wave normal direction of ELF hiss is obtained from the spin-modulated characteristics of received signal intensity. Obtained wave normal angles are almost 90° at an altitude of 3000 km and 50°–70° at 1450 km, which agree well with the results of ray tracing in Chapter 2.

Secondly, wave normal direction of ELF hiss is estimated from the attenuation at the multi-ion cutoff observed in the power spectrum of ELF hiss. From the full-wave calculation of multi-ion cutoff, the wave normal angle of ELF hiss at ISIS satellite altitude must be greater than 40° with respect to $\boldsymbol{B}_0$ in order to explain the observed value of attenuation. This also agrees with the results of ray tracing in Chapter 2.

This chapter deals with seasonal variation of ELF hiss intensity obtained at ISIS satellite altitude and on the ground. It is found that the intensity in summer is stronger than that in winter by 4 dB for both satellite altitude and on the ground. This means that the seasonal variation must be originated mainly above the satellite altitude. A tracing of penetrating ray path revealed that the ψ_1 window of the summer hemisphere is considerably wider than that of the winter hemisphere. This suggests that more wave energy is transferred from the equatorial plane to the satellite altitude in the summer hemisphere, and this is a possible cause of stronger emission intensity in the summer hemisphere.

In Chapter 4, some important features of ducted propagation outside the plasmapause are obtained from the analysis of periodic emissions observed at Syowa Station, Andøya in Norway, and on ISIS-2 satellite. From one-month continuous observation of ELF emission at Syowa and Andøya in March 1982, it was found that the occurrence rate of periodic emissions was 6% for this period. This means that the occurrence rate of ducted propagation near $L=6$ is relatively low and the majority of ELF emissions observed on the ground is thought to be propagated in nonducted mode. This inference is consistent with the observed fact of large wave normal angles of ELF hiss at ISIS satellite altitude described in Chapter 3, which is only explainable by nonducted propagation.

Multi-static ground based observations and ISIS satellite observation of periodic emissions revealed that the spatial extent of the emission was as wide as about 2000 km at the ionosphere level and on the ground. This wide extent can be explained if the duct is terminated at a considerably high altitude. Ray tracing from the duct exit to the ionosphere revealed that the duct exit altitude must be located at an altitude of 6000–7500 km in order to explain the observed extent of the emission.

In Chapter 5, Bremsstrahlung X-rays observed by balloons in the daytime auroral zone are compared with ELF emissions simultaneously observed on the ground, from a viewpoint that the X-rays are originated from high energy electron precipitations caused by wave-particle interaction with ELF emissions in the magnetosphere. As the precipitating electrons strictly follow the magnetic field line, the location of precipitation at the ionosphere level gives useful information on the source location of ELF waves involved in the wave-particle interaction. The electron precipitation shows temporal variations with characteristic time scales of 10 min–1 h (slow variation), 10 s–10 min (pulsations) and 0.1 s–10 s (micro-bursts).

With reference to slow variations, a good correlation is found between X-ray and ELF wave intensity when X-ray is observed on the lower latitude side of the ELF observation site. This supports the "poleward skewing" of penetrating ray paths obtained from the ray tracing in Chapter 2.

In Pc 3 pulsation time-scale range, an in-phase relationship is found between rising-tone type QP emissions observed at $L=6.1$ and X-ray pulsations observed at $L=5.1$–5.4. It was found that a higher frequency component of the emission is in-phase with the X-ray when observed at an inner L shell. This suggests that the generation region of rising-tone type QP emissions is located in the equatorial plane in such a way that the higher frequency component is generated in an inner L shell.

In regard to micro-bursts, one-to-one correspondence is sometimes obtained be-

tween X-ray and ELF bursts. The occurrence rate of the cross-correlation coefficient above 0.4 is only 6% in a balloon experiment in which X-ray was observed at $L=5.3$ and ELF was observed at $L=6.1$, which is 200 km north of the balloon. The rare occurrence rate of close relationship between X-ray and ELF bursts suggests nonducted propagation of ELF bursts, in which arriving position of the wave deviates a great deal from that of associated precipitation. Time lag between the occurrences of X-ray and ELF bursts is distributed around zero when they were observed in the opposite hemisphere, and around 2 s when observed in the same hemisphere. This feature is qualitatively understood in terms of the counter-streaming type wave-particle interaction, and the bouncing of wave packet in the magnetosphere.

In another balloon experiment, much higher occurrence rate amounting even to 70% was obtained between X-ray micro-bursts observed at $L=5.5$ and ELF bursts observed at $L=6.1$, which was 200 km north of the balloon. The frequent occurrence of close relationship between X-ray and ELF bursts suggests that ELF bursts propagate in ducted mode, in which both the waves and electrons move along the same field line. It was also found that, for three ground-based VLF observation sites, the starting time of the close relationship was delayed according to the distance from the balloon. This feature is explainable by an upward shifting of the ELF duct exit with local time due to an upward flow of ionospheric plasma in the morning hours, and the resultant extending of ELF wave arrival area on the ground.

Acknowledgments

The author wishes to express his sincere thanks to Prof. I. KIMURA of Kyoto University for his valuable suggestions, guidance and encouragement throughout the present work, and careful reading of the manuscript. The author also wishes to express his deep appreciation to Prof. T. HIRASAWA of National Institute of Polar Research for his helpful advice and continuous encouragement.

The author also wishes to express his sincere thanks to Prof. M. EJIRI of National Institute of Polar Research for his constructive comments on the manuscript and helpful advice on the present work. The author also wishes to express his heartfelt appreciation to Prof. N. SATO of the same institute for his valuable discussions, careful reading of the manuscript and continuous encouragement.

The author is greatly indebted to Prof. H. FUKUNISHI of Tohoku University for his valuable suggestions, and in particular, for his guidance in the study of X-ray pulsations in Section 5.3. The author is deeply grateful to Prof. K. HASHIMOTO of Tokyo Denki University for his guidance in the ray tracing in Chapter 2. Sincere thanks are also due to Prof. I. NAGANO of Kanazawa University for his guidance in the full wave calculation in Section 3.3.

The author wishes to express his sincere thanks to Prof. T. YOSHINO of University of Electro-Communication for his collaboration in the study of ELF wave observations by ISIS satellites in Chapter 3, periodic emission observation in Chapter 4, and balloon X-ray observation in Chapter 5. Sincere thanks are also due to his students, Messrs. T. KOJIMA, M. SUZUKI, M. ODAJIMA and M. HONMA, for their assistance in data analysis.

The author is deeply grateful to Prof. M. KODAMA of Yamanashi Medical College, Y. HIRASHIMA of Rikkyo University, and Dr. T. YAMAGAMI of Institute of Space and

Astronautical Science for their guidances in balloon X-ray experiments and valuable discussions on the X-ray data analyses.

The author is also grateful to Prof. S. ULLALAND of University of Bergen, Norway for his cooperation in balloon experiments in Norway and valuable comments on X-ray study in Chapter 5.

The author is deeply indebted to the staff of Upper Atmosphere Physics Branch, National Institute of Polar Research, for their efforts in carrying out upper atmosphere research at Syowa Station, Antarctica and its geomagnetically conjugate area in Iceland, and for their valuable discussions on the present work.

Thanks are also due to Communication Research Center in Canada and to Communication Research Laboratory, Ministry of Posts and Telecommunications in Japan for their cooperation in ISIS satellite data reception at Syowa Station.

The author expresses his sincere appreciation to the staff of Data Analysis Branch, National Institute of Polar Research for their kind help in the data analysis using HITAC M180 and M260 computer system. Finally the author thanks Mrs. M. IZAKI for her typing of this paper.

References

AGGSON, T. L. and KAPETANAKOS, C. A. (1966): On the impedance of a satellite borne VLF electric field antenna. NASA Tech. Rep., **X-612-66-380**, 42p.

AIKYO, K. and ONDOH, T. (1971): Propagation of nonducted VLF waves in the vicinity of the plasmapause. J. Radio Res. Lab., **18**, 153–182.

ALTMAN, C., CORY, H., ZOREA, S. and FIJALKOW, E. (1975): A full-wave study of downward propagating ELF waves in the ionosphere; Ion cutoff whistlers and the low frequency cutoff of ELF noise. Planet. Space Sci., **23**, 1155–1168.

ANGERAMI, J. J. (1970): Whistler duct properties deduced from VLF observations with the OGO 3 satellite near the magnetic equator. J. Geophys. Res., **75**, 6115–6135.

ANGERAMI, J. J. and CARPENTER, D. J. (1966): Whistler studies of the plasmapause in the magnetosphere electron density and total tube electron content near the Knees in magnetospheric ionization. J. Geophys. Res., **71**, 711–725.

ANGERAMI, J. J. and THOMAS, J.O. (1964): Studies of planetary atmospheres, 1. The distribution of electrons and ions in the earth's exosphere. J. Geophys. Res., **69**, 4537–4760.

ASHOUR-ABDALLA, M. and COWLEY, S. W. H. (1974): Wave-particle interactions near the geostationary orbit. Magnetospheric Physics, ed. by B. M. MCCORMAC. Dordrecht, D. Reidel, 241–279 (Astrophysics and Space Science Library, Vol. 44).

BASLER, R. P. (1963): Radio wave absorption in the auroral ionosphere. J. Geophys. Res., **68**, 4665–4681.

BARRINGTON, R. E., HARTZ, T. R. and HARVEY, R. W. (1971): Diurnal distribution of ELF, VLF, and LF noise at high latitudes as observed by Alouette 2. J. Geophys. Res., **76**, 5278–5291.

BERING, E. A., KELLEY, M. C. and MOZER, F. S. (1975): Observations of an intense field-aligned thermal ion flow and associated intense narrow band electric field oscillations. J. Geophys. Res., **80**, 4612–4620.

BERNHARDT, P. A. and PARK, C. G. (1977): Protonospheric-ionospheric modeling of VLF ducts. J. Geophys. Res., **82**, 5222–5230.

BINSACK, J. H. (1967): Plasmapause observations with the M.I.T. experiment on Imp 2. J. Geophys. Res., **72**, 5231–5237.

BRICE, N. (1965): Multiphase periodic very-low-frequency emissions. Radio Sci., **69D**, 257–265.

BURTIS, W. J. and HELLIWELL, R. A. (1969): Banded chorus—A new type of VLF radiation observed in the magnetosphere by OGO 1 and OGO 3. J. Geophys. Res., **74**, 3002–3010.

BURTIS, W. J. and HELLIWELL, R. A. (1976): Magnetospheric chorus; Occurrence patterns and normalized frequency. Planet. Space Sci., **24**, 1007–1024.

BURTON, R. K. and HOLZER, R. E. (1974): The origin and propagation of chorus in the outer magnetosphere. J. Geophys. Res., **76**, 1014–1023.

BURTON, R. K., RUSSELL, C. T. and CHAPPELL, C. R. (1970): The Alfven velocity in the magnetosphere and its relationship to ELF emissions. J. Geophys. Res., **75**, 5582–5586.

CARPENTER, D. L. (1963): Whistler evidence of a "knee" in the magnetospheric ionization density profile. J. Geophys. Res., **68**, 1675–1682.

CERISIER, J. C. (1974): Ducted and partly ducted propagation of VLF waves through the magnetosphere. J. Atmos. Terr. Phys., **36**, 1443–1467.

CHURCH, S. R. and THORNE, R. M. (1983): On the origin of plasmaspheric hiss; Ray path integrated amplification. J. Geophys. Res., **88**, 7941–7957.

CORNILLEAU-WEHRLIN, N., GENDRIN, R., LEFEUVRE, F., PARROT, A., GRARD, R., JONES, D., BAHNSEN, A., UNGSTRUP, E. and GIBBONS, W. (1978a): VLF electromagnetic waves observed onboard GEOS-1. Space Sci. Rev., **22**, 371–382.

CORNILLEAU-WEHRLIN, N., GENDRIN, R. and TIXIER, M. (1978b): VLF waves; Conjugated ground-satellite relationships. Space Sci. Rev., **22**, 419–431.

CORNILLEAU-WEHRLIN, N., SOLOMON, J., KORTH, A. and KREMSER, G. (1985): Experimental study of the relationship between energetic electrons and ELF waves observed on board GEOS; A support to quasi-linear theory. J. Geophys. Res., **90**, 4141–4154.

CORONITI, F. V. and KENNEL, C. F. (1970): Electron precipitation pulsations. J. Geophys. Res., **75**, 1279–1289.

DUNCKEL, N. and HELLIWELL, R. A. (1969): Whistler-mode emissions on the OGO 1 satellite. J. Geophys. Res., **74**, 6371–6385.

DÉCRÉAU, P. M., BEGHIN, C. and PARROT, M. (1982): Global characteristics of the cold plasma in the equatorial plasmapause region as deduced from the GEOS1 mutual impedance probe. J. Geophys. Res., **87**, 695–712.

EGELAND, A., GUSTAFSSON, G., OLSEN, S., ARONS, J. and BARRON, W. (1965): Auroral emissions centered at 700 cycles per second. J. Geophys. Res., **70**, 1079–1082.

ETCHETO, J., GENDRIN, R., SOLOMON, J. and ROUX, A. (1973): A self-consistent theory of magnetospheric ELF hiss. J. Geophys. Res., **78**, 8150–8166.

EVIATAR, A., LENCHEK, A. M. and SINGER, S. F. (1964): Distribution of density in an ion-exosphere of a nonrotating planet. Phys. Fluids, **7**, 1775–1779.

FOSTER, J. C. and ROSENBERG, T. J. (1976): Electron precipitation and VLF emissions associated with cyclotron resonance interaction near the plasmapause. J. Geophys. Res., **81**, 2183–2192.

GURNETT, D. A. (1966): A satellite study of VLF hiss. J. Geophys. Res., **71**, 5599–5615.

GURNETT, D. A. and BURNS, T. B. (1968): The low-frequency cutoff of ELF emissions. J. Geophys. Res., **73**, 7437–7445.

HARGREAVES, J. K. and COWLEY, F. C. (1967): Studies of auroral radio absorption events at three magnetic latitudes—II, Differences between conjugate regions. Planet. Space Sci., **15**, 1585–1597.

HASHIMOTO, K., KIMURA, I. and KUMAGAI, H. (1977): Estimation of electron temperature by VLF waves propagating in directions near the resonance cone. Planet. Space Sci., **25**, 871–877.

HELLIWELL, R. A. (1963): Whistler-triggered periodic VLF emission. J. Geophys. Res., **68**, 5387–5395.

HELLIWELL, R. A. (1965): Whistlers and Related Ionospheric Phenomena. Stanford, Stanford Univ. Press, 349p.

HOFFMAN, J. H. and DODSON, W. H. (1980): Light ion concentrations and fluxes in the polar regions during magnetically quiet times. J. Geophys. Res., **85**, 626–632.

HOFFMAN, J. H., DODSON, W. H., LIPPINCOTT, C. R. and HAMMAK, H. D. (1974): Initial ion composition results from the Isis 2 satellite. J. Geophys. Res., **79**, 4246–4251.

HOLZER, R. E., FARLEY, T. A. and BURTON, R. K. (1974): A correlated study of ELF waves and electron precipitation on Ogo 6. J. Geophys. Res., **79**, 1007–1013.

HUANG, C. Y. and GOERTZ, C. K. (1983): Ray-tracing studies and path-integrated gains of ELF unducted whistler mode waves in the earth's magnetosphere. J. Geophys. Res., **88**, 6181–6187.

HUANG, C. Y., GOERTZ, C. K. and ANDERSON, R. R. (1983): A theoretical study of plasmaspheric hiss generation. J. Geophys. Res., **88**, 7927–7940.

IMHOF, W. L., VOSS, H. D., WALT, M., GAINES, E. E., MODILIA, J., DATLOWE, D. W. and REAGON, J. B. (1986): Slot region electron precipitation by lightning, VLF chorus, and plasmaspheric hiss. J. Geophys. Res., **91**, 8883–8894.

INAN, U. S. and BELL, T. F. (1977): The plasmapause as a VLF wave guide. J. Geophys. Res., **82**, 2819–2827.

INAN, U. S., BELL, T. F. and CHANG, H. C. (1982): Particle precipitation induced by short-duration VLF waves in the magnetosphere. J. Geophys. Res., **87**, 6243–6264.

ISENBERG, P. A., KOONS, H. C. and FENNELL, J. F. (1982): Simultaneous observations of energetic electrons and dawnside chorus in geosynchronous orbit. J. Geophys. Res., **87**, 1495–1503.

ITO, K., SHIBUYA, S., MAEZAWA, K. and SATO, N. (1986): Statistical characteristics of 750-Hz band ELF emissions observed at Syowa Station. Mem. Natl Inst. Polar Res., Spec. Issue, **42**, 10–20.

JAMES, H. G. (1980): Direction-of-arrival measurements of auroral kilometric radiation and associated ELF data from Isis 1. J. Geophys. Res., **85**, 3367–3375.

JONES, D. (1969): The effect of the latitudinal variation of the terrestrial magnetic field strength on ion cyclotron whistlers. J. Atmos. Terr. Phys., **31**, 971–981.

KAMADA, T., NISHINO, M., TANAKA, Y., HIRASAWA, T. and OYA, H. (1981): Observation of auroral hiss by S-310JA-6 sounding rocket. Mem. Natl Inst. Polar Res., Spec. Issue, **18**, 453–461.

KELLEY, M. C., TSURUTANI, B. T. and MOZER, F. S. (1975): Properties of ELF electromagnetic waves in and above the earth's ionosphere deduced from plasma wave experiments on the OV1-17 and Ogo 6 satellites. J. Geophys. Res., **81**, 4603–4611.

KENNEL, C. F. and PETSCHECK, H. E. (1966): Limit on stably trapped particle fluxes. J. Geophys. Res., **71**, 1–28.

KIMURA, I. (1966): Effects of ions on whistler mode ray tracing. Radio Sci., **1**, 269–283.

KIMURA, I. (1985): Whistler mode propagation in the earth and planetary magnetospheres and ray tracing techniques. Space Sci. Rev., **42**, 449–466.

KIMURA, I. and MATSUO, T. (1982): Wave normal direction of auroral hiss observed by the S-310JA-5 rocket. Mem. Natl Inst. Polar Res., Spec. Issue, **22**, 185–195.

KIMURA, I., YAMAGISHI, H., MATSUO, T. and KAMADA, T. (1978): S-310JA-1 rocket observation of VLF emission spectra at Syowa Station in Antarctica. Mem. Natl Inst. Polar Res., Spec. Issue, **9**, 51–68.

KIMURA, I., MATSUO, T., TSUDA, M. and YAMAUCHI, K. (1985): Three dimensional ray tracing of whistler mode waves in a non-dipolar magnetosphere. J. Geomagn. Geoelectr., **37**, 945–956.

KOKUBUN, S., HAYASHI, K. and OGUTI, T. (1969): VLF emission study at Syowa Station, Antarctica—Polar chorus emission and worldwide geomagnetic variation—. JARE Sci. Rep., Ser. A (Aeronomy), **6**, 34p.

KREMSER, G., KORTH, A., ULLALAND, S., STADSNES, J., BAUMJOHANN, W., *et al.* (1986): Energetic electron precipitation during a magnetospheric substorm and its relationship to wave particle interaction. J. Geophys. Res., **91**, 5711–5718.

KURTH, W. S., BAUMBACK, M. M. and GURNETT, D. A. (1975): Direction-finding measurements of auroral kilometric radiation. J. Geophys. Res., **80**, 2764–2770.

LOKKEN, J. E., SHAND, J. A., SIR WRIGHT, C. S., K.C.B., O.B.E., MARTIN, L.H., BRICE, N.M. and HELLIWELL, R. A. (1961): Stanford-Pacific Naval Laboratory conjugate point experiment. Nature, **192**, 319–321.

MATSUDO, T. and SATO, N. (1986): Short-period magnetic pulsation induced by periodic VLF emission. Mem. Natl Inst. Polar Res., Spec. Issue, **42**, 1–9.

MATUURA, N. (1979): Kyokuiki denrisô no kôzô (A review on structure of the polar ionosphere). Nankyoku Shiryô (Antarct. Rec.), **65**, 1–14.

NAGANO, I., MAMBO, M., YAMAKAWA, H. and KIMURA, I. (1980): Kyokkô-tai ni okeru VLF ha no full wave keisan (A full wave calculation of VLF waves in auroral zone). Nankyoku Shiryô (Antarct. Rec.), **68**, 203–214.

NAGANO, I., MAMBO, M., SHIMBO, T. and KIMURA, I. (1986): Intensity and polarization characteristics along the earth's surface for the ELF-VLF waves emitted from a transmission cone in the high latitude. Mem. Natl Inst. Polar Res., Spec. Issue, **42**, 34–44.

NAGANO, I., MAMBO, M., SHIMBO, T. and KIMURA, I. (1987): Propagation characteristics in the earth-ionosphere waveguide for VLF waves emitted from trapping cones at high latitudes. Mem. Natl Inst. Polar Res., Spec. Issue, **47**, 183–191.

NISHINO, M. and TANAKA, Y. (1987): Observations of auroral LHR noise by the sounding rocket S-310JA-6. Planet. Space Sci., **35**, 127–137.

OGAWA, T., MORI, H., MIYAZAKI, S. and YAMAGISHI, H. (1981): Electrostatic plasma instabilities in highly active aurora observed by a sounding rocket S-310JA-7. Mem. Natl Inst. Polar Res., Spec. Issue, **18**, 312–329.

OLIVEN, M. N. and GURNETT, D. A. (1968): Microburst phenomena, 3, An association between microbursts and VLF chorus. J. Geophys. Res., **73**, 2355–2362.

ONDOH, T., AIKYO, K. and NAGAYAMA, M. (1972): VLF and ELF noise in the plasmasphere. J. Radio Res. Lab., **19**, 23–51.

PARK, C. G., LIN, C. S. and PARKS, G. K. (1981): A ground-satellite study of wave-particle correlations. J. Geophys. Res., **86**, 37–53.

PARKS, G. K. (1967): Spatial characteristics of auroral-zone X-ray microbursts. J. Geophys. Res., **72**, 215–225.

RADIO RESEARCH LABORATORIES (1981): World wide maps of electron density and temperature, mean ion mass, ion temperature and ion composition obtained from ionosphere sounding satellite-b observations August 1978 to April 1980. Tokyo, 95p.

ROEDERER, J. G. (1970): Dynamics of Geomagnetically Trapped Radiation. Berlin, Springer, 166p. (Physics and Chemistry in Space, Vol. 2).

ROSENBERG, T. J. and DUDENEY, J. R. (1986): The local time, substorm, and seasonal dependence of electron precipitation at $L=4$ inferred from riometer measurements. J. Geophys. Res., **91**, 12032–12040.

ROSENBERG, T. J., HELLIWELL, R. A. and KATSUFRAKIS, J. P. (1971): Electron precipitation associated with discrete very-low-frequency emissions. J. Geophys. Res., **76**, 8445–8452.

ROSENBERG, T. J., SIREN, J. C., MATTHEW, D. L., MARTHINSEN, K., HOLTET, J. A., EGELAND, A., CARPENTER, D. L. and HELLIWELL, R. A. (1981): Conjugacy of electron microburst and VLF chorus. J. Geophys. Res., **86**, 5819–5832.

RUSSELL, C. T. and HOLZER, R. E. (1970): AC magnetic field. Particles and Fields in the Magnetosphere, ed by B. M. MCCORMAC. Dordrecht, D. Reidel, 453 p. (Astrophysics and Space Science Library, Vol. 17).

RUSSELL, C. T., HOLZER, R. E. and SMITH, E. J. (1969): OGO 3 observation of ELF noise in the magnetosphere 1. Spatial extent and frequency of occurrence. J. Geophys. Res., **74**, 755–777.

RUSSELL, C. T., MCPHERRON, R. L. and COLEMAN, P. J., JR. (1972): Fluctuating magnetic field in the magnetosphere 1; ELF and VLF fluctuations. Space Sci. Rev., **12**, 810–856.

SAITO, H., YOSHINO, T. and SATO, N. (1986): Statistical characteristics of narrow-banded ELF emissions observed on board ISIS satellite. Mem. Natl Inst. Polar Res., Spec. Issue, **42**, 29–33.

SAITO, H., YOSHINO, T. and SATO, N. (1987): Narrow-banded ELF emissions over the southern polar region. Planet. Space Sci., **35**, 745–752.

SATO, N. (1984): Short-period magnetic pulsations associated with periodic VLF emissions ($T\sim5.6$ s). J. Geophys. Res., **89**, 2781–2787.

SATO, N. and FUKUNISHI, H. (1981): Interaction between ELF-VLF emissions and magnetic pulsations; Classification of quasi-periodic ELF-VLF emissions based on frequency-time spectra. J. Geophys. Res., **86**, 19–29.

SATO, N. and HAYASHI, K. (1985): Band-limited ELF emission burst (aurora roar). J. Geophys. Res., **90**, 3531–3535.

SATO, N. and KOKUBUN, S. (1980): Interaction between ELF-VLF emissions and magnetic pulsations; Quasi-periodic ELF-VLF emissions associated with Pc 3-4 magnetic pulsations and their geomagnetic conjugacy. J. Geophys. Res., **85**, 101–113.

SCARABUCCI, R. R. (1969): Interpretation of VLF signals observed on the OGO-4 satellite. Tech. Rep., Radiosci. Lab., Stanford Univ., **3418-2**.

SMITH, R. L. (1961): Propagation characteristics of whistlers trapped in field-aligned columns of enhanced ionization. J. Geophys. Res., **66**, 3699–3707.

SMITH, R. L. and ANGERAMI, J. J. (1968): Magnetospheric properties deduced from OGO 1 observations of ducted and nonducted whistlers. J. Geophys. Res., **73**, 10–20.

SMITH, E. J., FRANDSEN, A. M. A., TSURUTANI, B. T., THORNE, R. M. and CHAN, K. W. (1974): Plasmaspheric hiss intensity variation during magnetic storms. J. Geophys. Res., **79**, 2507–2510.

SONWALKAR, V. S. and INAN, U. S. (1986): Measurements of Siple transmitter signals on the DE 1 satellite; Wave normal direction and antenna effective length. J. Geophys. Res., **91**, 154–164.

STUART, G. F. (1977): Plasmaspheric whistler duct positions. J. Atmos. Terr. Phys., **39**, 433–444.

SUZUKI, H. and SATO, N. (1987): Seasonal and diurnal variations of ELF emission occurrences at 750-Hz band observed at geomagnetically conjugate stations. J. Geophys. Res., **92**, 6153–6158.

TAYLOR, W. W. L. and GURNETT, D. A. (1968): Morphology of VLF emissions observed with the Injun 3 satellite. J. Geophys. Res., **73**, 5615–5626.

TEMERIN, M. and LYSAK, R. L. (1984): Electromagnetic ion cycloton mode (ELF) waves generated by auroral electron precipitation. J. Geophys. Res., **89**, 2849–2859.

THOMSON, R. J. and DOWDEN, R. L. (1977): Simultaneous ground and satellite reception of whistlers 1. Ducted whistlers. J. Atmos. Terr. Phys., **39**, 869–877.

THORNE, R. M. and KENNEL, C. F. (1967): Quasi-srapped VLF propagation in the outer magnetosphere. J. Geophys. Res., **72**, 857–870.

THORNE, R. M., SMITH, E. J., BURTON, R. K. and HOLZER, R. E. (1973): Plasmaspheric hiss. J. Geophys. Res., **78**, 1581–1596.

THORNE, R. M., SMITH, E. J., FISKE, K. J. and CHURCH, S. R. (1974): Intensity variation of ELF hiss and during isolated substorms. Geophys. Res. Lett., **1**, 193–196.

THORNE, R. M., CHURCH, S. R., MALLOY, W. J. and TSURUTANI, B. T. (1977): The local time variation of ELF emissions during periods of substorm activity. J. Geophys. Res., **82**, 1585–1590.

THORNE, R. M., CHURCH, S. R. and GORNEY, D. J. (1979): On the origin of plasmaspheric hiss; The importance of wave propagation and the plasmapause. J. Geophys. Res., **84**, 5241–5247.

TIXIER, M. and CHARCOSSET, G. (1978): Partly ducted whistlers over Europe. J. Atmos. Terr. Phys., **40**, 601–613.

TSURUDA, K., MACHIDA, S., TERASAWA, T., NISHIDA, A. and MAEZAWA, K. (1982): High spatial attenuation of the Siple transmitter signal and natural VLF chorus observed at ground-based chain stations near Roberval, Quebec. J. Geophys. Res., **87**, 742–750.

TSURUTANI, B. T. and SMITH, E. J. (1977): Two types of magnetospheric ELF chorus and their substorm dependences. J. Geophys. Res., **82**, 5112–5128.

UNGSTRUP, E. and JACKEROTT, I. M. (1963): Observations of chorus below 1500 cycles per second at Godhaven, Greenland, from July 1957 to December 1961. J. Geophys. Res., **68**, 2141–2146.

WALTER, F. (1969): Nonducted VLF propagation in the magnetosphere. Radioscience Lab., Stanford Electronics Labs., Stanford University, SEL-69-061.

WEST, R. H. and PARKS, G. K. (1984): ELF emission and relativistic electron precipitation. J. Geophys. Res., **89**, 159–167.

XIAO-TING, S. and CAUDAL, G. (1987): Electron density near the plasmapause measured over one year by GEOS-2; A statistical analysis. J. Atmos. Terr. Phys., **49**, 135–144.

YABROFF, I. (1961): Computation of whistler ray paths. J. Res. Natl. Bur. Stand., Sect D, **65**, 485.

YAMAGISHI, H., FUKUNISHI, H., HIRASAWA, T. and OGAWA, T. (1981): Measurements of auroral electric fields with an Antarctic sounding rocket S-310JA-7. 2. AC electric field. Mem. Natl Inst. Polar Res., Spec. Issue, **18**, 379–390.

YAMAGISHI, H., ONO, T., FUKUNISHI, H., YAMAGAMI, T., NISHIMURA, J. *et al.* (1984): Auroral zone X-ray pulsations associated with VLF pulsations; B_{15}-3 balloon experiment. Mem. Natl Inst. Polar Res., Spec. Issue, **31**, 124–136.

YAMAGISHI, H., ONO, T., FUKUNISHI, H., YAMAGAMI, T., NISHIMURA, J. *et al.* (1985): Pulsating phenomena of auroral-zone X-rays associated with quasi-periodic VLF emissions and Pc 3 magnetic pulsations. J. Geomagn. Geoelectr., **37**, 927–943.

YOSHINO, T., Ozaki, T. and FUKUNISHI, H. (1981): Occurrence distribution of VLF hiss and saucer emissions over the southern polar region. J. Geophys. Res., **86**, 846–852.

(Received November 30, 1988; Revised manuscript received January 25, 1989)

Appendix 1

The polarization of the whistler mode wave electric field in the plane perpendicular to $\boldsymbol{k}$ is given by

$$\rho_1 \equiv E_\perp / E_y = j 2Y_L / \{Y_T^2/(1-X) + \sqrt{Y_T^4/(1-X)^2 + 4Y_L^2}\} , \tag{A-1}$$

where E_y and $E_\perp$ denote respectively the electric field components in y direction and in the direction perpendicular to $\boldsymbol{k}$ and y-axis. Y_L and Y_T are difined as $Y_L = Y\cos\psi$ and $Y_T = Y\sin\psi$, where $Y \equiv f_H/f$ and $X \equiv (f_p/f)^2$, and f_H and f_p denote respectively electron gyrofrequency and electron plasma frequency, and j a unit of imaginary number. The polarization of the wave electric field in the plane, which includes $\boldsymbol{k}$, is given by

$$\rho_2 \equiv E_k / E_y = j \cdot Y_T(1-n^2)/(1-X) , \tag{A-2}$$

where E_k denotes the electric field component parallel to $\boldsymbol{k}$, and n the refractive index of the whistler mode wave given by

$$n^2 = 1 - 2X/\{2 - Y_T^2/(1-X) - \sqrt{Y_T^4/(1-X)^2 + 4Y_L^2}\} . \tag{A-3}$$

Then, the polarization of the whistler mode wave electric field, ρ, is defined as

$$\rho = \sqrt{|\rho_1|^2 + |\rho_2|^2} . \tag{A-4}$$

In ELF range, the condition for the quasi longitudinal approximation

$$4Y_L^2 \gg Y_T^4/(1-X)^2 , \tag{A-5}$$

is satisfied. By applying the inequality of eq. (A-5) and another inequality of $X \gg 1$, which is well satisfied in ELF range, eqs. (A-1), (A-2) and (A-4) become

$$\rho_1 = j \cdot 2Y_L/(Y_T^2/X + 2Y_L) , \tag{A-6}$$

$$\rho_2 = j \cdot 2Y_T/(Y_T^2/X + 2Y_L) , \tag{A-7}$$

$$\rho = 2Y/(Y_T^2/X + 2Y_L) . \tag{A-8}$$

In the dayside polar ionosphere at an altitude of 1450 km, where ISIS-2 was passing, typical values of f_p and f_H are 740 kHz and 640 kHz, respectively. The wave frequency of ELF hiss, f, is typically 1 kHz. For these values, X and Y become respectively 5.5×10^5 and 640, and an inequality of $(Y_T^2/X)/2Y_L < 1/10$ is satisfied when $|\psi| < 89.7°$. In this condition, the first term in the denominator of eq. (A-8) can be neglected in comparison with the second term, and eq. (A-8) becomes

$$\rho = Y/Y_L = 1/\cos\psi . \tag{A-9}$$

The angle α between $\boldsymbol{B}_0$ and the polarization plane of $\boldsymbol{E}$ is given by

$$\begin{aligned} \alpha &= \psi + \tan^{-1}(|\boldsymbol{E}|/|\boldsymbol{E}_k|) \\ &= \psi + \tan^{-1}(|\rho_1|/|\rho_2|) . \end{aligned} \tag{A-10}$$

By substituting ρ_1 and ρ_2 of eqs. (A-6) and (A-7) into eq. (A-10),

$$\begin{aligned} \alpha &= \psi + \tan^{-1}(Y_L/Y_T) \\ &= \psi + \tan^{-1}(1/\tan\psi) = 90° . \end{aligned} \tag{A-11}$$

This means that the whistler mode wave electric field is polarized in the plane perpendicular to $\boldsymbol{B}_0$.

Appendix 2

In order to obtain the dependency of R-to-R mode coupling rate on H^+ to O^+ concentration ratio, a full wave calculation is made for three ion composition models F, G and H, shown in Table A-1. These ion compositions are given at an altitude of 1450 km, and the compositions at other altitudes are given by diffusive equilibrium condition. The altitude range for the calculation is 1450–1640 km, because we consider mode coupling arising just above the ISIS-2 satellite altitude of 1450 km, and the wave frequency is chosen as 400, 210 and 140 Hz for the each model so that cross-over and $L=0$ cutoff appear in above altitude range. The results of the calculation is shown in Fig. A-1. It is found that the attenuation at the $L=0$ cutoff is mainly dependent on ψ, and not much dependent on the ion composition, nor wave frequency.

Table A-1. Ion composition models for the full wave calculation shown in Fig. A-1.

Altitude : 1450 km

Model	Fractional abundance			Composition			Wave frequency
	H^+	He^+	O^+	H^+	He^+	O^+	
F	10^3 cm^{-3}	20 cm^{-3}	9×10^3 cm^{-3}	9.9%	0.2%	89.8%	400 Hz
G	5×10^3	20	5×10^3	49.9	0.2	49.9	210
H	7×10^3	20	3×10^3	69.9	0.2	29.9	140

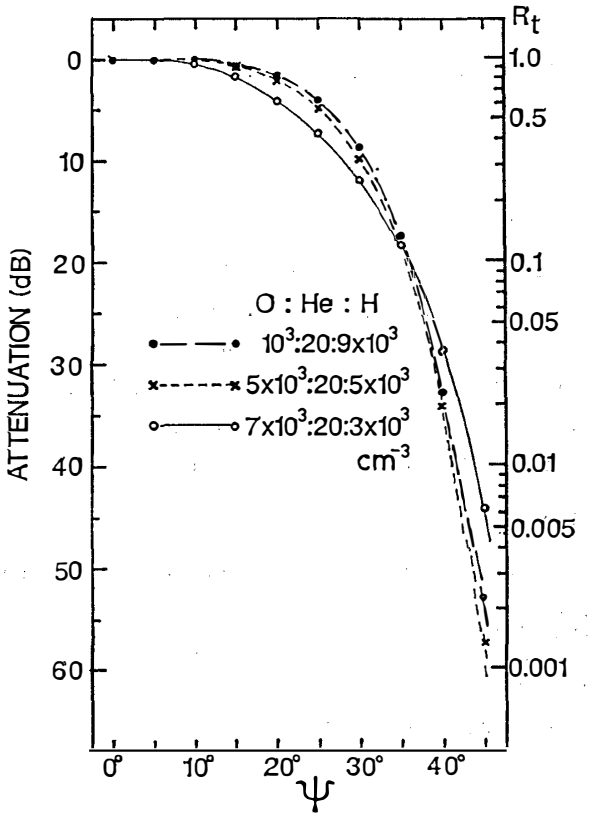

Fig. A-1. A plot of the attenuation at $L=0$ cutoff (, or the penetration rate, R_t) vs. ψ for three models of ion composition shown in Table A-1. The direction of B_0 is assumed to be vertical.

Appendix 3

The sheath impedance of a cylindrical antenna immersed in plasma consists of capacitive component $1/\omega c_s$ and resistive component r_s. In ELF range, r_s is much smaller than $1/\omega c_s$ for the magnetospheric plasma (AGGSON and KAPETANAKOS, 1966), and the impedance can be regarded as resistive. According to their calculation, r_s for a cylindrical antenna of 10 mm in diameter and 1 m in length is approximated by

$$r_s = 5.4 \times 10^4 N_e^{-0.61} \quad (\mathrm{k}\Omega) , \tag{A-12}$$

for the electron density range of 10^3–10^4 cm^{-3} in the lower magnetosphere. As the diameter and the length of the ISIS VLF antenna was 13 mm and 36 m (one side), the sheath resistance of this antenna is given by

$$R_s = 1.15 \times 10^3 N_e^{-0.61} \quad (\mathrm{k}\Omega) . \tag{A-13}$$

For the typical electron density of 10^4 cm^{-3} at the altitude of ISIS-2 satellite, R_s becomes 4.2 kΩ. Considering the input resistance of the receiver of 16 kΩ and the effective length of the antenna of 36 m, the wave electric field is given by

$$E(\mathrm{V/m}) = \frac{1}{36} \cdot \frac{R_s + 16}{16} V_{in} , \tag{A-14}$$

where V_{in} stands for the input voltage of the receiver. V_i is obtained from the amplitude of the AGC signal with the following relation

$$V_i = \exp(R_5 A^4 + R_4 A^3 + R_3 A^2 + R_2 A + R_1) , \tag{A-15}$$

where A is the decimal expression of the AGC signal and

$$\left.\begin{aligned} R_5 &= -1.2 \\ R_4 &= 3.4 \times 10^{-2} \\ R_3 &= 7.38 \times 10^{-5} \\ R_2 &= -1.66 \times 10^{-6} \\ R_1 &= 6.03 \times 10^{-9} \end{aligned}\right\} . \tag{A-16}$$

Appendix 4

Here, the divergence of the ray paths in the off-meridian plane is estimated for low altitude range ($\leq$9000 km) with large ($\sim$70°) dip angle.

As discussed in Section 2.5, the wave normal direction along a ray path in low altitudes depends mainly on the vertical electron density gradient. Hence, we neglect other effects such as the curvature of the geomagnetic field line and horizontal electron density gradient, and obtain altitude dependence of wave normal direction in off-meridian plane based on Snell's law. Here, the ionosphere is assumed to be horizontally stratified layers, and the dip angle of the geomagnetic field constant.

In the following analysis, coordinate system shown in Fig. A-2 is used, where x, y and z-axis represents the geomagnetic east, the geomagnetic north and upward direction, respectively. Angle δ denotes the dip angle of the geomagnetic field $\boldsymbol{B}_0$, and ϕ is azimuthal angle of wave normal vector $\boldsymbol{k}$, measured clockwise from the geomagnetic north.

The vector $\boldsymbol{k}$ is expressed as follows

$$\begin{aligned}\boldsymbol{k} &= \boldsymbol{k}_{//} + \boldsymbol{k}_{\perp} \\ &= k\cdot\cos\psi\,(0,\ \cos\delta,\ -\sin\delta) + k\cdot\sin\psi\,(\sin\phi,\ \cos\phi\,\sin\delta,\ -\cos\phi\,\cos\delta) \\ &= k(\sin\psi\,\sin\phi,\ \cos\psi\,\cos\delta + \sin\psi\,\cos\phi\,\sin\delta,\ -\cos\psi\,\sin\delta - \sin\psi\,\cos\phi\,\cos\delta)\ ,\end{aligned}$$

where ψ denotes the wave normal angle with respect to $\boldsymbol{B}_0$.

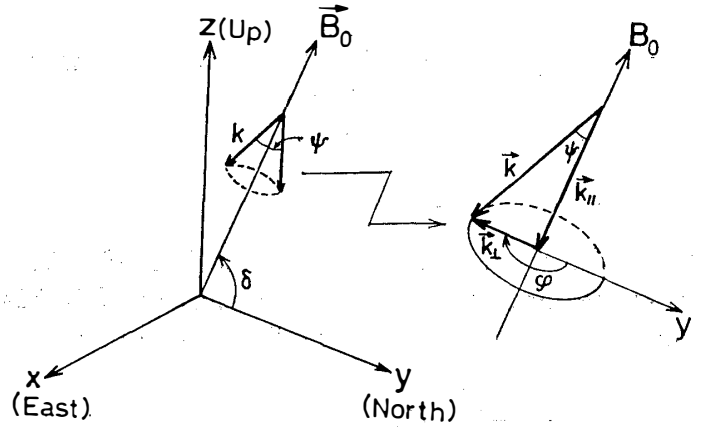

Fig. A-2. Coordinate system used in this analysis.

The wave incident angle θ is given by the scalar product of $\boldsymbol{k}$ and $\boldsymbol{z}\equiv(0,\ 0,\ 1)$ as

$$\begin{aligned}\cos\theta &= -\boldsymbol{k}\cdot\boldsymbol{z}/k \\ &= \cos\psi\,\sin\delta + \sin\psi\,\cos\phi\,\cos\delta\ .\end{aligned} \tag{A-17}$$

When δ approaches 90°, the second term of eq. (A-17), dependent on ϕ, becomes much smaller than the first term. This is one reason why the features of ray paths in off-meridian plane becomes similar to those in the meridian plane when δ approaches to 90°. There is a maximum value of ψ at the duct exit, which satisfies the following relation

$$\psi_{\mathrm{d}} = \cos^{-1}(N_{\mathrm{m}}/N_{\mathrm{b}})\ , \tag{A-18}$$

where N_{m} denotes the maximum value of the enhanced electron density in the duct, and N_{b} the background electron density.

In order to estimate the maximum deviation of a ray path from the field line at the duct, ψ, ϕ and θ at a certain altitude h will be calculated for initial wave normal direction of ψ_{d} and ϕ_{d} at the duct exit. The incident angle at the duct exit, θ_{d}, is given from eq. (A-17) as

$$\cos\theta_{\mathrm{d}} = \cos\psi_{\mathrm{d}}\,\sin\delta + \sin\psi_{\mathrm{d}}\,\cos\phi_{\mathrm{d}}\,\cos\delta\ . \tag{A-19}$$

According to Snell's law,

$$n_{\mathrm{d}}\,\sin\theta_{\mathrm{d}} = n\,\sin\theta\ , \tag{A-20}$$

where n_{d} and n denote refractive index of the whistler mode wave at the duct exit and at the altitude of h.

Eqs. (A-17), (A-19) and (A-20) give

$$1-(\cos\psi\,\sin\delta+\sin\psi\,\cos\phi\,\cos\delta)^2 = (n_d/n)^2\{1-(\cos\psi_d\,\sin\delta+\sin\psi_d\,\cos\phi_d\,\cos\delta)^2\}\ . \tag{A-21}$$

We compare three representative extreme cases; $\phi_d=0°$ and 180° of maximum and minimum incident angles at the duct exit, and $\phi_d=90°$ for off-meridian propagation. For $\phi_d=0°$, ϕ is kept at 0° during the downward propagation and eq. (A-21) becomes

$$1-\sin^2(\delta+\phi)=(n_d/n)^2\{1-\sin^2(\delta+\psi_d)\}\ . \tag{A-22}$$

For $\phi_d=180°$, ϕ is kept at 180° during the downward propagation and eq. (A-21) becomes

$$1-\sin^2(\delta-\phi)=(n_d/n)^2\{1-\sin^2(\delta-\psi_d)\}\ . \tag{A-23}$$

For $\phi_d=90°$, eq. (A-21) becomes

$$1-(\cos\psi\,\sin\delta+\sin\psi\,\cos\phi\,\cos\delta)^2-\frac{n_d^2}{n^2}(1-\cos^2\psi_d\,\sin^2\delta)\ . \tag{A-24}$$

Since

$$\cos\psi\,\sin\delta+\sin\psi\,\cos\phi\,\cos\delta=\sqrt{1+(n_d/n)^2(\cos^2\psi_d\,\sin^2\delta-1)}\ ,$$

it turns out that

$$\sin(\psi+\alpha)=\sqrt{1+(n_d/n)^2(\cos^2\psi_d\,\sin^2\delta-1)}\,/\,\sqrt{\sin^2\delta+\cos^2\phi\,\cos^2\delta}\ ,$$
$$\alpha=\tan^{-1}(\tan\delta/\cos\phi)\ . \tag{A-29}$$

We use typical value of $\psi_d=30°$ and $\delta=70°$, and calculate ϕ, ψ and θ for various n_d/n with eqs. (A-19), (A-20), (A-22), (A-23) and (A-25). Dependences of ϕ, θ, ψ and $|\psi|$ on n_d/n are shown in Figs. A-3a and 3b for $\phi_d=0°$, 90° and 180°. As n_d/n de-

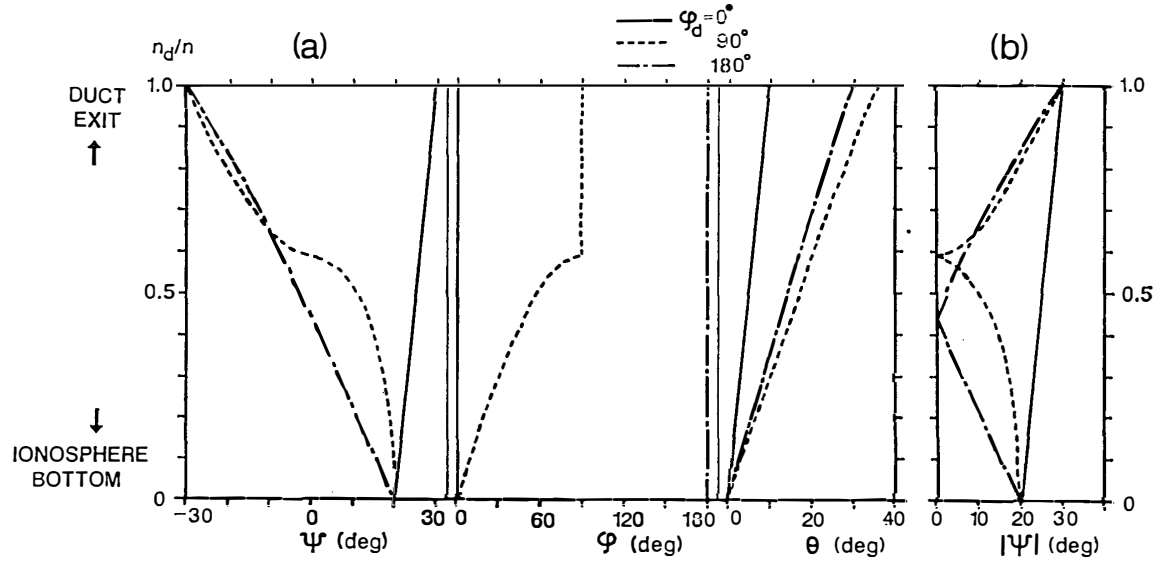

Fig. A-3. Variations of ψ, φ and θ (panel a), and $|\psi|$ (panel b) with n_d/n.

creases monotonically with altitude, these plots represent altitude variations of the above angles. In the case of $\phi_d=90°$, not only ψ, but also ϕ changes with n_d/n in order to satisfy Snell's law. It is found that $|\psi|$ for $\phi_d=90°$ is between those for $\phi_d=0°$ and $\phi_d=180°$ for most of n_d/n values. In this altitude range ($h\leq 9000$ km), $|\psi|$ is always smaller than the inflection angle of $\psi_{IA}=60°$ given from eq. (8). Under this condition, there is a positive correlation between $|\psi|$ and the ray direction, or the deviation of a ray path from the field line. Hence the above feature of $|\psi|$ for $\phi_d=0°$, 90° and 180° suggests that the deviation of the ray path from the field line for each ϕ_d value is in order of $\phi_d=0°$, 90° and 180°. It is shown in Figs. 66, 68, 71 and 73 that the deviation of the ray paths for $\phi_d=0°$ and 180° are almost the same. Therefore, the deviation of the ray path for $\phi_d=90°$ is also the same as those for $\phi_d=0°$ and 180°. That is, the divergence of ray paths in the off-meridian plane is nearly the same as that in the meridian plane, when the altitude is low (≤ 9000 km) and δ is large ($\sim 70°$).